UNIVERSITY OF CALIFORNIA

Santa Barbara

Tuning Biotic/Abiotic Interfaces for Enhanced Bioelectrochemical Conversion: Redox-Active Conjugated Oligo- and Polyelectrolytes

A dissertation submitted in partial satisfaction

of the requirements for the degree

Doctor of Philosophy

in

Chemical Engineering

by

Samantha McCuskey

Committee in charge:

Professor Guillermo C. Bazan, Co-Chair

Professor Rachel A. Segalman, Co-Chair

Professor Bradley F. Chmelka

Professor Matthew E. Helgeson

Professor Thuc-Quyen Nguyen

June 2020

The dissertation of Samantha McCuskey is approved.

_____

Professor Bradley F. Chmelka

_____

Professor Matthew E. Helgeson

_____

Professor Thuc-Quyen Nguyen

_____

Professor Rachel A. Segalman, Co-chair

_____

Professor Guillermo C. Bazan, Co-Chair

June 2020

Tuning Biotic/Abiotic Interfaces for Enhanced Bioelectrochemical Conversion:

Redox-Active Conjugated Oligo- and Polyelectrolytes

by

Samantha McCuskey

Acknowledgements

I am indebted to my primary advisor, Gui Bazan. You first inspired me to work in your group when we talked on a visit weekend about bacteria that can produce electricity and organic semiconductors that could help this process. You have inspired me to think critically about complex, interesting systems involving charge transport and how to keep the big picture in mind.

For my committee members, Rachel Segalman, Brad Chmelka, Matt Helgeson, and Quyen Nguyen, I appreciate your helpful insights during my annual committee meetings. I am especially grateful to Rachel for advising me during the first two years of my PhD and always pushing me to present my results and hypothesis in a full and concise manner. I want to thank members of the Bazan Group, Segalman Group, and CPOS for providing a welcoming environment to discuss science. For teaching me more about electrochemistry and always having enthusiasm to discuss fundamentals, I thank Lior Sepunaru. In particular, I am thankful to Scott Danielsen and Martin Seifrid, who were mentors to me in understanding scattering, polymer design and physics, as well as communicating research.

For helping me to get started on the Bioteam, I thank Nate Kirchhofer, Chelsea Catania, and Hengjing Yan. Nate, I still remember when you showed me how to assemble my first microbial electrochemical cell, while Chelsea and Hengjing, you would be proud of my biosafety and microbiological techniques. For patiently discussing with me about the interactions of our conjugated electrolytes with cells, I really appreciate Alex Moreland and Bing Wang. For the synthesis of the materials I used in my studies, I must thank Cheng-Kang Mai, Zach Rengert, and Dirk Leifert.

For fabricating the electrochemical cells and environmental chambers I used during my PhD, I must acknowledge Bruce Dunsen and Roger Green of the Chemistry Machine Shop. Thank you for pushing me to communicate my designs in coherent drawings and always offering up help when I needed it.

Being a part of the Bioelectronics team, Lijiao Ren, Yude Su, and Luana Llanes were my closest colleagues. I am grateful to Lijiao, you provided an example of efficient use of lab time and always lent a hand to trouble shoot my experiments. Yude, you were a critical part of my last project in designing and fabricating the working electrodes. From my time with you, I have learned invaluable lessons in close collaboration that I will take with me through my career. Luana, I can say you are one of my best friends and favorite lab mate during my time in Santa Barbara. Your kindness and strength as well as your enthusiasm for research and good energy in lab empower me to keep pursuing science as a woman.

To my parents, you gave me the tools for success in graduate school, namely self-discipline *and* creativity. I hope someday soon you can see me walk across the graduation stage.

To my husband, Taylor, I am so glad you are on this adventure with me. Even though this is not your field, you were the first to read my manuscripts and hear me practice my talks. I appreciate all of the support you give me in pursuit of my dreams. I must also thank our cats Oscar and Greta for staying up late with me during the writing of this dissertation.

Curriculum Vitæ

Samantha McCuskey

Education

2020	Ph. D. in Chemical Engineering, *University of California, Santa Barbara*
2015	B. S. in Chemical Engineering, Minor in Nanoscience/Nanotechnology, *summa cum laude,* *Florida Institute of Technology*

Research Experience

2015-2020	Graduate Student Researcher, *University of California, Santa Barbara*
2014	Research Assistant, *University of Massachusetts, Amherst*
2013	Materials Science R&D Co-op, *Mainstream Engineering Co.*

Teaching & Mentoring Experience

2019-2020	*University of California, Santa Barbara* Advanced Graduate Student Mentor, Graduate Scholars Program
2016-2019	*University of California, Santa Barbara* Junior & Senior Chemical Engineering Labs, Introduction to Chemical Engineering Design

Outreach

2020	UC Santa Barbara *ScienceLine*
2016-2020	*Family Ultimate Science Exploration (FUSE)*
2015-2020	*Graduate Students for Diversity in Science (GSDS)*
2016-2017	*NanoDays*

Awards & Honors

2020	2nd Place, *Electric Avenues*, Art of Science Competition, California NanoSystems Institute, UC Santa Barbara
2019	Outstanding Student Learner – Chinese, Confucius Institute, UC Santa Barbara
2017	National Science Foundation - Graduate Research Fellowship (NSF GRFP)

2016	Dow Materials Institute & Materials Research Laboratory Travel Fellowship
2016	Honorable Mention, National Science Foundation - Graduate Research Fellowship Program
2015	Best in Show – Chemical Engineering, Northrup Grumman Engineering & Science Student Design Showcase, Florida Tech
2015	Donald R. Mason Award in Chemical Engineering
2013-2014	Student Employee of the Year: Co-op, Florida Tech
2013-2014	Scholar-Athlete of the Year – Rowing, Florida Tech
2012-2013	Donald F. Othmer Academic Excellence Award, Central Florida AIChE
2011-2015	Bright Futures Scholarship, Florida State

Publications

12. McCuskey, S. R.; Llanes, L. C.; Su, Y.; Leifert, D.; Bazan, G. C. Self-doped Conjugated Polyelectrolytes in Microbial Fuel Cells. In preparation.

11. McCuskey, S. R.; Mostert, A. B.; Seifrid, M.; Danielsen, S. P. O.; Bazan, G. C. Hydration increases both electronic and ionic conduction in self-doped conjugated polyelectrolytes. In preparation.

10 Su, Y.; McCuskey, S. R.; Leifert, D.; Moreland, A. S.; Sepunaru, L.; Bazan, G. C. "Smart" Biological-Synthetic Composite that can Switch Operation between Current Generation and Electrochemical Energy Storage. In preparation.

9. Llanes, L. C.; McCuskey, S. R.; Hunt, C.; Menard, G.; Bazan, G. C. Porphyrin-based conjugated oligoelectrolytes: assembly and limitations for accelerating extracellular electron transfer. In preparation.

8. McCuskey, S. R.; Su, Y.; Leifert, D.; Moreland, A. S.; Bazan, G. C. "Living Bioelectrochemical Composites. *Advanced Materials* **1908178**, 1908178 (2020).

7. Ren, L.; McCuskey, S. R.; Moreland, A.; Bazan, G. C.; Nguyen, T.-Q. Tuning *Geobacter sulfurreducens* biofilm with conjugated polyelectrolyte for increased performance in bioelectrochemical system. *Biosensors and Bioelectronics* **144**, 111630 (2019). DOI: 10.1016/j.bios.2019.111630.

6. Tang, J.; Chen, Y.; McCuskey, S. R.; Chen, L.; Bazan, G. C.; Liang, Z. Recent Advances in n-Type Thermoelectric Nanocomposites. *Advanced Electronic Materials* **5**, 1800943 (2019). DOI: 10.1002/aelm.201800943.

5. McCuskey, S. R.;† Rengert Z. D.;† Zhang, M.; Helgeson, M. E.; Nguyen T.-Q.; Bazan G. C. Tuning the Potential of Electron Extraction from Microbes with Ferrocene-Containing Conjugated Oligoelectrolytes. *Advanced Biosystems* **3**, 1800303 (2018). DOI: 10.1002/adbi.201800303. †Co-first author.

4. Danielsen, S. P. O.; Sanoja, G. E.; McCuskey, S. R.; Hammouda, B.; Bazan, G.C.; Fredrickson, G.H.; Segalman, R. A. Mixed Conductive Soft Solids by Electrostatically Driven Network Formation of a Conjugated Polyelectrolyte. *Chemistry of Materials* **30**, 1417–1426 (2018). DOI: 10.1021/acs.chemmater.7b05303.

3. Burnett, E. K.; Ly, J.; Niazi, M. R.; Zhang, L.; McCuskey, S. R.; Amassian, A.; Smilgies, D.-M.; Mannsfeld, S. C. B.; Briseno, A. L. Bistetracene Thin Film Polymorphic Control to Unravel the Effect of Molecular Packing on Charge Transport. *Advanced Materials Interfaces* **5**, 1701607 (2018). DOI: 10.1002/admi.201701607.

2. Ren, T.; Erbakan, M.; Shen, Y.; Barbieri. E.; Saboe, P.; Feroz, H.; Yan, H.; McCuskey, S.; Hall, J. F.; Schantz, A. B.; Bazan, G. C.; Butler, P. J.; Grzelakowski, M.; Kumar, M. Membrane Protein Insertion into and Compatibility with Biomimetic Membranes. *Advanced Biosystems* **1**, 1700053 (2017). DOI: 10.1002/adbi.201700053.

1. Kirchhofer, N. D.;† McCuskey, S. R.;† Mai, C.-K.; Bazan, G. C. Anaerobic Respiration on Self-Doped Conjugated Polyelectrolytes : Impact of Chemical Structure. *Angewandte Chemie International Edition* **56**, 6519–6522 (2017). DOI: 10.1002/anie.201701964. †Co-first author.

Select Presentations

1. Kirchhofer, N.; Mai, C.-K.; McCuskey, S.;* Dahlquist, R.; Bazan, G. C. "Anaerobic Respiration on Self-Doped Conjugated Polyelectrolytes: Impact of Chemical Structure." Zing Organic Semiconductors Conference. Cavtat, Croatia. 9/24/2016. (Poster) *Presenter.

2. McCuskey, S. R. "Electron Conduction in Polymers: Molecular Orbital Approach" Polymer Physics Summer School. UC Santa Barbara. 9/5/2017. (Lecture)

3. McCuskey, S. R.; Rengert, Z.; Nguyen, T-Q.; Bazan, G. "Materials for Improving Electron Transfer from Microbial Communities." Asilomar Bioelectronics Symposium 2017. Pacific Grove, CA. 9/20/2017. (Poster and Oral) ***Poster Award**

4. McCuskey, S. R. "Conjugated Electrolytes for Improving Electron Transfer from Microbial Communities." Fudan University, Shanghai, China. 8/16/2017. (Seminar)

5. McCuskey, S. R.; Rengert, Z. D.; Zhang, M.; Helgeson, M.; Nguyen, T-Q.; Bazan, G. C. "Tuning the Potential of Electron Extraction from Microbes with Ferrocene-Containing Conjugated Oligoelectrolytes." DeLange XI Bioelectronics Conference. Rice University. 12/5/2018. (Poster) ***Travel Award**

6. McCuskey, S.R. "Tuning the Potential of Electron Extraction from Microbes with Ferrocene-Containing Conjugated Oligoelectrolytes." 2019 Chemical Science Student Seminar. UC Santa Barbara. 3/11/2019. (Seminar)

7. McCuskey, S. R. "How Could Bacteria Power the World?" 2019 UC Santa Barbara Grad Slam Competition. UC Santa Barbara. 4/17/2019. (Oral) ***Semi-Finalist**

8. McCuskey, S. R.; Bazan, G.C. " Bioelectronic Composites using Conjugated Polyelectrolytes: New Living Materials for Harnessing Bioelectrochemical Pathways." 2019 Chlorox-Amgen Chemical Engineering Graduate Student Symposium. UC Santa Barbara. 10/4/2019. (Seminar)
9. McCuskey, S. R. "Improving Electricity Generation from Microbial Communities." Lunch & Learn: Microbes & Measurement, Graduate Student Resource Center. UC Santa Barbara. 11/8/2019. (Lecture)
10. McCuskey, S. R.; Su, Y.; Leifert, D.; Moreland, A. S.; Bazan, G. C.; "Bioelectronic Composites using Self-Doped Conjugated Polyelectrolytes." 2019 Materials Research Society Fall Meeting. Boston, MA. 12/2/2019. (Oral)

Abstract

Tuning Biotic/Abiotic Interfaces for Enhanced Bioelectrochemical Conversion: Redox-Active Conjugated Oligo- and Polyelectrolytes

by

Samantha McCuskey

Bioelectronics concerns the integration of electronic elements with biological systems to form functional devices including biosensors for detection and analysis, neuroelectronic junctions, and biofuel cells for energy conversion and catalysis. A fundamental part of any bioelectronic system is the electronic coupling and transport at the various biotic/abiotic interfaces between biomaterials and electronic supports. The development and study of materials that modulate charge transport across these interfaces is therefore an area of interest. Advances in increasing the synergy between electronics and biology will see impacts in not only our understanding of system, cell, and molecular biology, but also more efficient electronics for conversion of bioenergy. In this development, we have focused on the implementation of redox-active conjugated electrolytes at the biotic/abiotic interface for amplifying biocurrent collection.

In specifically-designed microbial bioelectrochemical systems, bacteria interface with electrodes to catalyze the interconversion of chemical and electrical energy. Membrane modifiers called conjugated oligoelectrolytes (COEs), defined by their conjugated core and peripheral ionic pendant groups, have been shown to increase the ability of electrogenic microbes to electronically communicate with abiotic components through a number of

indirect factors including increasing electrode colonization and coulombic efficiency. However, precise control over the mechanism of current enhancement remained to be seen. Two ferrocene-containing COEs called DVFBO and F_4-DVFBO were designed to test voltammetric control over biocatalytic current production. Both COEs have a π-delocalized core capped on each end by ferrocene units and show similar optical properties, affinity for the membrane, and toxicity, but fluorination of the core (F_4-DVFBO) results in a higher redox potential (422 ± 5 mV compared to 365 ± 4 mV vs Ag/AgCl for DVFBO). The COEs were tested in anaerobic microbial three-electrode electrochemical cells (M3Cs) containing the model electrogenic bacterium *Shewanella oneidensis* MR-1. At a low electrode potential, the addition of the COEs produced negligible current enhancement compared to controls. However, at E = 365 mV, DVFBO increased steady-state biocurrent 67 ± 12% relative to controls while F_4-DVFBO only increased biocurrent by 30 ± 5%. With no change in electrode colonization, cyclic voltammetry supports that DVFBO is the primary conduit of the increased catalytic current and shows F_4-DVFBO has less activity at this poised potential. Overall, this work demonstrates the ability to modulate electron transfer from microbial species exclusively via the oxidation potential of the COE.

While microbial membrane modification with redox-active COEs led to improvement in current extraction, a two-dimensional electrode structure limits the surface area for electroactive bacteria attachment and restricts efficient substrate and buffer diffusion. Conjugated polyelectrolytes represent a complementary interfacial materials strategy to enhance biotic/abiotic electronic coupling. First, the mixed ionic-electronic conduction properties of the self-doped conjugated polyelectrolyte CPE-K were investigated with respect to hydration. Films of CPE-K showed both increasing ionic and electronic

conduction with hydration. Results indicate that the increase in electronic conduction was due to both increased number of free charge carriers and closer π-π stacking.

Following this characterization, CPE-K was used as a conductive matrix to electronically connect a three-dimensional network of *Shewanella oneidensis* MR-1 to a gold electrode. At critical CPE-K concentrations, these biocomposites spontaneously assemble from solution into an intricate arrangement of cells within a conductive polymer matrix, thereby increasing biocurrent ~150-fold over control biofilms in M3C tests. While increased biocurrent is due to more cells in communication with the electrode, current extracted per cell is also enhanced indicating efficient long-range electron transport. Further, biocomposites show almost an order-of-magnitude lower charge transfer resistance than CPE-K alone, supporting that the electroactive bacteria and the conjugated polyelectrolyte work synergistically towards an effective electronic biocomposite. Examination of these biocomposites in microbial fuel cell configurations reinforces the need for continued pursuit of synthetic designs to improve the biotic/abiotic interface in bioelectronics.

Table of Contents

List of Figures and Tables

Chapter 1

Introduction

1.1 Background and Motivation: Electric Avenues

In 1791 Luigi Galvani, professor of anatomy at Bologna, founded the concept of "animal" or biological electricity. In his now famous experiment, Galvani observed the twitching of a dissected frog's leg when the nerves and muscle were spanned by metal probes.[1] However, it was Alessandro Volta, professor of physics at Pavia, who suspected that the dissimilar metal objects involved were responsible for the flow of current through the tissue. He called this "metallic" electricity. Volta demonstrated his theory with the creation of the first chemical electric battery and named the phenomenon "Galvanism" after Galvani.[2] Through these scientific endeavors, the fields of electrophysiology and electrochemistry were born.

The first instance of microbial bioelectricity was published in 1911, when M. C. Potter reported on the electromotive force developed during the "disintegration of organic compounds by microorganisms."[3] His experiments on microbial-induced electrode reduction led to the development of biofuel cells, later termed "microbial fuel cells." In 1964, Duca and Fuscoe explained the thermodynamics behind bioelectrochemical energy conversion.[4]

They also suggested four general areas for microbial electrochemical technologies: detectors for contaminants, sensors for the generation of control signals, as power sources, and as catalysts for the generation of electrochemical reactions.[4] With the isolation of microbes called exoelectrogens that could directly reduce external insoluble electron acceptors in the 1990s, mediatorless microbial fuel cells were possible and kicked off further research into microbial bioelectronics.[5–7]

All microbial bioelectrochemical systems (BESs) are dependent on the wiring of microbial metabolism to solid-state electrodes. Exoelectrogenic microbes exchange electron equivalents with an electrode via extracellular electron transfer (EET) at the biotic/abiotic interface. The rate of electron exchange between microbe and electrode directly impacts the power generation, turnover frequency, and selectivity of BESs. Three distinct pathways for EET are known: (a) direct electron transfer (DET) via outer membrane-bound redox active proteins, (b) through conductive appendages such as pili, and (c) indirectly through the secretion of redox-active electron shuttles called mediated electron transfer (MET).[8–11] The specific type of electron transfer can be distinguished by their characteristic electrochemical potentials in cyclic voltammetry.

Approaches to improve electronic coupling at the biotic/abiotic interface include genetic modification of microbes,[12–16] addition of conductive coatings or interfacial mediators to the cell or electrode,[17–20] and whole bioelectrode fabrication.[20–22] One underdeveloped approach is the use of water soluble organic semiconductors to modify the biotic/abiotic interface. Beginning ten years ago, the development of membrane-intercalating conjugated oligoelectrolytes with phenylene-vinylene cores has seen the boost of biocurrent collection by increased electrode colonization, membrane permeabilization, and coulombic

efficiency.[11,23–28] More recently, addition of physiologically relevant redox-units to COEs has added another level of interaction between the microbes and the electrode.[29] Additionally, a conjugated polyelectrolyte (CPE) was shown to modify the surface of an electrode for increased colonization and DET.[30] The studies outlined in this dissertation allow us to understand how redox-active COEs and CPEs can be used to *tune* microbial electronic communication for enhanced bioelectrochemical conversion.

1.2 Outline

In Chapter 2, ferrocene-containing membrane-intercalating conjugated oligoelectrolytes were added to anaerobic microbial three-electrode electrochemical cells (M3Cs) containing the model exoelectrogen *Shewanella oneidensis* MR-1 to evaluate their ability to participate in biocatalytic current production. Electrochemical, metabolic, and spectroscopic techniques were used to show COEs functioned as an additional conduit for microbial extracellular electron transfer and that solely the applied potential can be used to modulate electron extraction from microbes.

In Chapter 3, the effect of hydration on the mixed conduction properties of the self-p-doped cyclopentadithiophene-*alt*-benzothiadiazole conjugated polyelectrolyte with pendant sulfonate groups (called CPE-K) is investigated. Both the electronic and ionic conductivity increased with hydration in CPE-K films. Electronic hole conduction increased partially due to growth of the radical cation population, but was mainly attributed to a shift in the π-π stacking to closer packing distances. Hydrated films also showed enhancement in the lamellar crystal correlation length indicating larger, more perfectly ordered crystallites.

In Chapter 4, we show that CPE-K functions as a conductive matrix to electronically connect a three-dimensional network of *S. oneidensis* MR-1 to a gold electrode in M3Cs,

thereby increasing biocurrent ~150-fold over control biofilms in M3Cs. While increased biocurrent is due to more cells in communication with the electrode, current extracted per cell is also enhanced indicating efficient long-range electron transport. Further, biocomposites show almost an order-of-magnitude lower charge transfer resistance than CPE-K alone, supporting that the electroactive bacteria and the conjugated polyelectrolyte work synergistically towards creating an effective bioelectronic composite to interface with the charge collecting electrode.

In Chapter 5, the *S. oneidensis* MR-1/CPE-K bioelectronic composites are tested in microbial fuel cells (MFCs) to see if they can operate autonomously. Under steady-state operation with a constant external load, only ~22-fold biocurrent enhancement is seen over controls (compared to ~150-fold in poised-potential M3Cs). Polarization testing shows the biocomposites can generate ~65% higher maximum power density than control biofilms. Testing of the anode potential during MFC operation supports that there is not enough natural driving force to electrochemically activate the CPE-K network.

1.3 Permissions

Parts of this dissertation are reproduced (adapted) in part with permission from:

1. McCuskey, S. R.; Rengert Z. D.; Zhang, M.; Helgeson, M. E.; Nguyen T.-Q.; Bazan G. C. Tuning the Potential of Electron Extraction from Microbes with Ferrocene-Containing Conjugated Oligoelectrolytes. *Advanced Biosystems* **3**, 1800303 (2018). DOI: 10.1002/adbi.201800303. Reproduced by permission of John Wiley and Sons.

2. McCuskey, S. R.; Su, Y.; Leifert, D.; Moreland, A. S.; Bazan, G. C. "Living Bioelectrochemical Composites. *Advanced Materials* **1908178**, 1908178 (2020). Reproduced by permission of John Wiley and Sons.

3. McCuskey, S. R.; Mostert, A. B.; Seifrid, M.; Danielsen, S. P. O.; Bazan, G. C. Hydration increases both electronic and ionic conduction in self-doped conjugated polyelectrolytes. In preparation. To allow for publication of this manuscript and permissions for its use to be granted, publication of this dissertation was embargoed.

4. McCuskey, S. R.; Llanes, L. C.; Su, Y.; Leifert, D.; Bazan, G. C. Self-doped Conjugated Polyelectrolytes in Microbial Fuel Cells. In preparation. To allow for publication of this manuscript and permissions for its use to be granted, publication of this dissertation was embargoed.

1.4 References

(1) Galvani, L.; Roller, D. H. D. Commentary on the Effect of Electricity on Muscular Motion. *Am. J. Phys.* **1954**, *22* (1), 40–40. https://doi.org/10.1119/1.1933610.

(2) Cajavilca, C.; Varon, J.; Sternbach, G. L. Luigi Galvani and the Foundations of Electrophysiology. *Resuscitation* **2009**, *80* (2), 159–162. https://doi.org/10.1016/j.resuscitation.2008.09.020.

(3) Potter, M. C. Electrical Effects Accompanying the Decomposition of Organic Compounds. *Proc. R. Soc. B Biol. Sci.* **1911**, *84* (571), 260–276. https://doi.org/10.1098/rspb.1911.0073.

(4) Del Duca, M. G.; Fuscoe, J. M. *Thermodynamics and Applications of Bioelectrochemical Energy Conversion Systems*; 1964.

(5) Lovley, D. R.; Stolz, J. F.; Nord, G. L.; Phillips, E. J. P. Anaerobic Production of Magnetite by a Dissimilatory Iron-Reducing Microorganism. *Nature* **1987**, *330* (6145), 252–254. https://doi.org/10.1038/330252a0.

(6) Venkateswaran, K.; Moser, D. P.; Dollhopf, M. E.; Lies, D. P.; Saffarini, D. A.; MacGregor, B. J.; Ringelberg, D. B.; White, D. C.; Nishijima, M.; Sano, H.; Burghardt, J.; Stackebrandt, E.; Nealson, K. H. Polyphasic Taxonomy of the Genus

Shewanella and Description of Shewanella Oneidensis Sp. Nov. *Int. J. Syst. Bacteriol.* **1999**, *49* (2), 705–724. https://doi.org/10.1099/00207713-49-2-705.

(7) Chaudhuri, S. K.; Lovley, D. R. Electricity Generation by Direct Oxidation of Glucose in Mediatorless Microbial Fuel Cells. *Nat. Biotechnol.* **2003**, *21* (10), 1229–1232. https://doi.org/10.1038/nbt867.

(8) Renslow, R.; Babauta, J.; Kuprat, A.; Schenk, J.; Ivory, C.; Fredrickson, J.; Beyenal, H. Modeling Biofilms with Dual Extracellular Electron Transfer Mechanisms. *Phys. Chem. Chem. Phys.* **2013**, *15* (44), 19262–19283. https://doi.org/10.1039/c3cp53759e.

(9) Babanova, S.; Bretschger, O.; Roy, J.; Cheung, A.; Artyushkova, K.; Atanassov, P. Innovative Statistical Interpretation of Shewanella Oneidensis Microbial Fuel Cells Data. *Phys. Chem. Chem. Phys.* **2014**, *16* (19), 8956–8969. https://doi.org/10.1039/c4cp00566j.

(10) Babanova, S.; Cornejo, J.; Roy, J. N.; Babanova, S.; Garcia, K. E.; Cornejo, J.; Ista, L. K.; Atanassov, P. Catalytic Biofilm Formation by Shewanella Oneidensis MR-1 and Anode Characterization by Expanded Uncertainty. *Electrochim. Acta* **2017**, *126* (July 2013), 3–10. https://doi.org/10.1016/j.electacta.2013.07.075.

(11) Kirchhofer, N. D.; Chen, X.; Marsili, E.; Sumner, J. J.; Dahlquist, F. W.; Bazan, G. C. The Conjugated Oligoelectrolyte DSSN+ Enables Exceptional Coulombic Efficiency via Direct Electron Transfer for Anode-Respiring Shewanella Oneidensis MR-1-a Mechanistic Study. *Phys. Chem. Chem. Phys.* **2014**, *16* (38), 20436–20443. https://doi.org/10.1039/c4cp03197k.

(12) TerAvest, M. A.; Ajo-Franklin, C. M. Transforming Exoelectrogens for Biotechnology Using Synthetic Biology. *Biotechnol. Bioeng.* **2016**, *113* (4), 687–697. https://doi.org/10.1002/bit.25723.

(13) Choi, D.; Lee, S. B.; Kim, S.; Min, B.; Choi, I.; Chang, I. S. Metabolically Engineered Glucose-Utilizing Shewanella Strains under Anaerobic Conditions. *Bioresour. Technol.* **2014**, *154*, 59–66. https://doi.org/10.1016/j.biortech.2013.12.025.

(14) Nakagawa, G.; Kouzuma, A.; Hirose, A.; Kasai, T.; Yoshida, G. Metabolic Characteristics of a Glucose- Utilizing Shewanella Oneidensis Strain Grown under Electrode-Respiring Conditions. **2015**, 1–14. https://doi.org/10.1371/journal.pone.0138813.

(15) Yang, Y.; Ding, Y.; Hu, Y.; Cao, B.; Rice, S. A.; Kjelleberg, S.; Song, H. Enhancing Bidirectional Electron Transfer of Shewanella Oneidensis by a Synthetic Flavin Pathway. *ACS Synth. Biol.* **2015**, *4* (7), 815–823. https://doi.org/10.1021/sb500331x.

(16) Kouzuma, A.; Oba, H.; Tajima, N.; Hashimoto, K.; Watanabe, K. Electrochemical Selection and Characterization of a High Current-Generating Shewanella Oneidensis Mutant with Altered Cell-Surface Morphology and Biofilm-Related Gene Expression.

2014, 1–11.

(17) Kumar, R.; Singh, L.; Zularisam, A. W. Exoelectrogens: Recent Advances in Molecular Drivers Involved in Extracellular Electron Transfer and Strategies Used to Improve It for Microbial Fuel Cell Applications. *Renew. Sustain. Energy Rev.* **2016**, *56*, 1322–1336. https://doi.org/10.1016/j.rser.2015.12.029.

(18) Patil, S. a; Hasan, K.; Leech, D.; Hägerhäll, C.; Gorton, L. Improved Microbial Electrocatalysis with Osmium Polymer Modified Electrodes. *Chem. Commun.* **2012**, *48* (82), 10183. https://doi.org/10.1039/c2cc34903e.

(19) Park, S.; Kang, Y. J.; Majd, S. A Review of Patterned Organic Bioelectronic Materials and Their Biomedical Applications. *Adv. Mater.* **2015**, 7583–7619. https://doi.org/10.1002/adma.201501809.

(20) Qiao, Y.; Li, C. M.; Bao, S.-J.; Bao, Q.-L. Carbon Nanotube/Polyaniline Composite as Anode Material for Microbial Fuel Cells. *J. Power Sources* **2007**, *170* (1), 79–84. https://doi.org/10.1016/j.jpowsour.2007.03.048.

(21) Cai, W.; Liu, W.; Han, J.; Wang, A. Enhanced Hydrogen Production in Microbial Electrolysis Cell with 3D Self-Assembly Nickel Foam-Graphene Cathode. *Biosens. Bioelectron.* **2016**, *80*, 118–122. https://doi.org/10.1016/j.bios.2016.01.008.

(22) Yong, Y.-C.; Dong, X.-C.; Chan-Park, M. B.; Song, H.; Chen, P. Macroporous and Monolithic Anode Based on Polyaniline Hybridized Three-Dimensional Graphene for High-Performance Microbial Fuel Cells. *ACS Nano* **2012**, *6* (3), 2394–2400. https://doi.org/10.1021/nn204656d.

(23) Garner, L. E.; Park, J.; Dyar, S. M.; Chworos, A.; Sumner, J. J.; Bazan, G. C. Modification of the Optoelectronic Properties of Membranes via Insertion of Amphiphilic Phenylenevinylene Oligoelectrolytes. *J. Am. Chem. Soc.* **2010**, *132* (29), 10042–10052. https://doi.org/10.1021/ja1016156.

(24) Hou, H.; Chen, X.; Thomas, A. W.; Catania, C.; Kirchhofer, N. D.; Garner, L. E.; Han, A.; Bazan, G. C. Conjugated Oligoelectrolytes Increase Power Generation in E. Coli Microbial Fuel Cells. *Adv. Mater.* **2013**, *25* (11), 1593–1597. https://doi.org/10.1002/adma.201204271.

(25) Garner, L. E.; Thomas, A. W.; Sumner, J. J.; Harvey, S. P.; Bazan, G. C. Conjugated Oligoelectrolytes Increase Current Response and Organic Contaminant Removal in Wastewater Microbial Fuel Cells. *Energy Environ. Sci.* **2012**, *5* (11), 9449–9452. https://doi.org/10.1039/c2ee22839d.

(26) Thomas, A. W.; Garner, L. E.; Nevin, K. P.; Woodard, T. L.; Franks, A. E.; Lovley, D. R.; Sumner, J. J.; Sund, C. J.; Bazan, G. C. A Lipid Membrane Intercalating Conjugated Oligoelectrolyte Enables Electrode Driven Succinate Production in Shewanella. *Energy Environ. Sci.* **2013**, *6* (6), 1761.

https://doi.org/10.1039/c3ee00071k.

(27) Yan, H.; Catania, C.; Bazan, G. C. Membrane-Intercalating Conjugated Oligoelectrolytes: Impact on Bioelectrochemical Systems. *Adv. Mater.* **2015**, *27* (19), 2958–2973. https://doi.org/10.1002/adma.201500487.

(28) Catania, C.; Ajo-franklin, C. M.; Bazan, G. C. Membrane Permeabilization by Conjugated Oligoelectrolytes Accelerates Whole-Cell Catalysis. *RSC Adv.* **2016**, *6*, 100300–100306. https://doi.org/10.1039/C6RA23083K.

(29) Kirchhofer, N. D.; Rengert, Z. D.; Dahlquist, F. W.; Nguyen, T.-Q.; Bazan, G. C. A Ferrocene-Based Conjugated Oligoelectrolyte Catalyzes Bacterial Electrode Respiration. *Chem* **2017**, *2* (2), 240–257. https://doi.org/10.1016/j.chempr.2017.01.001.

(30) Kirchhofer, N. D.; McCuskey, S. R.; Mai, C.-K.; Bazan, G. C. Anaerobic Respiration on Self-Doped Conjugated Polyelectrolytes: Impact of Chemical Structure. *Angew. Chemie Int. Ed.* **2017**, *56* (23), 6519–6522. https://doi.org/10.1002/anie.201701964.

Chapter 2

Tuning the Potential of Electron Extraction from Microbes with Ferrocene-Containing Conjugated Oligoelectrolytes

Synthetic systems that facilitate electron transport across cellular membranes are of interest in bioelectrochemical technologies such as bioelectrosynthesis, waste water remediation, and microbial fuel cells. The design of a second generation redox-active conjugated oligoelectrolyte (COE) bearing terminal cationic groups and a π-delocalized core capped by two ferrocene units is reported. The two COEs, DVFBO and F_4-DVFBO, have similar membrane affinity, but fluorination of the core results in a higher oxidation potential (422 ± 5 mV compared to 365 ± 4 mV vs Ag/AgCl for the neutral precursors of F_4-DVFBO and DVFBO in chloroform). Concentration-dependent aggregation is suggested by zeta potential measurements and confirmed by examination by cryo-TEM. When the working electrode is poised below the oxidation potential of the COEs (E_{CA} = 200 mV) in three-electrode electrochemical cells containing *Shewanella oneidensis* MR-1, addition of DVFBO and F_4-DVFBO produces negligible biocurrent enhancement compared to controls. At E_{CA} = 365 mV, DVFBO increases steady-state biocurrent by 67±12% relative to controls, while the

increase with F_4-DVFBO is 30±5%. Cyclic voltammetry supports that DVFBO increases catalytic biocurrent and that F_4-DVFBO has less impact, consistent with their oxidation potentials. The overall effect is the ability to modulate electron transfer from microbial species via tailoring of the COE redox properties.

2.1 Introduction

Bioelectrochemical systems (BESs, for listing of all abbreviations, please see end of Experimental Section) rely on exoelectrogenic microbes that can exchange electrons with an electrode and thereby have the ability to generate electricity from organic waste or generate products through the process of bioelectrosynthesis.[1–3] The functional activity of bacteria in these devices is determined by the efficiency of interfacial charge transfer between the cells and the electrode.[1,2,4] Three distinct pathways for extracellular electron transfer (EET) are commonly described to occur in nature: (a) direct electron transfer via transmembrane redox-active proteins, (b) through conductive appendages such as pili, and (c) indirectly through the secretion of redox-active electron shuttles.[5–8] The specific type of electron transfer can be distinguished in cyclic voltammetry (CV) by their characteristic electrochemical potentials.[9,10]

Different approaches have been explored to improve electron transfer across biotic/abiotic interfaces. These methods include genetic modification of microbes, addition of conductive coatings or interfacial mediators to the electrode, and bioelectrode fabrication.[11–13] Research into synthetic biology of bacteria aims to add useful pathways characteristic of exoelectrogenic microbes and introduce EET to microbes already containing other useful processes.[14–16] These strategies have had success in improving

biocurrent production and enabling microbial electrosynthesis, but require organism-specific programming and have only been extended to a few species.

Another means that directly modifies microorganisms is the implementation of synthetic ion channels and/or transmembrane electron transporters with structures that facilitate the passage of charged species through the hydrophobic lipid bilayer of cell membranes.[17–19] Conjugated oligoelectrolytes (COEs) are one class of these materials and they are described by a π-delocalized backbone with appended ionic functionalities that afford solubility in polar solvents.[20–23] COEs have been implemented into biosensor applications and their intermolecular contacts enforced by hydrophobic effects have been correlated with different morphologies in solution.[24–30] COEs have also shown to improve biocurrent generation and whole cell catalysis by increasing ion conductance across the membrane and allowing the release of periplasmic enzymes.[12,31]

A redox-active COE containing a single ferrocene unit, abbreviated as DSFO+ (**Figure 2.1a**), was recently found to increase biologically-derived current in microbial three-electrode electrochemical cells (M3Cs) by mimicking the function of native redox-active transmembrane proteins.[32] When operating M3Cs at the oxidation potential of DSFO+ (270 mV vs Ag/AgCl), current amplification arose from an increase in the coulombic efficiency and current collected per cell. Examination by CV revealed that the increase in current is not due to direct/mediated electron transfer mechanisms through membrane proteins or flavins, respectively, but rather through a process that relies on the redox properties of DSFO+.

In this contribution we report a second generation of redox-active COEs specifically designed to include an additional ferrocene unit per inserted molecule and to allow understanding of the impact of changes in their oxidation potential. The design of the new

molecules, namely DVFBO and F_4-DVFBO, in Figure 2.1a extends the dimensionality of DSFO+, while reducing the number of charged groups per molecule in order to increase the driving force for association with the membrane. Cell association and minimum inhibitory concentration windows of DVFBO and F_4-DVFBO were investigated with *S. oneidensis* MR-1, a well-characterized exoelectrogen. Results presented here include application of the COEs in microbial three-electrode electrochemical cells to evaluate their effect on microbial EET. Finally, we demonstrate that the oxidation potential of the COE can indeed be used to modulate electron extraction from *S. oneidensis* MR-1.

2.2 Synthesis and Characterization

The synthesis of DVFBO, see **Figure 2.1b**, starts with building the internal conjugated core by using 1 and 2a, affording the bis-aldehyde terminated core 3a in 90% yield. An analogous reaction towards F_4-DVFBO with the tetrafluorinated bis(diethylphosphonate) compound 2b proceeds in a similar manner, except the isolated yield of 3b was 60%. We attribute the lower yield of this transformation to the stabilization and resulting lower nucleophilicity of the anion of 2b as a result of fluorination. Reduction using sodium borohydride and 10 mole % methanol in 1,2-dichloroethane (DCE) afforded bis-diols 4a and 4b in 99% and 89% yield, respectively. Acid-catalyzed condensation reaction of 4a or 4b with 6-bromo-1-hexanol in the presence of catalytic acid affords 5a and 5b in 55% and 45% yield, respectively. After a Finkelstein reaction to exchange the pendant alkyl bromides for iodides, target compounds DVFBO and F_4-DVFBO were generated by reaction with an excess of trimethylamine. Complete details of the synthetic procedures and characterization of compounds DVFBO, F_4-DVFBO, together with all intermediates, can be found in the Supporting Information.

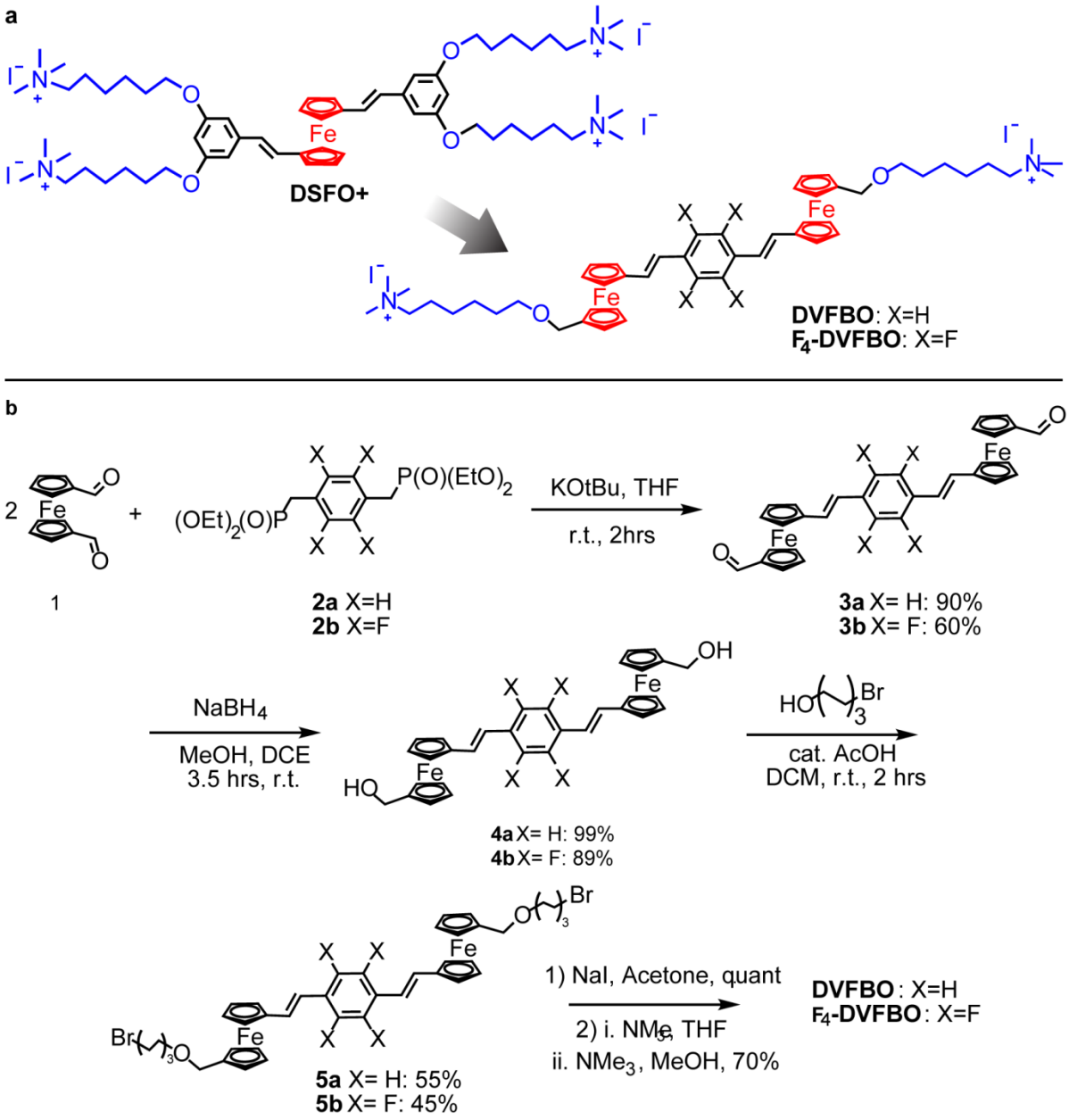

Figure 2.1: Redox-active COEs. a) Structural evolution of redox-active COEs. b) Synthesis of DVFBO and F_4-DVFBO**.**

To first ascertain the properties of the conjugated core of DVFBO and F_4-DVFBO, we investigated the optical and electrochemical features of the non-ionic precursors 5a and 5b in chloroform. The dielectric constant of chloroform is similar to that of a lipid bilayer membrane (ε_{CHCl3} = 4.8, $\varepsilon_{membrane} \approx 5$).[33] As expected, the optical properties of 5a and 5b are

similar due to the fact the fluorination of the internal benzene ring of 5a results in an inductive withdrawing effect but little resonance delocalization.[34] The absorption maximum (λ_{max}) for 5a occurs at 352 nm; fluorination of the core causes the λ_{max} of 5b to red shift by only 2 nm (see **Figure 2.S2**). This peak is assigned to a π to π* transition, which is similar to that of COEs of similar molecular length, but without a ferrocene unit, in both peak wavelength and molar absorptivity.[34] There exists a lower energy and lower intensity peak at ~470 nm in both molecules that is assigned to a metal to ligand charge transfer (MLCT) band typical of ferrocenes.[35] Examination of this lower energy peak reveals a more significant red shift of 19 nm upon fluorination of the core in 5b, an indication that suggests fluorination of the internal core increases delocalization in the anti-bonding ligand orbital of the MLCT transition.[36] No emission could be detected under any experimental conditions using a standard fluorimeter. The optical features described for 5a and 5b in chloroform are essentially the same as those observed for DVFBO and F_4-DVFBO in aqueous media (Figure 2.S2).

Similarities in the optical properties are contrasted by their different electrochemical features. **Figure 2.2a** shows the normalized traces of 5a and 5b at 100 μM in chloroform at 25^{o}C, as determined by differential pulse voltammetry (DPV). Voltammograms in chloroform were measured against the non-aqueous reference electrode Ag/$AgNO_3$ (0.01 M acetonitrile) and converted to Ag/AgCl (saturated KCl) for understanding subsequent microbial electrochemical experiments, please see the Experimental Section for details.[37,38] Fluorination of the internal phenylene ring raises the first oxidation step from 365 ± 4 mV in 5a, to 422 ± 5 mV in 5b (all potentials will be reported vs Ag/AgCl in saturated KCl).[39] **Figure 2.2b** provides normalized DPV traces of DVFBO and F_4-DVFBO under dilute

conditions as measured in aqueous media (100 mM phosphate buffer (PB), pH 7.2). At 1 μM and 25 ^{o}C, fluorination of the backbone raises the oxidation potential from 330 mV in DVFBO to 438 mV in F_4-DVFBO and the general features of these traces closely resemble those of 5a/5b in chloroform. However, one observes additional signals at more positive potentials as the concentrations of DVFBO and F_4-DVFBO are increased, which we attribute to aggregation (see **Figure 2.S3** for DPV traces).

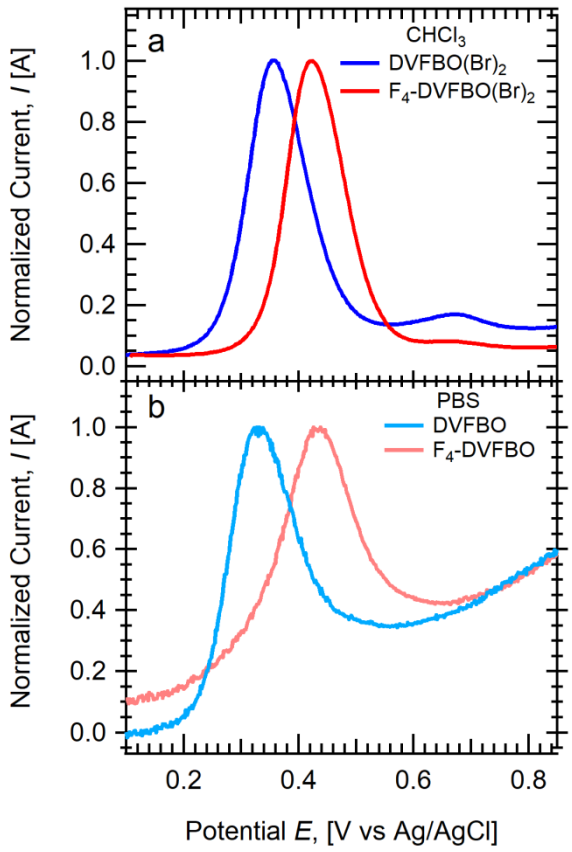

Figure 2.2: DPV traces of DVFBO and F_4-DVFBO in different solvents. a) 100 μM 5a (blue trace) and 100 μM 5b (red trace) in CHCl3 at 25 ˚C, b) 1 μM DVFBO (light blue trace) and 1 μM F4-DVFBO (light red trace) in PB at 25 ˚C. All traces are normalized relative to the highest intensity feature.

An aggregate or micellar structure should afford a detectable signal from a zeta potential (ZP) measurement, as the hydrophobic core of the molecule would be surrounded by the

tethered cationic functionalities.[40–42] When the zeta potential of solutions containing DVFBO or F_4-DVFBO in PB were measured as a function of concentration, solutions of DVFBO show an increase in ZP as a function of concentration and a plateau at ~20 mV above 40 μM, while for F_4-DVFBO this plateau occurs at ~15 mV above 10 μM (**Figure 2.S5**).[43,44]

Cryogenic transmission electron microscopy (cryo-TEM) was used to visualize any aggregates and ascertain their morphological features in solution. The cryo-TEM study of 100 μM DVFBO in deionized water revealed a high degree of supramolecular order in the form of ribbon-like structures, which persist across micron length scales (**Figure 2.3a**). However, cryo-TEM images of DVFBO (Figure 2.3b) and F_4-DVFBO (Figure 2.3c) in PB show aggregates with considerably less order. Their features resemble clusters of approximately 100 nm that are composed of smaller spherical micelle-like structures. These differences in structure are attributed to the ionic strength of the medium, which acts by affecting interactions between charged molecules in solution through the screening of charges.[45,46]

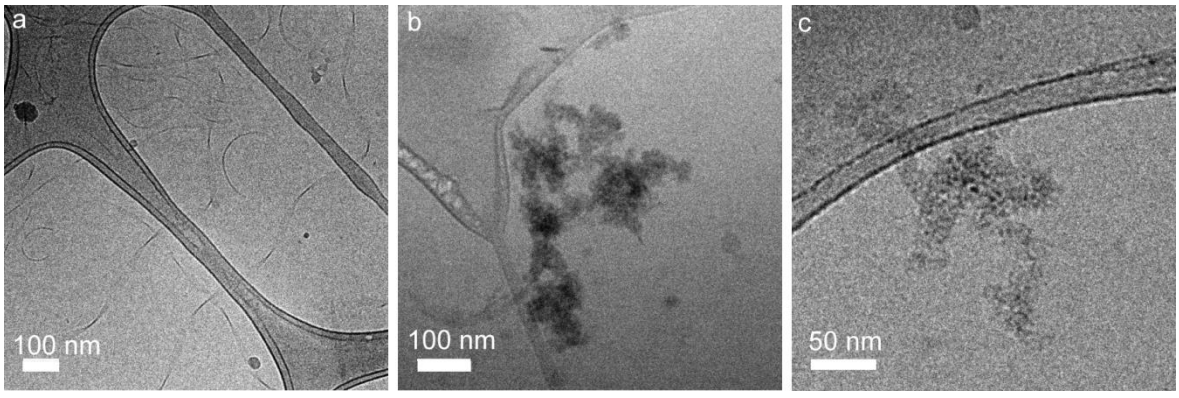

Figure 2.3: Cryo-TEM images of (a) DVFBO in H_2O, (b) DVFBO in PB, and (c) F_4-DVFBO in PB.

2.3 Microbial Electrochemical Characterization

Minimum inhibitory concentrations (MIC) and associations of DVFBO and F_4-DVFBO with bacteria were investigated prior to microbial electrochemical testing. The dilution method was used to determine the susceptibility of *S. oneidensis* MR-1 to DVFBO and F_4-DVFBO. Cells were tested for their ability to produce visible growth when exposed to a logarithmic concentration series of the COEs.[47] The MIC of both DVFBO and F_4-DVFBO was determined to be 11.25 μM, see **Figure 2.S6**. To measure association of the COEs with the cells, concentrations in the range of 0-50 μM of both molecules were incubated with liquid cultures at 0.4 OD_{600} for 1 hour at 30 ˚C. After cell removal by centrifugation, the absorbance of the supernatant was compared to controls. **Figure 2.S7** shows that both DVFBO and F_4-DVFBO associate nearly quantitatively with *S. oneidensis* MR-1.

We now discuss to what extent DVFBO and F_4-DVFBO impact electron harvesting from *S. oneidensis* MR-1 by using microbial three-electrode electrochemical cells (M3Cs). M3Cs allow one to measure biocurrent over time using chronoamperometry (CA) at a given electrode potential (E_{CA}) and investigate mechanisms of enhancement through cyclic voltammetry (CV). We utilized carbon felt working electrodes, titanium counter electrodes, and Ag/AgCl reference electrodes (saturated KCl). Full experimental details are provided in the Experimental Section.

To examine whether it is possible to tune the electron extraction from *S. oneidensis* MR-1 based on the oxidation potential of the COE, DVFBO and F_4-DVFBO were tested in M3Cs poised at two different potentials: E_{CA} = 200 mV and E_{CA} = 365 mV. **Figure 2.5** shows a schematic representation of the available biocurrent pathways at the these E_{CA} values. Oxidizing the ferrocene centers in the COE structures enables them to participate in

metabolic electron transfer from inside of the cell out to the working electrode electron acceptor. The Nernst equation (**Equation 2.1**) relates the oxidation potential (E°_{ox}) of the molecules to the electrode potential E_{CA}, temperature T, and species activities (here approximated as concentrations):

$$E_{\mathrm{CA}} = E^{\circ}_{\mathrm{ox}} - \frac{RT}{F} \ln \frac{[\mathrm{Red}]}{[\mathrm{Ox}]} \tag{2.1}$$

where R is the gas constant and F is Faraday's constant. At E_{CA} = 200 mV, a negligible fraction of DVFBO and F_4-DVFBO is oxidized and available for ferrocene-mediated electron transport across the membrane. At E_{CA} = 365 mV the poised potential of the working electrode matches the oxidation potential of DVFBO in chloroform, an environment akin to the membrane in terms of dielectric constant, giving the expected ratio of reduced to oxidized species as 1:1, or 50% oxidized. The oxidation potential of F_4-DVFBO is higher at 422 ± 5 mV, affording only ~10% oxidation of the species. These approximations are based on dilute solutions and we expect that the variety of environments available to the molecules upon insertion into the membrane may shift this estimate of oxidized molecules.

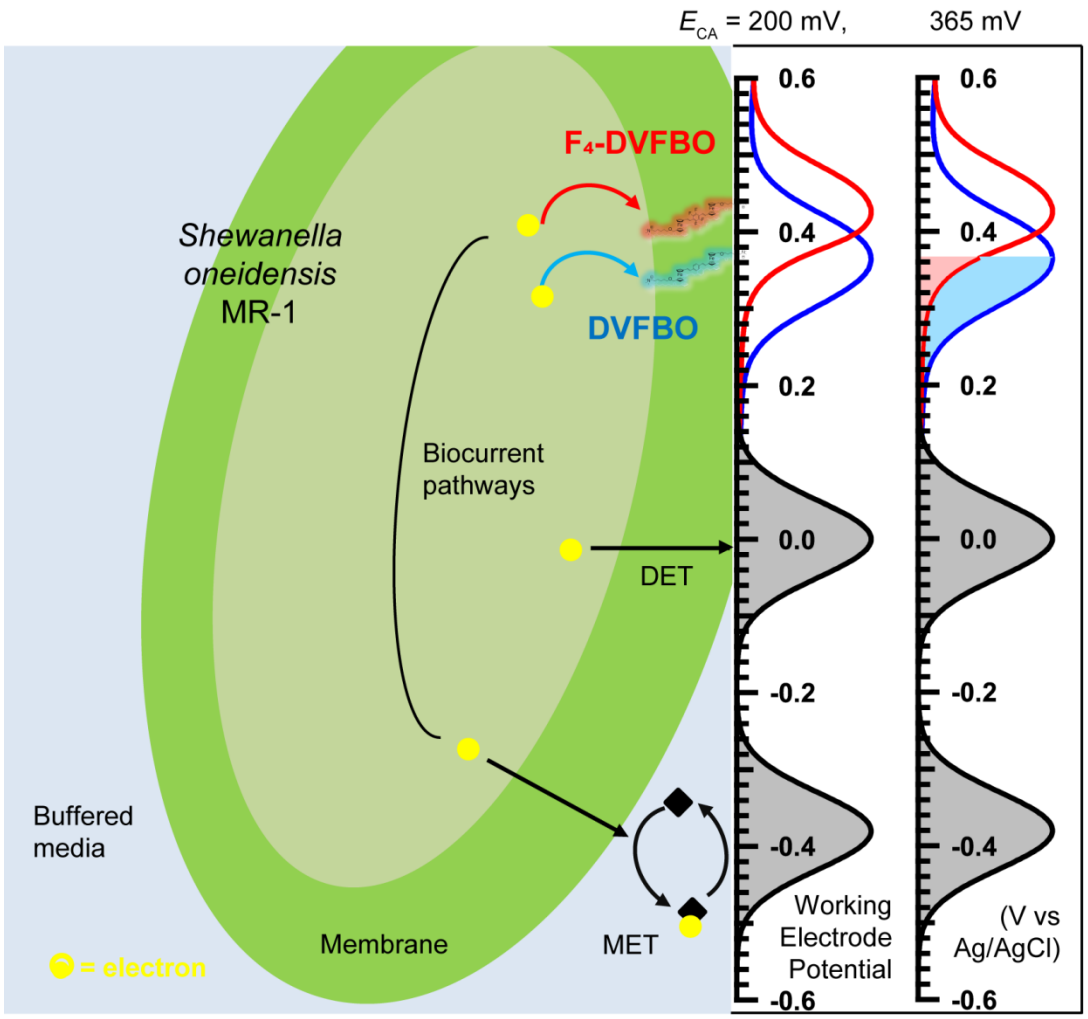

Figure 2.4: Schematic representation of biocurrent pathways available to *Shewanella oneidensis* MR-1.

To test the impact of E_{CA} and the oxidation potential of DVFBO and F_4-DVFBO on biocurrent production, biological replicate biofilms were grown on carbon felt working electrodes with lactate as the carbon source. **Figure 2.5** shows average current density, *J*, over time for E_{CA} = 200 mV and E_{CA} = 365 mV. From time point I to II biofilms are conditioned at the different potentials. Note that more current is collected at E_{CA} = 365 mV during biofilm growth and that DVFBO and F_4-DVFBO have negligible output when added to sterile controls with only growth media and lactate. At time point II, when the biofilms

reached steady-state current production, 7 µM DVFBO or 7 µM F_4-DVFBO from concentrated stock solutions were injected into M3Cs.

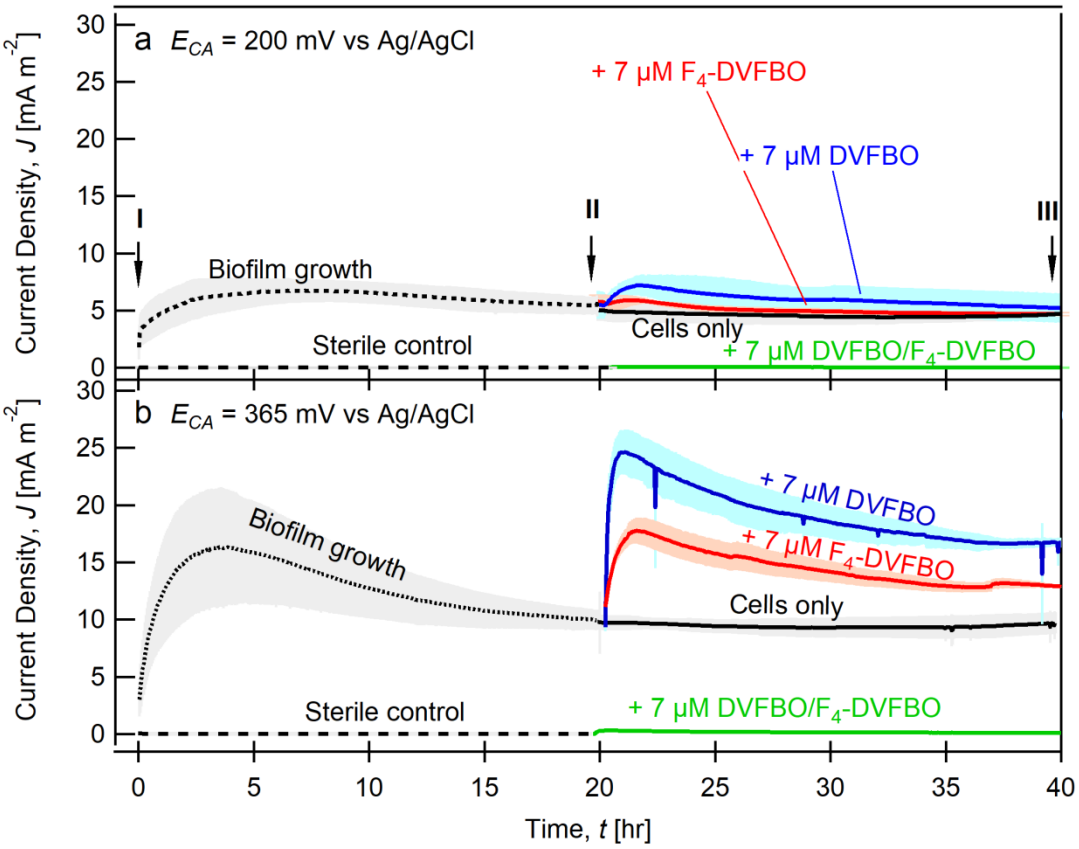

Figure 2.5: Average current density as a function of time (CA traces) for M3Cs poised at (a) E_{CA} = 200 mV vs Ag/AgCl, below the oxidation potential of DVFBO and F_4-DVFBO and at (b) E_{CA} = 365 mV vs Ag/AgCl, at the oxidation potential of DVFBO. Shaded areas represent ±1 std. dev. from the mean (n ≥ 3). Note the negligible current output from the sterile controls. (I) Inoculation of the reactors with *S. oneidensis* MR-1, CV, HPLC sample, and initiation of the current collection. (II) CV, addition of 7 µM DVFBO (blue trace and green trace) or 7µM F_4-DVFBO (red trace) to reactors. Black solid trace is positive control with only *S. oneidensis* MR-1, no added COEs. (III) HPLC sample and CV at the end of the current collection, followed by chemical cell fixation and SEM of the fixed electrode or biomass quantification.

Because DVFBO and F_4-DVFBO are largely in their neutral states at E_{CA} = 200 mV, the lower potential can be used to ascertain the effect of the physical presence of the molecules in the cell membranes.[48] Figure 2.5a shows that addition of DVFBO and F_4-DVFBO produces steady-state biocurrents (J_{SS}) of 5.1 ± 1 mA m^{-2} and 4.7 ± 0.1 mA m^{-2} (taken at t = 39 hr), respectively. Compared to the positive control (4.6 ± 0.3 mA m^{-2}) addition of the COEs at E_{CA} = 200 mV therefore does not significantly impact the biocurrent. However, when working electrodes are poised at E_{CA} = 365 mV, the addition of DVFBO increases steady-state current density from controls at 10 ± 1 mA m^{-2} to 16.7 ± 0.4 mA m^{-2}. Adding F_4-DVFBO leads to a steady-state current density of 13 ±1 mA m^{-2}. Put another way, one can achieve improvement levels of 67 ± 12% and 30 ± 5% over the positive controls from addition of DVFBO and F_4-DVFBO, respectively. Given that both COEs associate to the same extent with *S. oneidensis* MR-1 (**Figure 2.S7**), the difference in current density enhancement is most reasonably attributed to the difference in redox properties.

CV measurements were carried out at time points I, II, and III, i.e. before CA current collection, immediately before COE injection, and right after CA current collection. CV measurements can be used in bioelectrochemical experiments in order to determine to what degree current generated by the biofilm is catalytic or not. The potential range of -0.6 V ≤ E_{CV} ≤ 0.45 V vs Ag/AgCl was chosen to encompass the characteristic redox-potential ranges of flavin-based mediated electron transfer (MET, -0.4 V - 0 V), membrane-protein direct electron transfer (DET, 0 V - 0.2 V), and the expected electrochemical signals of the molecules 0.365 V (DVFBO) and 0.422 V (F_4-DVFBO).[7,9,48–50] By determining the contribution to the current from processes at different redox potentials, one can obtain an

estimate of the participation by the different mechanisms. A summary of these known and proposed biocurrent pathways is shown in Figure 2.4.

Figure 2.S8 shows average CV and derivative traces right after inoculation with bacteria and before the start of current collection (time point I in Figure 2.5). First derivative plots (*dJ/dE*) are also provided to identify relevant processes. For MET, the peak current density, J_p, is 0.5 ± 0.1 mA m^{-2}.[8,51–53] DET is seen with J_p = 1.2 ± 0.3 mA m^{-2}. **Figure 2.6a** shows that at time point II both MET and DET increase from time point I; this increase in *J* reflects the formation and conditioning of the biofilms. For E_{CA} = 200 mV, J_p = 2.7 ± 0.6 mA m^{-2} (MET) and J_p = 4.2 ± 0.5 mA m^{-2} (DET). For E_{CA} = 365 mV, we see J_p = 2.6 ± 0.6 mA m^{-2} (MET) and J_p = 4.7 ± 0.9 mA m^{-2} (DET). There is no change in the J_p values for the controls at time point III as seen in **Figure 2.6b** (E_{CA} = 200 mV, J_p = 2.5 ± 0.8 mA m^{-2} (MET), J_p = 4.6 ± 0.7 mA m^{-2} (DET); E_{CA} = 365 mV, J_p = 3.1 ± 0.5 mA m^{-2} (MET), J_p = 5.2± 0.7 mA m^{-2} (DET)). At all time points for control M3Cs, the current measured in CV is catalytic, as indicated by the sigmoidal shape of the curves. These data provide a baseline to compare possible mechanisms of enhancement in EET after addition of DVFBO and F_4-DVFBO.

Figure 2.6c and **2.6d** show CV and derivative data at time point III for M3Cs modified with DVFBO and F_4-DVFBO, respectively. The light traces correspond to E_{CA} = 200 mV, while the dark traces correspond to E_{CA} = 365 mV. The DET wave (E_{CV} = 0 V) will first be discussed. For F_4-DVFBO, J_p = 4.2 ± 0.6 mA m^{-2} (E_{CA} = 200 mV) and J_p = 5.3 ± 0.2 mA m^{-2} (E_{CA} = 365 mV). For DVFBO, J_p = 3.0 ± 0.6 mA m^{-2} (E_{CA} = 200 mV) and increases to J_p = 4.3 ± 0.3 mA m^{-2} (E_{CA} = 365mV). These values are invariable within error compared to the corresponding positive controls. The signal for DET thus remains unaffected when cells are

treated with DVFBO and F_4-DVFBO, which indicates that the COEs do not boost biocurrent production by increasing transport through the native membrane proteins.

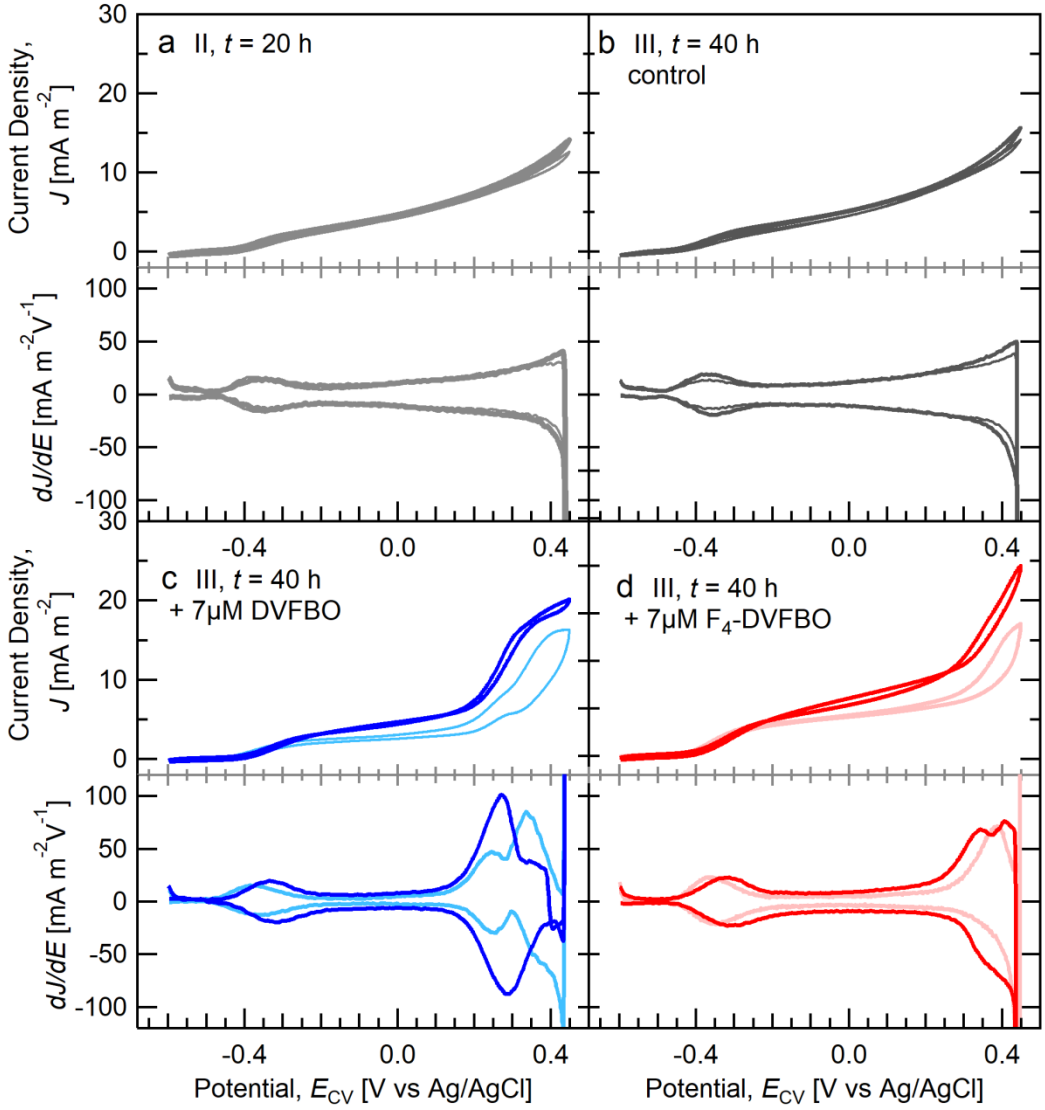

Figure 2.6: Average (n ≥ 3) CV and *dJ/dE* outputs from *S. oneidensis* MR- 1 EET. Scan rate: 5 mV s^{-1}. Corresponding to CA experiments performed at E_{CA} = 200 mV (light traces) and at E_{CA} = 365 mV (dark traces) (a) at time point II, t = 20 hours, *S. oneidensis* MR-1 and no COEs and (b-d) after CA collection at time point III, t=40 h. (b) *S. oneidensis* MR-1 and no COEs. (c) 7 μM DVFBO and *S. oneidensis* MR-1. (d) 7 μM F_4-DVFBO and *S. oneidensis* MR-1.

The MET wave is more distinguishable than the DET wave and ranges from -0.4 to -0.3 V. For F_4-DVFBO, the magnitudes of J_p are similar to each other (J_p = 3.2 ± 0.4 mA m^{-2}, E_{CA} = 200 mV; J_p = 3.6 ± 1.3 mA m^{-2}, E_{CA} = 365 mV). A slight increase occurs in MET with DVFBO (J_p = 2.3 ± 0.5 mA m^{-2}, E_{CA} = 200 mV; J_p = 3.1 ± 0.4 mA m^{-2}, E_{CA} = 365 mV). Worthy to highlight is the shift in the MET peak potential from E_{CV} = -367 mV to -309 mV for F_4-DVFBO modified cells and E_{CV} = -385 mV to -325 mV for DVFBO modified cells when E_{CA} is increased. This shift suggests a change in the flavin population from freely diffusing riboflavin and flavin mononucleotides to bound flavin species at the electrode surface.[8,50–55] Free-form flavins follow a two-electron redox reaction of quinone to hydroquinone, while bound flavins acting as cofactors at the cell/electrode interface allow for faster and more thermodynamically favorable one-electron transfer.[56,57] Because this shift in redox potential for MET is not seen for DVFBO and F_4-DVFBO modified *S. oneidensis* MR-1 at E_{CA} = 200 mV, it is possible that the oxidation of the COEs can stimulate transport through bound flavins, although further mechanistic evidence is required for full verification.

Of most relevance are the oxidation waves at $E_{CV} \geq 200$ mV in Figure 2.6c and 6d for M3Cs modified with DVFBO and F_4-DVFBO. These waves are not seen in the positive controls at time point III (Figure 2.6b). Most significantly one observes the appearance of redox waves that correlate to the E°_{ox} of the molecules in chloroform (Figure 2.2a). CV and derivative data after E_{CA} = 365 mV are seen in the darker traces. For F_4-DVFBO modified cells J_p =18.7 ± 1.6 mA m^{-2} (E_{CV} = 407 mV) and for DVFBO modified cells J_p = 19.5 ± 1.2 mA m^{-2} (E_{CV} = 367 mV). Additionally, the CV waves are sigmoidal in shape indicating catalytic transport though the molecules. At $E_{CV} = E_{CA}$ = 365 mV, J values increase by 27 ±

3% and 63 ± 8% for F_4-DVFBO and DVFBO modified M3Cs, respectively, when compared to the control (12.0 ± 0.6 mA m^{-2}). These percent increases in CV current density correlate to the percent increase in steady-state biocurrent production seen for COE modified cells at E_{CA} = 365 mV. This reveals that DVFBO and F_4-DVFBO are the primary pathways of increased current production and can act as conduits for extracellular electron transfer for *S. oneidensis* MR-1.

For biofilms evolved at E_{CA} = 200 mV, one also observes similar J due to transport via the COEs in the CV and derivative plots (Figure 2.6c and 2.6d, light traces). F_4-DVFBO modified cells show J_p = 13.3 ± 1.5 mA m^{-2} (E_{CV} = 385 mV), while DVFBO modified cells show J_p = 16.0 ± 1.8 mA m^{-2} (E_{CV} = 349 mV). It is worth clarifying that these pathways are not activated during chronoamperometry at E_{CA} = 200 mV, thus one observes no increase in the J_{SS} over the positive controls (Figure 2.5a). That more than one peak is observed at E_{CV} > 200 mV may be attributed to COEs in different environments within the lipid bilayer: 1) a COE dilute phase where the local environment comprises lipids, and 2) a COE rich phase where the molecules have ordered in close contact with each other.[58–63]

During M3C operation, *S. oneidensis* MR-1 theoretically generates four electrons for each equivalent of lactate oxidized to acetate by the following reaction (**Equation 2.2**)[5]

$$\text{Lactate}^- + 2\ H_2O \rightarrow \text{Acetate}^- + HCO_3^+ + 5\ H^+ + 4\ e^- \qquad (2.2)$$

Analysis of the charge collected during chronoamperometry (Q_{col}) relative to the maximum possible charge equivalents in the lactate consumed by the bacteria (Q_{lac}) defines the coulombic efficiency (CE) of the M3Cs as shown in **Equation 2.3**,[64]

$$CE = \frac{Q_{col}}{Q_{lac}} \times 100 \qquad (2.3)$$

The values and expressions used to calculate *CE* are detailed in **Table 2.S1.** The average *CE* for positive control M3Cs poised at E_{CA} = 200 mV was 34 ± 3 %, while it was found to be 89 ± 23 % and 45 ± 1 % with added DVFBO and F_4-DVFBO, respectively. The Q_{col} is similar for all conditions, but the change in lactate concentration is higher for untreated cells, perhaps reflecting that COEs impact the vitality of the cells. Therefore, the lower Q_{lac} leads to a higher *CE* for DVFBO and F_4-DVFBO. These *CE* values are similar to those reported when 1 µM of DSFO+ was added to *S. oneidensis* MR-1 at similar working electrode potentials.[32] The average *CE* for positive control M3Cs poised at E_{CA} = 365 mV was 82 ± 11 % while it was found to be 89 ± 23 % and 66 ± 10 % for M3Cs with added DVFBO and F_4-DVFBO, respectively. In this case, Q_{lac} is higher for DVFBO and F_4-DVFBO modified cells compared to the control, but one also observes higher Q_{col} compared to E_{CA} = 200 mV for all cases leading to higher *CE* values. This set of observations suggests that under conditions where electron transfer can take place any toxic side effect of the COE is compensated by the new avenue for electron transfer.

Representative SEM images of the carbon felt electrodes after electrochemical testing are shown in **Figure 2.7**. Biomass on each electrode was quantified via the Bradford protein assay method to reveal that electrode colonization was the same within error for each tested E_{CA} (Figure 2.7g). Similar electrode colonization suggests that DVFBO and F_4-DVFBO do not influence colonization and support that performance of the M3C is enhanced on a per cell basis by adding additional electron transfer conduits to the cell.

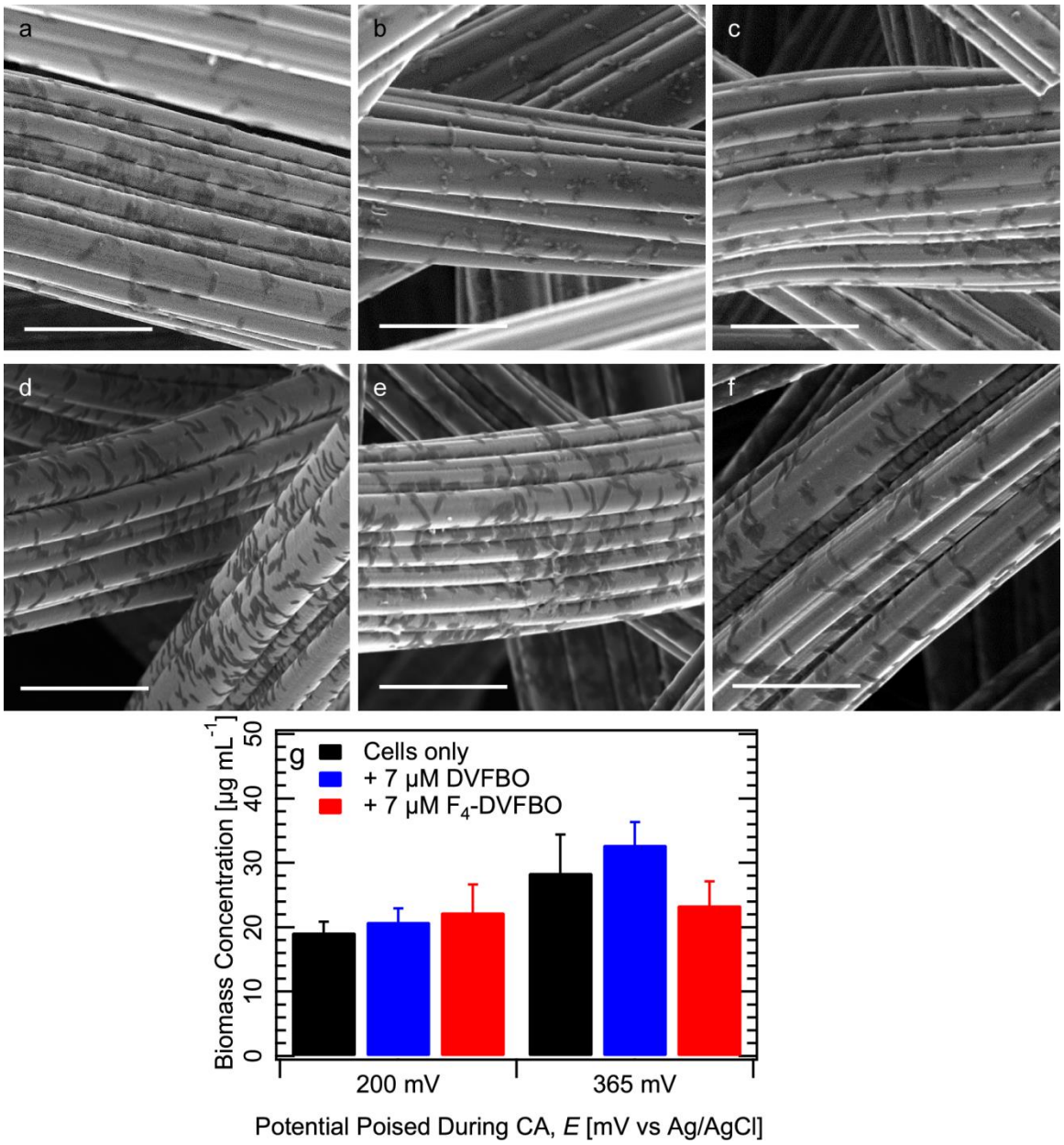

Figure 2.7: Representative SEM images of carbon fiber working electrodes with bacterial colonization and biomass quantification. Scale bars represent 20 μm. (a-c) electrodes from experiments at E_{CA} = 200 mV vs Ag/AgCl. (d-f) electrodes from experiments at E_{CA} = 365 mV vs Ag/AgCl. (a,d) S. oneidensis MR-1 and no COE. (b,e) 7 μM DVFBO and *S. oneidensis* MR-1. (c,f) 7 μM F_4-DVFBO and *S. oneidensis* MR-1. (g) Average biomass concentration for carbon felt working electrodes at each potential.

2.3 Conclusion

In dilute solution, the electrochemical properties of DVFBO and F_4-DVFBO behave in a conventional manner for isolated molecules, but at higher concentrations in aqueous media, aggregation gives rise to additional redox processes.[65,66] The driving force for this aggregation is akin to micelle formation in traditional surfactants, where the hydrophobic core of the molecule is shielded from interactions with the polar aqueous solvent. Changes in zeta potential as concentration increases as well as cryo-TEM images provide evidence of aggregation.

Because DVFBO and F_4-DVFBO have the same minimum inhibitory concentration and cell association behavior, but different redox properties, controlling the working electrode potential E_{CA} in microbial electrochemical experiments allows direct command of electron transfer enhancement to charge collecting electrodes from *S. oneidensis* MR-1. The presence of 7 μM DVFBO and 7 μM F_4-DVFBO in M3Cs at a potential below their oxidation onset (E_{CA} = 200 mV) does not significantly impact biocurrent production or electrode colonization, but does increase *CE*. When the electrode potential is set to E_{CA} = 365 mV, a higher fraction of DVFBO and F_4-DVFBO species are oxidized and one observes 67 ± 12% (DVFBO) and 30 ± 5% (F_4-DVFBO) increases in steady-state current density over controls. Catalytic waves in the cyclic voltammetry measurements suggest that the COEs couple to redox species generated in metabolic pathways.

That the increases in biocurrent at E_{CA} = 365 mV correlate to increases of CV current at the oxidation potentials of DVFBO and F_4-DVFBO, together with the similar level of electrode colonization, is consistent with the two COEs acting to primarily introduce an artificial electron extraction conduit that complements naturally occurring DET and MET

pathways. Moreover, DVFBO and F_4-DVFBO allow for *tunable* increase of cell surface/electrode interfacial electron transfer and increase in transmembrane electron flux via their difference in redox properties and the poised electrode potential. This study ultimately illustrates the design of synthetic elements that enable control over electron transport from bioelectrochemical systems that are under study for applications such as bioelectrosynthesis, waste water remediation, and microbial fuel cells. The opportunity exists to further tailor the oxidation potentials of these molecules by adding additional electron donating or withdrawing groups to the core.

2.4 Materials, Methods, & Supplementary Figures

2.4.1 Materials & Methods

Unless otherwise noted, materials were purchased from suppliers (Sigma Aldrich, Acros, Strem, and TCI) and were used without further purification. ^{1}H and ^{13}C NMR spectra were recorded on either a Bruker DMX 500 MHz or Varian VNMRS 600 MHz spectrometer and all chemical shifts are reported in ppm values (δ) versus tetramethylsilane. Dry, inhibitor-free THF was taken from a solvent purification system, using packed alumina columns under Argon. Silica gel was purchased from Dynamic Adsorbents Inc. and had particle size of 32-64 μM. Compounds **2**, **3a**, and **3b** were prepared according to literature procedures.[67–69]

Comments on synthetic scheme: Due to the low solubility of intermediates **3a/3b**, it was found that 1,2-dichloroethane with 10 mol% methanol allowed the reaction with sodium borohydride to proceed smoothly in under 2 hours, while reaction in dichloromethane or under aprotic conditions returned starting material after reacting for 48 hours.

Attempts to use alcohols **4a** and **4b** as nucleophiles to synthesize ethers **5a** and **5b** failed in the presence of potassium carbonate under refluxing conditions, only returning starting materials. The inefficiency of this transformation is attributed to the decrease in acidity of alcohols **4a** and **4b** due to the electron rich nature of the cyclopentadienyl ligand located geminal to the alcohol. In order to exploit the electron rich nature of these alcohols, we reasoned that they could be electrophiles in an acid-catalyzed condensation reaction. Encouraged by reports from literature, the reaction of alcohols **4a** and **4b** with 6-bromo-1-hexanol proceeded smoothly in the presence of catalytic acetic acid, to afford both ethers in moderate yield.[70]

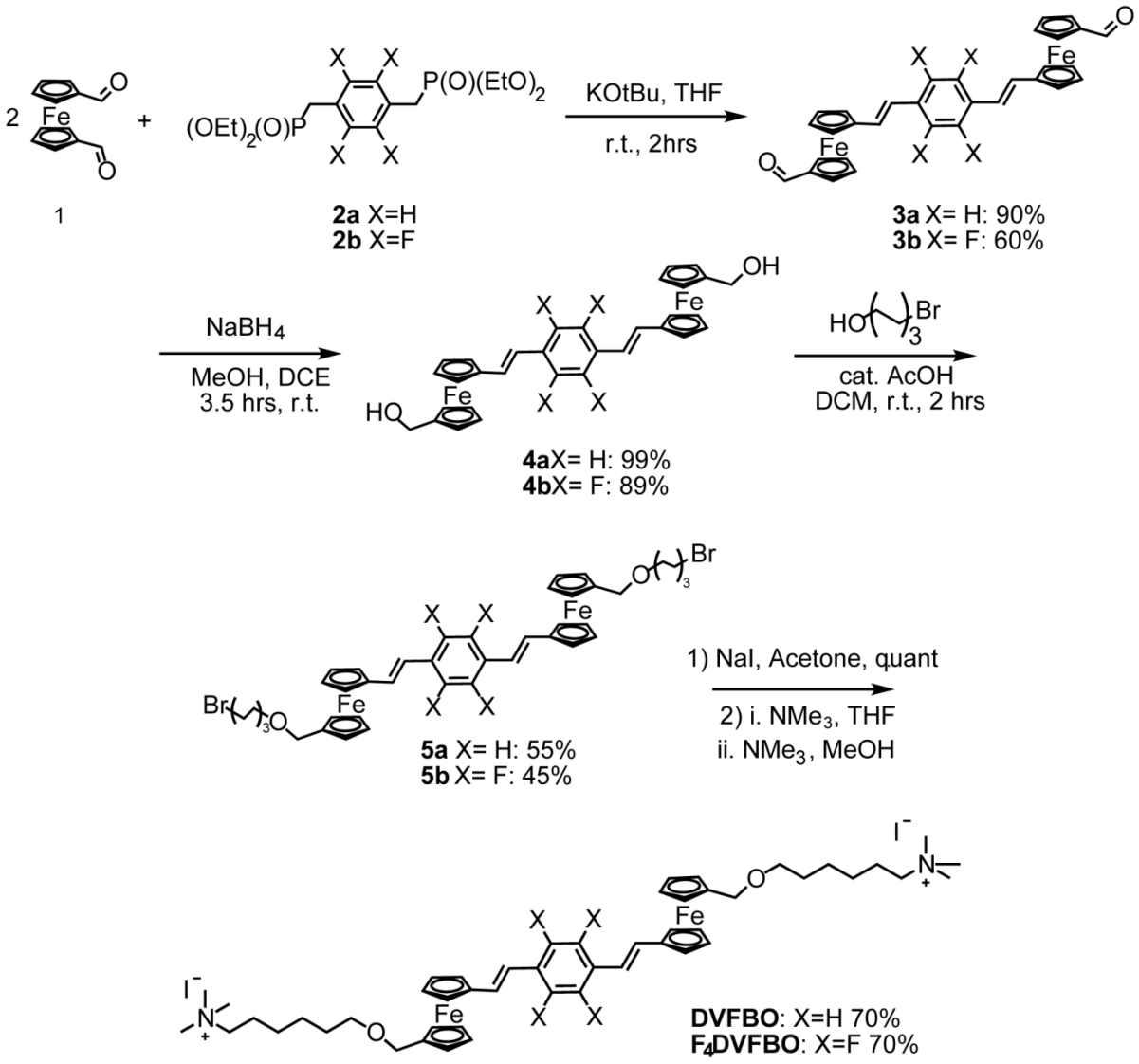

Figure 2.S1: Detailed synthetic scheme of DVFBO and F_4-DVFBO.

Preparation of 1,4-bis-(2-ethenyl-(1'-formylferrocen-1-yl))benzene (3a): A dry 100 mL schlenck flask was charged with 500 mg (1.0 eq, 1.32 mmol) of compound **2a** and 736 mg (2.3 eq, 3.04 mmol) of compound **1**. The flask was capped with a septum and placed under an inert Argon atmosphere by 3 vacuum/argon cycles. 50 mL of dry THF was added via syringe to give a deep brick red homogeneous solution. Then, 326 mg of Potassium *tert*-butoxide (2.2 eq, 2.91 mmol) was added in one portion by taking of the septum and adding the solid against an argon flow at room temperature. The solution immediately turns a bright

red and was allowed to stir under Argon for 2 hours. An aliquot of the reaction mixture shows consumption of the limiting reagent by thin layer chromatography (TLC) using 1:1 (v/v) dichloromethane (DCM) and Ethyl Acetate (EtOAc) as the mobile phase. The reaction is quenched with 10 mL of water and poured into ~100 mL of water to give a red heterogeneous mixture. The solid was collected by vacuum filtration through a Buchner filter, washed with methanol, and dried to afford **3a** of mass 656 mg in 90% yield. ^{1}H NMR (600 MHz, CD_2Cl_2) δ = 9.88 (s, 2H), 7.43 (s, 5H), 6.80 (d, J=16.2, 3H), 6.74 (d, J=16.1, 3H), 4.76 (t, J=1.9, 4H), 4.60 (t, J=1.9, 4H), 4.58 (t, J=1.9, 4H), 4.40 (t, J=1.8, 4H). ^{13}C NMR (600 MHz, $CDCl_3$) δ= 193.79, 136.36, 127.75, 126.39, 124.75, 85.46, 79.79, 74.41, 70.63, 70.50, 68.16. HRMS m/z (ESI) calcd for $C_{32}H_{26}Fe_2O_2H$ $[M+H]^+$ 553.0757, found 553.0771

*Preparation of 1,4-bis-(2-ethenyl-(1'-formylferrocen-1-yl))-2,3,5,6-tetrafluorobenzene (**3b**):* A dry 100 mL schlenck flask was charged with 500 mg (1.0 eq, 1.11 mmol) of compound **2b** and 618 mg (2.3 eq, 2.55 mmol) of compound **1**. The flask was capped with a septum and placed under an inert Argon atmosphere by 3 vacuum/argon cycles. 50 mL of dry THF was added via syringe to give a deep brick red homogeneous solution. Then, 274 mg of Potassium *tert*-butoxide (2.2 eq, 2.44 mmol) was added in one portion by removing the septum and adding the solid against an argon flow at room temperature. The solution immediately turned a bright red color and was allowed to stir under Argon for 2 hours. An aliquot of the reaction mixture shows consumption of the limiting reagent by thin layer chromatography (TLC) using 1:1 (v/v) dichloromethane (DCM) and Ethyl Acetate (EA) as the mobile phase. The reaction was quenched with 10 mL of water and poured into ~100 mL of water to give a red heterogeneous mixture. The solid was collected by vacuum filtration

through a Buchner filter, washed with methanol, and dried to afford **3b** of mass 378 mg in 54% yield. ^{1}H NMR (600 MHz, CD_2Cl_2) δ = 9.87 (s, 1H), 7.19 (d, J=16.5, 2H), 6.70 (d, J=16.6, 2H), 4.77 (s, 4H), 4.64 (s, 4H), 4.60 (s, 4H), 4.47 (s, 4H). ^{13}C NMR (600 MHz, $CDCl_3$) δ =193.30, 145.34-143.53 (dm, J= 249), 134.20 (t, J= 3.5), 114.49, 112.87, 84.31, 80.05, 74.53, 71.27, 70.77, 68.57. HRMS m/z (ESI) calcd for $C_{32}H_{22}F_4Fe_2O_2H$ $[M+H]^+$ 625.0380, found 625.0386

*Preparation of 1,4-bis-(2-ethenyl-(1'-hydroxymethylferrocen-1-yl))benzene (**4a**)***:** A 3-neck 150 mL round bottom flask was charged with 719 mg of compound **3a** (1.0 eq, 1.30 mmol), 70 mL of 1,2-dichloroethane, 7 mL of methanol (10 vol %), and placed under a blanket of Argon. 108 mg of sodium borohydride (2.2 eq, 2.85 mmol) was dissolved in a minimal amount of methanol and quickly added to the stirring, homogeneous, red solution. Bubbles of hydrogen were observed to form and continued for 3.5 hrs, at which time an aliquot analyzed by TLC showed consumption of the starting material using 20% (v/v) EA, 30% (v/v) DCM, in hexanes as the mobile phase. The reaction mixture was slowly quenched with 5 mL saturated ammonium chloride solution at room temperature. The mixture was diluted with water and extracted with DCM two times, washed with water and brine, and dried over sodium sulfate. Decanting the solution to remove the drying agent, followed by removal of solvent *in vacuo*, afforded 714 mg of compound **4a** in 99% yield. ^{1}H NMR (600 MHz, CD_2Cl_2) δ = 7.41 (s, 4H), 6.89 (d, J=16.1, 2H), 6.73 (d, J=16.1, 2H), 4.49 (t, J=1.8, 4H), 4.32 (t, J=1.8, 4H), 4.29 (s, 4H), 4.22 (t, J=1.8, 4H), 4.17 – 4.09 (m, 4H). ^{13}C NMR (600 MHz, $CDCl_3$) δ= 136.32, 126.32, 126.17, 125.90, 88.97, 83.81, 69.41, 69.39, 68.81, 67.11, 60.61. HRMS m/z (ESI) calcd for $C_{32}H_{30}Fe_2O_2$ $[M]^+$ 556.0992, found 556.0972

*Preparation of 1,4-bis-(2-ethenyl-(1'-hydroxymethylferrocen-1-yl))- 2,3,5,6-tetrafluorobenzene (**4b**):* A 3-neck 150 mL round bottom flask was charged with 513 mg of compound **3b** (1.0 eq, 0.819 mmol), 50 mL of 1,2-dichloroethane, 5 mL of methanol (10 vol %), and placed under a blanket of Argon. 68 mg of sodium borohydride (2.2 eq, 1.80 mmol) was dissolved in a minimal amount of methanol and quickly added to the stirring, homogeneous, red solution. Bubbles of hydrogen were observed to form and continued for 3.5 hrs, at which time an aliquot analyzed by TLC showed consumption of the starting material using 20% (v/v) EA, 30% (v/v) DCM, in hexanes as the mobile phase. The reaction mixture was slowly quenched with 5 mL saturated ammonium chloride solution at room temperature. The mixture was diluted with water and extracted with DCM three times, the organic layer was washed with water and brine, and dried over sodium sulfate. Decanting the solution to remove the drying agent, followed by removal of solvent *in vacuo*, afforded 714 mg of compound **4b** in 89% yield. ^{1}H NMR (600 MHz, CD_2Cl_2) δ = 7.27 (d, J=16.5, 2H), 6.68 (d, J=16.5, 2H), 4.54 (t, J=1.9, 4H), 4.40 (t, J=1.8, 4H), 4.30 (d, J=5.8, 4H), 4.24 (t, J=1.8, 4H), 4.17 (t, J=1.8, 4H). ^{13}C NMR (600 MHz, $CDCl_3$) δ= 145.29-143.45 (dm, J= 251), 135.61 (t, J= 3.3), 114.33, 111.35, 88.94, 82.84, 70.26, 69.74, 69.13, 67.61, 60.54. HRMS m/z (ESI) calcd for $C_{32}H_{26}F_4Fe_2O_2$ $[M]^+$ 628.0615, found 628.0613

*Preparation of 1,4-bis-(2-ethenyl-(1'-((6-bromohexoxy)methyl)ferrocen-1-yl))benzene (**5a**):* 300 mg of compound **4a** (1.0 eq, 0.537 mmol) was weighed into a 2 mL microwave tube and capped. 2.2 mL of DCM (~0.25M solution) was added via syringe and the flask purged with argon. Then, 3.1 μL of glacial acetic acid (10 mole %) was added *via* microsyringe and the solution was allowed to stir vigorously for 2 hours. An aliquot analyzed by TLC showed consumption of the starting material using 20% (v/v) EA, 30%

(v/v) DCM, in hexanes as the mobile phase. At this time, 0.1 mL trimethylamine was added to quench the reaction. The mixture was diluted with DCM and filtered through a silica plug. Column chromatography using a small gradient of 5 to 7% (v/v) EA in hexane was performed to remove the trimer generated in the first synthetic transformation. Removal of solvent afforded 262 mg of **5a** in 55% yield. ^{1}H NMR (600 MHz, CD_2Cl_2) δ = 7.41 (s, 4H), 6.85 (d, J=16.1, 2H), 6.69 (d, J=16.1, 2H), 4.45 (t, J=1.8, 4H), 4.30 – 4.26 (m, 4H), 4.18 (m, 8H), 4.13 (m, 4H), 3.40 (t, J=6.9, 4H), 3.35 (t, J=6.6, 4H), 1.83 (p, J=7.0, 4H), 1.50 (p, J=7.1, 4H), 1.40 (p, J=7.4, 4H), 1.35 – 1.28 (m, 4H). ^{13}C NMR (600 MHz, $CDCl_3$) δ 136.41, 126.14, 126.08, 126.06, 84.47, 84.17, 70.64, 69.79, 69.75, 69.69, 68.82, 67.30, 33.92, 32.71, 29.47, 27.94, 25.33. HRMS m/z (ESI) calcd for $C_{44}H_{52}Br_2Fe_2O_2$ $[M]^+$ 880.1082, found 880.1086

*Preparation of 1,4-bis-(2-ethenyl-(1'-((6-bromohexoxy)methyl)ferrocen-1-yl))))-2,3,5,6-tetrafluorobenzene (**5b**):* 300 mg of compound **4b** (1.0 eq, 0.537 mmol) was weighed into a 2 mL microwave tube and capped. 2.2 mL of DCM (~0.25M solution) was added via syringe and the flask purged with argon. Then, 2.7 μL of glacial acetic acid (10 mole %) was added *via* microsyringe and the solution was allowed to stir vigorously for 2 hours. An aliquot analyzed by TLC showed consumption of the starting material using 20% (v/v) EA, 30% (v/v) DCM, in hexanes as the mobile phase. At this time, 0.1 mL trimethylamine was added to quench the reaction. The mixture was diluted with DCM and filtered through a silica plug. Column chromatography using a small gradient of 5 to 7% (v/v) EA in hexane was performed to remove the trimer generated in the first synthetic transformation. Removal of solvent afforded 246 mg of **5b** in 48% yield. ^{1}H NMR (600 MHz, CD_2Cl_2) δ = 7.25 (d, J=16.5, 2H), 6.66 (d, J=16.5, 2H), 4.51 (t, J=1.9, 4H), 4.36 (t, J=1.8, 4H), 4.20 (t, J=1.9,

4H), 4.17 (s, 4H), 4.15 (t, J=1.8, 4H), 3.41 (t, J=6.9, 4H), 3.38 (t, J=6.6, 4H), 1.88 – 1.79 (m, 4H), 1.53 (m, 4H), 1.45 – 1.38 (m, 4H), 1.37 – 1.30 (m, 4H). ^{13}C NMR (600 MHz, $CDCl_3$) δ = 150.09 – 139.40 (dm, J=250), 135.84, 114.34 (d, J=11.3), 111.09, 84.65, 82.85, 70.72, 70.46, 69.87, 69.85, 68.62, 67.78, 33.87, 32.72, 29.48, 27.94, 25.34. HRMS m/z (ESI) calcd for $C_{44}H_{48}F_4Fe_2O_2Br_2$ $[M]^+$ 952.0704, found: 952.0710.

*Preparation of 1,4-bis-(2-ethenyl-(1'-((6-iodohexoxy)methyl)ferrocen-1-yl))benzene (**6a**):* 50 mg of compound **5a** (1.0 eq, 0.057 mmol), 85 mg of sodium iodide (10 eq, 0.565 mmol), and 5 mL of dry acetone were refluxed in a 10 mL round bottom flask, equipped with a stir bar and condenser, for 18 hours. Dilution of the reaction mixture with DCM and filtration through a silica plug afforded 55 mg of compound **6a** in quantitative yield. ^{1}H NMR (600 MHz, CD_2Cl_2) δ = 7.41 (s, 4H), 6.86 (d, J=16.2, 2H), 6.70 (d, J=16.1, 2H), 4.46 (s, 4H), 4.29 (s, 4H), 4.19 (d, J=7.5, 8H), 4.14 (s, 4H), 3.36 (t, J=6.6, 4H), 3.19 (t, J=7.1, 4H), 1.79 (q, J=7.1, 4H), 1.51 (p, J=6.7, 4H), 1.38 – 1.30 (m, 8H). ^{13}C NMR (600 MHz, $CDCl_3$) δ = 136.41, 126.06, 84.29, 83.80, 70.49, 69.78, 69.58, 69.53, 68.82, 67.24, 62.78, 33.42, 32.48, 30.25, 29.45, 25.13, 24.69. HRMS m/z (ESI) calcd for $C_{44}H_{52}Fe_2O_2I_2$ $[M]^+$ 976.0803, found: 976.0766.

*Preparation of 1,4-bis-(2-ethenyl-(1'-((6-iodohexoxy)methyl)ferrocen-1-yl))))- 2,3,5,6-tetrafluorobenzene (**6b**):* 50 mg of compound **5b** (1.0 eq, 0.052 mmol), 85 mg of sodium iodide (10 eq, 0.520 mmol), and 5 mL of dry acetone were refluxed in a 10 mL round bottom flask, equipped with a stir bar and condenser, for 18 hours. Dilution of the reaction mixture with DCM and filtration through a silica plug afforded 55 mg of compound **6b** in quantitative yield. ^{1}H NMR (600 MHz, CD_2Cl_2) δ = 7.26 (d, J=16.5, 2H), 6.66 (d, J=16.5, 2H), 4.54 – 4.48 (m, 4H), 4.37 (t, J=1.8, 4H), 4.21 (t, J=1.9, 4H), 4.18 (s, 4H), 4.16 (t, J=1.9,

4H), 3.38 (t, J=6.6, 4H), 3.19 (t, J=7.1, 4H), 1.80 (p, J=7.1, 4H), 1.52 (p, J=6.8, 4H), 1.41 – 1.29 (m, 8H). ^{13}C NMR (600 MHz, $CDCl_3$) δ = 145.26-143.42 (dm, J = 250), 135.87-135.82 (t, J=3.52), 114.40 (m), 111.09, 84.62, 82.80, 70.70, 70.44, 69.87, 69.83, 68.62, 67.76, 33.44, 30.25, 29.46, 25.11, 7.12. HRMS m/z (ESI) calcd for $C_{44}H_{48}F_4Fe_2O_2I_2$ $[M]^+$ 1048.0426, found: 1048.0430.

*Preparation of 1,4-bis-(2-ethenyl-(1'-((6-trimethylammoniumhexoxy)methyl)ferrocen-1-yl))benzene (**DVFBO**):* 63 mg of compound **6a** (1.0 eq, 0.064 mmol) was dissolved in 5 mL of dry, inhibitor free THF and placed under a blanket of argon. 0.4 mL of a trimethylamine solution in methanol (20 eq, 1.20 mmol, ~3.2M) was added and the solution was left to stir at room temperature for 24 hours in the dark. The resulting red heterogeneous solution was diluted with methanol to afford a homogeneous solution, another 0.4 mL portion of trimethylamine solution was added and the left to stir for another 24 hours. The excess trimethylamine and THF was removed via reduced pressure distillation to give a red oil. The oil was sonicated in the presence of hexane, centrifuged for 10 min, and the solvent decanted off. This process was repeated with a 1:1 (v/v) mixture of inhibitor free diethyl ether and pure diethyl ether to give 50 mg of a red solid in 70% yield. ^{1}H NMR (600 MHz, CD_3OD) δ = 7.46 (s, 4H), 6.92 (d, *J*=16.2, 2H), 6.76 (d, *J*=16.2, 2H), 4.54 – 4.47 (m, 4H), 4.32 – 4.26 (m, 4H), 4.24 – 4.17 (m, 8H), 4.16 – 4.11 (m, 4H), 3.36 (t, *J*=6.6, 4H), 3.27 – 3.21 (m, 4H), 3.05 (s, 18H), 1.72 – 1.62 (m, 4H), 1.47 (m, 4H), 1.29 (m8H). ^{13}C NMR (600 MHz, CD_3OD) δ = 136.52, 125.90, 125.84, 125.81, 83.87, 83.69, 70.36, 69.51, 69.33, 69.18, 68.76, 67.07, 66.42, 52.30 (t, J= 3.7), 28.79, 25.57, 25.28, 22.44. HRMS m/z (ESI) calcd for $C_{50}H_{70}Fe_2N_2O_2I$ $[M-I]^+$ 967.3228, found: 967.3276

*Preparation of 1,4-bis-(2-ethenyl-(1'-((6-trimethylammoniumhexoxy)methyl)ferrocen-1-yl))))- 2,3,5,6-tetrafluorobenzene diiodide (**F_4-DVFBO**):* 63 mg of compound **6b** (1.0 eq, 0.064 mmol) was dissolved in 5 mL of dry, inhibitor free THF and placed under a blanket of argon. 0.4 mL of a trimethylamine solution in methanol (20 eq, 1.20 mmol, ~3.2M) was added and the solution was left to stir at room temperature for 24 hours in the dark. The resulting red heterogeneous solution was diluted with methanol to afford a homogeneous solution, another 0.4 mL portion of trimethylamine solution was added and the left to stir for another 24 hours. The excess trimethylamine and THF was removed via reduced pressure distillation to give a red oil. The oil was sonicated in the presence of hexane, centrifuged for 10 min, and the solvent decanted off. This process was repeated with a 1:1 (v/v) mixture of inhibitor free diethyl ether and pure diethyl ether to give 49 mg of a red solid in 70% yield. ^{1}H NMR (600 MHz, CD_3OD:D_2O) δ = 7.24 (d, J=16.5, 2H), 6.66 (d, J=16.4, 2H), 4.56 (t, J=2.0, 4H), 4.40 (t, J=2.0, 4H), 4.31 – 4.19 (m, 8H), 4.19 – 4.16 (m, 4H), 3.41 (t, J=6.5, 4H), 3.33 – 3.29 (m, 4H), 3.10 (s, 18H), 1.74 (m, 4H), 1.54 (m, 4H), 1.43 – 1.31 (m, 8H). ^{1}H NMR (600 MHz, CD_3OD) δ = 144.24 (dm, J= 247), 136.42, 114.37, 110.13, 84.09, 82.52, 70.56, 70.40, 69.57, 69.48, 68.51, 67.62, 66.40, 52.26 (t, J=3.9), 28.90, 25.60, 25.32, 22.43. HRMS m/z (ESI) calcd for 3276 $C_{50}H_{66}F_4Fe_2N_2O_2I$ $[M\text{-}I]^+$ 1039.2852, found: 1039.2863

Ultraviolet-Visible Absorbance Spectroscopy: Solutions were illuminated at 1 nm wavelength intervals at a scan rate of 20 nm/s (Beckman Coulter DU 800 Spectrophotometer) in a quartz cuvette with 1 cm path length.

Differential Pulse Voltammetry: DPV traces were collected using a glassy carbon electrode, $Ag/AgNO_3$ (0.01 M MeCN) or Ag/AgCl (saturated KCl) reference electrode, and platinum counter electrode. Measurements taken in chloroform with $Ag/AgNO_3$ were

converted to Ag/AgCl using 0.3 V $Ag/AgNO_3$ = 0 V vs SCE.[38] The working electrode was cleaned and polished before each scan with successive rubbing with a paste of 0.3 μm Alumina particles in water on a polishing cloth, a 0.05 μm Alumina paste on a polishing cloth, washing with water then acetone, and allowed to air dry. The parameters for DPV scans were as follows: the scan window (low E to high E) was chosen as needed and the following parameters were kept invariant, Incr E (V) = 0.002, Amplitude (V) = 0.05, Pulse Width (sec) = 0.2, Sample Width (sec) = 0.02, Pulse Period (sec) = 0.4. For DPV redox peaks, the potentials at which peak current occurs, E_{max}, are shifted from the actual redox potentials of the redox species, $E_{1/2}$, by a value of one half the pulse amplitude, $\Delta E/2$ = 25 mV. This can be corrected using the expression: $E_{1/2} = E_{max} + \Delta E/2$.[37] Chloroform solutions utilized 100 mM tetrabutylammonium hexafluorophosphate (Sigma Aldrich) and aqueous solutions used 100 mM pH 7.2 phosphate buffer (PB) as the supporting electrolyte.

Zeta Potential Measurements: Zeta potentials were measured using a Malvern Zetasizer Nano ZS equipped with a He-Ne 4mW 633 nm laser.

*Cell culture, inoculation, and growth medium***:** *Shewanella oneidensis* MR-1 was struck out on LB agar plates from frozen bacterial stock and incubated at 30 °C to isolate single colonies. Liquid cultures were grown by selecting morphologically similar colonies with a sterile loop to inoculate anaerobic modified M1 medium[6] containing 20 mM Na-(L)-lactate as electron donor and 20 mM Na-fumarate as electron acceptor. After 24 hours of incubation with shaking at 30 °C and 120 rpm, cultures consistently reach a maximum OD_{600} of ~0.20 (or 2.0×10^8 cfu/mL). These stationary phase cultures are then centrifuged and washed 2 times. The final concentration of the liquid culture inoculated into M3Cs was 0.15 OD_{600}.

Microbial Three-Electrode Electrochemical Cells (M3Cs): The 3-electrode, batch-type, membraneless bioelectrochemical reactors used herein (M3Cs) follow the Bond design.[9] Glass M3C vials have a 20 mL working volume and are sealed with gaskets. Reference electrode: Ag/AgCl (saturated KCl) with 3.2 mm Vycor frit (Gamry). Counter electrode: coiled 0.25 mm Ti wire (Aldrich), 10 turns. Working electrode: 1 cm × 1 cm × 0.2 cm carbon felt (Alfa Aesar), woven with Ti wire as the electrical lead. Anaerobic conditions were maintained through constant headspace degassing with humidified, deoxygenated N_2. Temperature was kept at 30 °C by housing the M3Cs in a temperature regulated incubator. COEs were added to M3Cs at 7 μM end concentration (previously optimized) by first making concentrated aqueous solutions (200–2000 μM) and then adding the necessary negligible volume of these solutions to achieve the correct COE concentration.

Chronoamperometry (CA): Using a Gamry potentiostat (Reference 600) and multiplexer (model ECM8), M3C carbon felt working electrodes were poised at E_{CA} = 200 mV or 365 mV vs Ag/AgCl to serve as the sole terminal electron acceptor for bacteria. M3Cs were inoculated from stationary liquid cultures (see above) with 20 mM Na-(L)-lactate and incubated in the dark[7] with 150 rpm magnetic stirring for 40 hours total to cultivate an electroactive biofilm and measure current responses. The current response was measured, recorded, and averaged for 20-second blocks (at 160 second intervals) with Gamry software (Framework Version 6.11, Build 2227, 2013). Time integration of the resulting current response determined the amount of charge transferred by the bacteria, Q_{col} (Table 2.S1).

Cyclic voltammetry (CV): Electrochemical characterization with CV was undertaken with a Gamry potentiostat (Reference 600) and multiplexer (model ECM8) at the indicated time points to characterize the COE-bacteria-electrode interactions. For these experiments,

the working electrode potential was swept from $E_{initial}$ = –0.6 V to E_{vertex} = 0.45 V and back to E_{final} = –0.6 V at a scan rate of 0.005 V/s. For CV at time point II, CA was stopped and these CA traces are not shown.

High performance liquid chromatography (HPLC): HPLC analysis of M3C effluent was performed with a Shimadzu LC20AB instrument equipped with an organic acid compatible C18 Kinetix column (Phenomenex). Samples from M3Cs were filtered through 0.22 µm PES filters (Thermo Fisher) to remove cells, and diluted 10-fold into mobile phase prior to analysis. The mobile phase was 20 mM Potassium Phosphate (pH = 2.0) flowing at 1.25 mL min^{-1}, and UV detection was set at 210 nm.

Scanning Electron Microscopy (SEM): Images of chemically fixed carbon felt electrodes were obtained with an FEI XL40 SEM at an accelerating voltage of 5 kV, working distance of ~5 mm, and a spot size of 3. Post processing of images only involved increasing the brightness and/or contrast of the images by up to 40% in order to better visualize cells.

Chemical fixation of cells: After bioelectrochemical experiments, M3C working electrodes were submerged in 100 mM PBS, pH = 7 containing 2% (v/v) formaldehyde to fix electrode-associated cells for 24 hours. After fixation, electrodes were sequentially rinsed with the following solutions twice each: 100 mM PBS, pH = 7 (10 min), deionized water (10 min), 70% ethanol in deionized water (10 min), 100% ethanol (30 min). Electrodes were then allowed to air dry for 24 hours and stored in glass scintillation vials for future study.

Biomass Quantification: Electrodes were gently rinsed with 100 mM PBS to remove planktonic cells and then placed in test tubes with 2 mL of 0.2 M NaOH and kept at 4 ˚C for 1 hour.[71] Samples were vortexed for 10 seconds every 15 minutes. Electrodes were then rinsed with 2 mL of Millipore water. To lyse the cells, samples were frozen at -20 ˚C then

thawed at 90 ˚C for 10 minutes, repeated 3 times. 96 well plates were used to test the samples with the Coomassie Plus Reagent against bovine serum albumin standards made with 0.1 M NaOH diluent.

Abbreviations: COE, conjugated oligoelectrolyte; BES, bioelectrochemical system; EET, extracellular electron transfer; CV, cyclic voltammetry; M3C, microbial three-electrode electrochemical cell; λ_{max}, absorbance maximum; MLCT, metal to ligand charge transfer; DPV, differential pulse voltammetry; PB, phosphate buffer; ZP, zeta potential; cryo-TEM, cryogenic transmission electron microscopy; MIC, minimum inhibitory concentration; CA, chronoamperometry; E_{CA}, electrode poised potential during CA; E°_{ox}, oxidation potential; J, current density; J_{SS}, steady-state biocurrent density at t = 39 hours; E_{CV}, electrode potential during CV; MET, mediated electron transfer through flavins; DET, direct electron transfer through membrane proteins; dJ/dE, first derivative of current density with respect to potential; J_{P}, peak current density from CV trace; $Q_{\mathrm{col,}}$ charge collected during CA; Q_{lac}, charge equivalents of lactate; CE, coulombic efficiency.

2.4.2 Supplementary Figures & Discussion

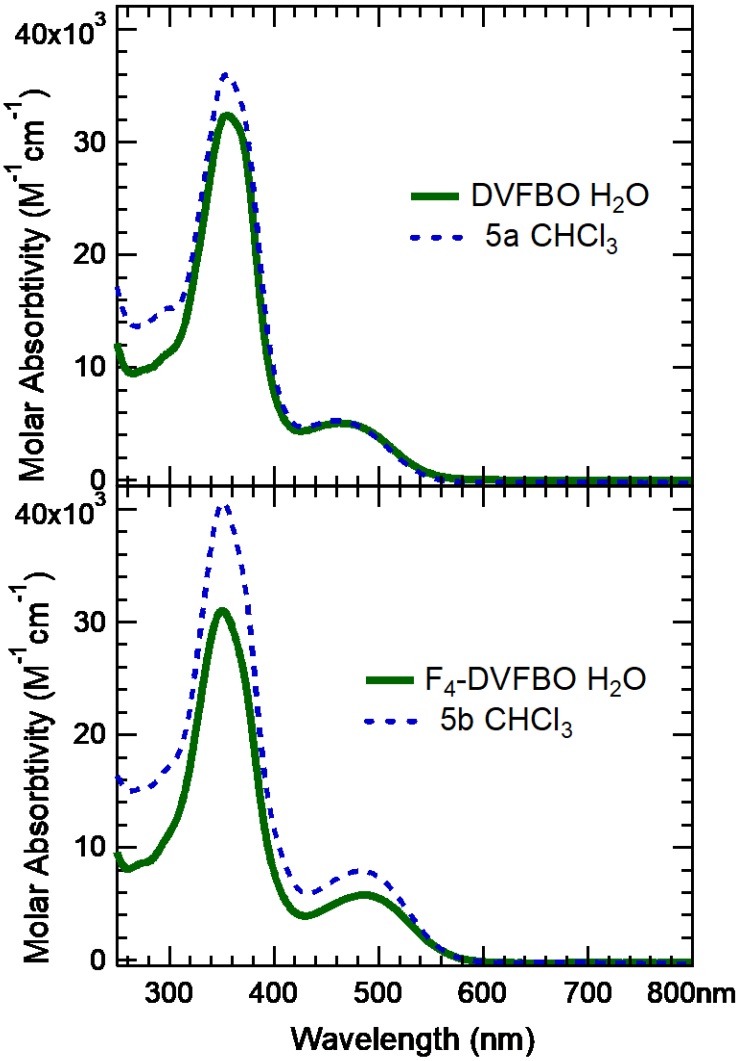

Figure 2.S2: UV-Vis Spectra of 5a, 5b, DVFBO and F4-DVFBO.

At 10 μM (Figure 2.S3b), the second oxidation step centered at 580 mV, containing a shoulder at 522 mV, is observed in the DVFBO trace. Further increasing the concentration to 50 μM (Figure 2.S3c) results in the appearance of a third feature at 682 mV of even larger magnitude. At 100 μM (Figure 2.S3d), the middle feature shifts from 522 mV to 583 mV, while maintaining the higher potential, largest magnitude signal at 698 mV. Similar trends are observed for F_4-DVFBO (Figure 2.S3e-h). The concentration dependence of these

oxidation signals suggests supramolecular aggregation. Moreover, that the oxidation signal centered between 522-582 mV is observed to shift between 10-100 μM suggests that this feature originates from a supramolecular entity whose structure is dynamic with respect to concentration.

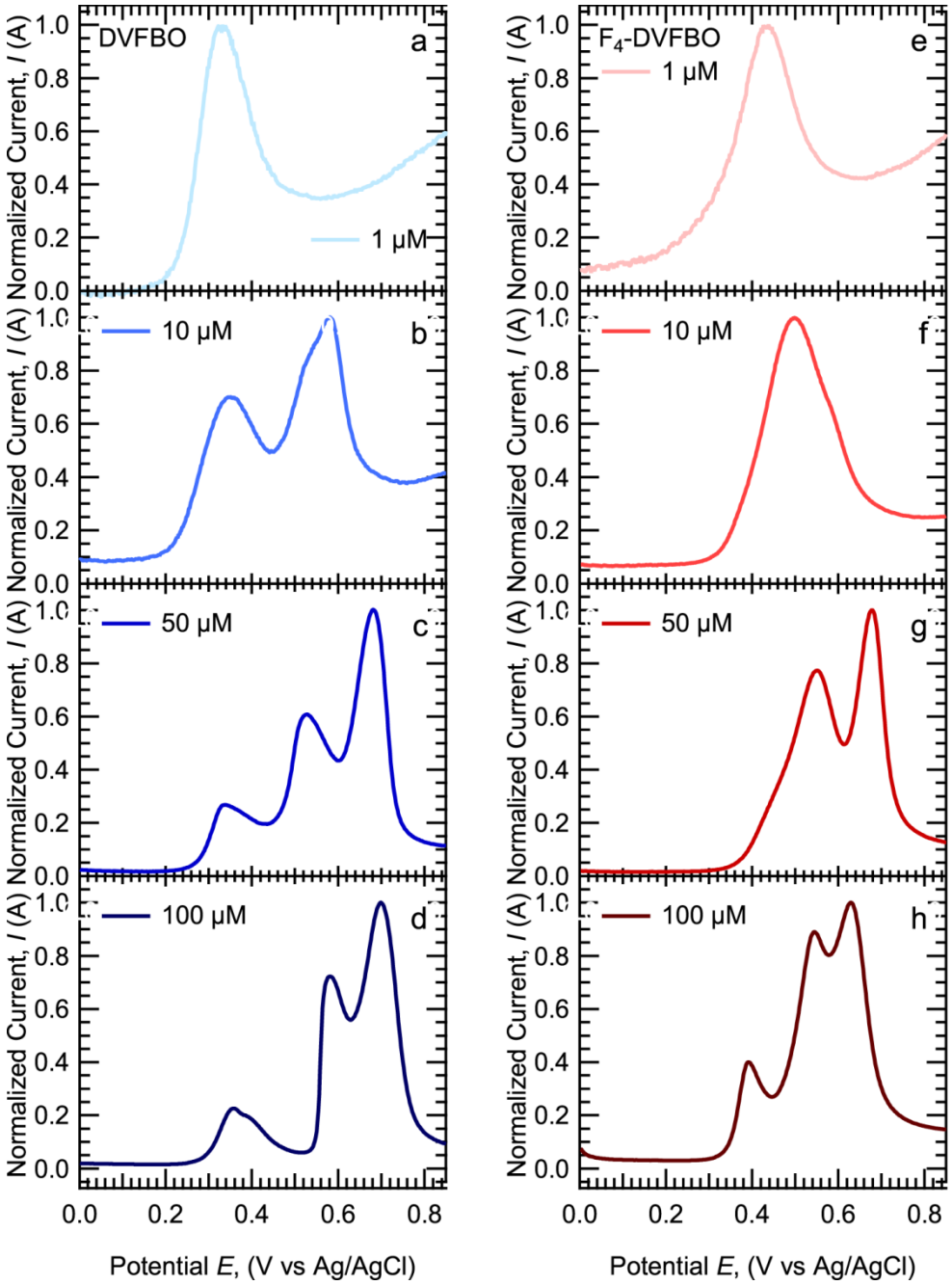

Figure 2.S3: DPV traces of DVFBO (a-b) and F4-DVFBO (e-h) in PB at 25 ˚C. (a) 1 μM DVFBO, (b) 10 μM DVFBO, (c) 50 μM DVFBO, (d) 100 μM DVFBO, (e) 1 μM F_4-DVFBO, (f) 10 μM F_4-DVFBO, (g) 50 μM F_4-DVFBO, and (h) 100 μM F_4-DVFBO 50 μM DVFBO. All traces are normalized relative to the highest intensity feature.

When the DPV traces of DVFBO (50 μM) were taken as a function of temperature, the feature centered at 334 mV shifted to lower potentials as expected and, more importantly, the two features centered at 526 mV and 682 mV coalesce upon one another to 568 mV at 70°C (**Figure 2.S4**), again consistent with supramolecular organization.[72,73]

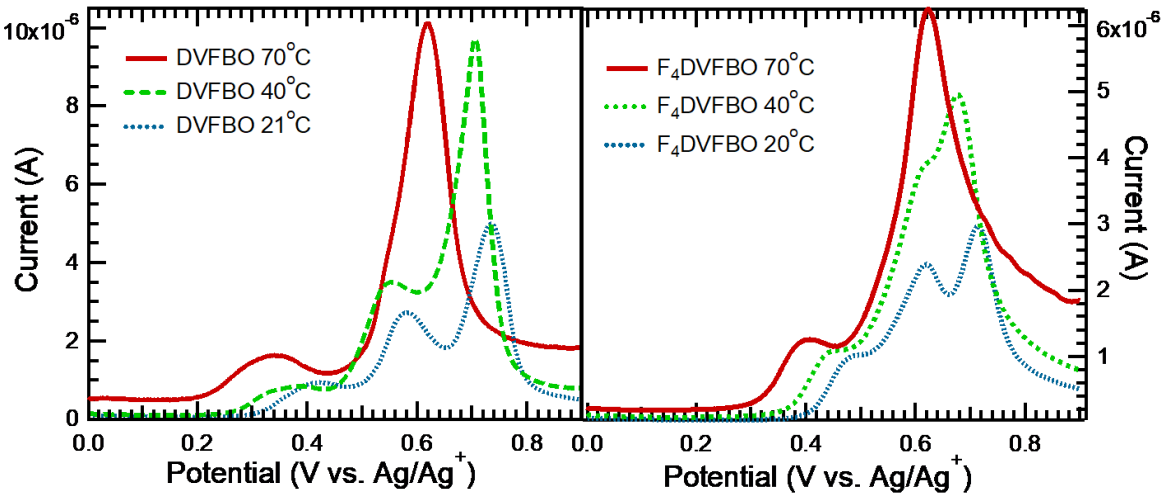

Figure 2.S4: Temperature dependent DPV scans of DVFBO and F_4-DVFBO in PB at 50 μM.

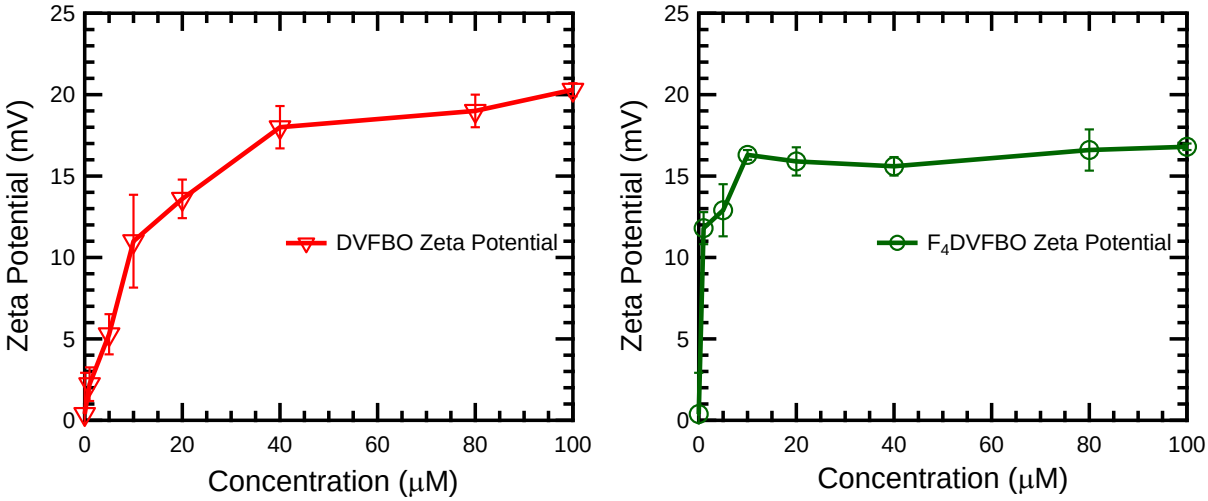

Figure 2.S5: Zeta potential measurements of DVFBO and F_4-DVFBO in 100 mM PB as a function of concentration.

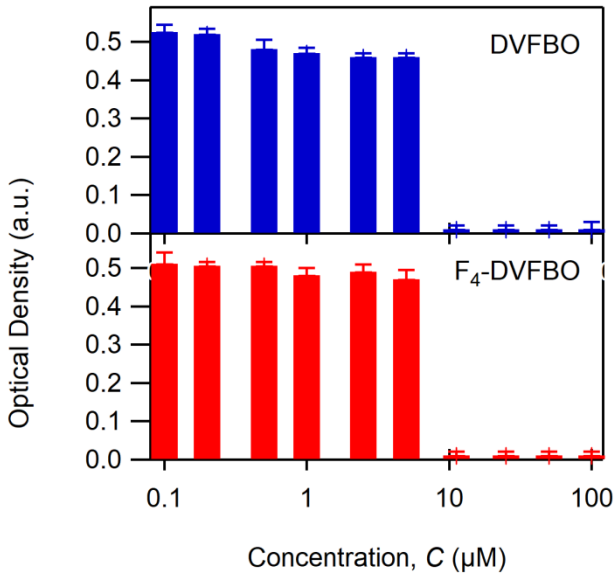

Figure 2.S6: Determination of the minimum inhibitory concentration (MIC) of DVFBO and F_4-DVFBO for *S. oneidensis* MR-1. Triplicate average cell culture optical density at t = 72 h was measured at 600 nm as a function of logarithmic DVFBO and F_4-DVFBO concentrations. The MIC is read as the lowest concentration that completely inhibits growth[47] of the target organism, here detected as 11.25 μM for both COEs.

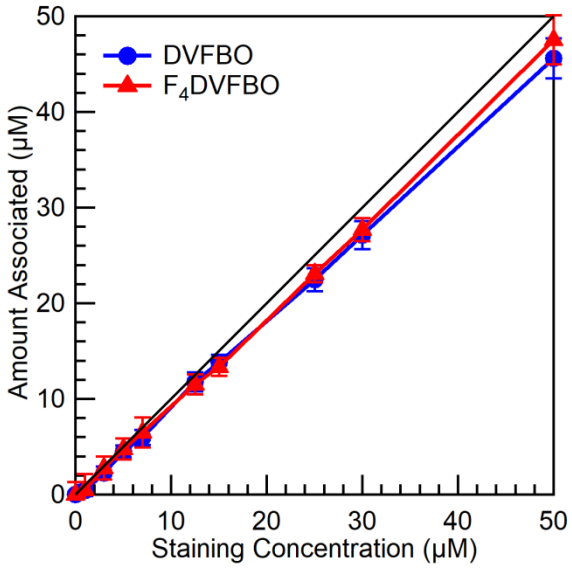

Figure 2.S7: Association of DVFBO and F_4-DVFBO with cells of *S. oneidensis* MR-1. Data points falling on the solid black line indicate 100% association of the COEs with cells for a given staining concentration. Concentrations were measured by taking the absorbance spectra of growth medium (water) solutions containing varying concentrations of COEs, re-suspending the bacteria for 1 h at constant OD = 0.40 in these solutions to enable association, centrifugation, and re-measuring the absorbance spectra of the supernatant to calculate the difference in concentration.

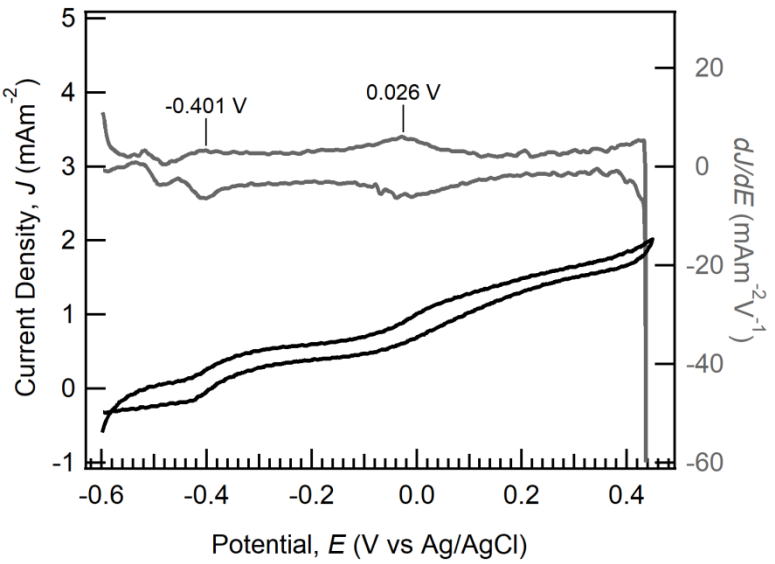

Figure 2.S8: Average CV and *dJ/dE* outputs from *S. oneidensis* MR-1. Experiments were conducted at time point I indicated in CA plots, i.e. for before chronoamperometry, just after inoculating M3Cs with bacteria.

Table 2.S1: Measured and calculated bioelectrochemical parameters from M3Cs employing DVFBO and F4DVFBO.[a]

		CA @ E = 200 mV vs Ag/AgCl			CA @ E = 365 mV vs Ag/AgCl		
Measured Parameter	Expression	Control	7µM DVFBO	7 µM F4DVFBO	Control	7µM DVFBO	7 µM F_4DVFBO
Charge collected (C)	$Q_{\mathrm{col}} = A\int J(t)dt$	13.4 ± 2.5	12.5 ± 2.6	12.0 ± 0.4	22.4 ± 1.4	33.5 ± 2.0	29.9 ± 4.0
Lactate consumed[b] (mM)	$\Delta[\mathrm{lac}] = [\mathrm{lac}]_{\mathrm{f}} - [\mathrm{lac}]_{\mathrm{i}}$	-5.2 ± 1.1	-1.9 ± 0.4	-3.5 ± 0.1	-3.6 ± 0.5	-5.0 ± 1.4	-6.0 ± 1.0
Lactate charge equivalent[c] (C)	$Q_{\mathrm{lac}} = -\Delta[\mathrm{lac}]VF$	29.3 ± 8.3	14.1 ± 2.8	26.6 ± 0.7	27.2 ± 4.0	37.6 ± 10.6	45.3 ± 7.8
Coulombic efficiency (%)	$CE_{\mathrm{lac}} = 100 \times Q_{\mathrm{col}}/Q_{\mathrm{lac}}$	34 ± 3	89 ± 23	45 ± 1	82 ± 11	89 ± 23	66 ± 10
Biomass concentration (µg mL^{-1})	[protein]	19 ± 2	21 ± 2	22 ± 4	28 ± 6	33 ± 4	23 ± 4

[a] Measured values are averages from the replicate M3Cs as discussed in the text and figures, while calculated parameters follow the provided expressions; quoted uncertainties represent ± 1 standard deviation (for measured values) or are propagated errors by addition of standard deviations in quadrature (for calculated values).[b] Note that $\Delta[lac] < 0$ because lactate consumption produces electrons in Equation 1; this is why the expression for Q_{lac} contains a negative sign. [c] V = 19.5 mL (0.5 mL from 20 mL is used for HPLC); $F = eN_A \approx$ 96485 C mol^{-1}, where $e = 1.602 \times 10^{-19}$ C and $N_A = 6.02 \times 10^{23}$ mol^{-1}; n = 4 from Equation 1.

2.5 Acknowledgements

We gratefully acknowledge support by the Institute for Collaborative Biotechnologies (ICB) under grant W911F-09-D-0001 from the U.S. Army Research Office. S. R. M is grateful for funding from the National Science Foundation Graduate Research Fellowships Program (NSF GRFP) under grant 1650114. Spectroscopy and electron microscopy research reported here made use of shared facilities of the UCSB MRSEC (NSF DMR 1720256), a member of the Materials Research Facilities Network (www.mrfn.org). The authors acknowledge the use of the Biological Nanostructures Laboratory within the California NanoSystems Institute, supported by the University of California, Santa Barbara and the University of California, Office of the President. S. R. M. acknowledges Dr. Zach Rengert for the design and synthesis of DVFBO and F_4-DVFBO, as well as Dr. Mengwen Zhang for cryo-TEM imaging.

2.6 References

(1) Logan, B. E. Exoelectrogenic Bacteria That Power Microbial Fuel Cells. *Nat. Rev. Microbiol.* **2009**, *7* (5), 375–381. https://doi.org/10.1038/nrmicro2113.

(2) Logan, B. E.; Rabaey, K. Conversion of Wastes into Bioelectricity and Chemicals by Using Microbial Electrochemical Technologies. *Science (80-.).* **2012**, *337* (6095), 686–690. https://doi.org/10.1126/science.1217412.

(3) Lovley, D. R. Live Wires: Direct Extracellular Electron Exchange for Bioenergy and the Bioremediation of Energy-Related Contamination. *Energy Environ. Sci.* **2011**, *4* (12), 4896. https://doi.org/10.1039/c1ee02229f.

(4) Lovley, D. R. Electromicrobiology. *Annu. Rev. Microbiol.* **2012**, *66* (1), 391–409. https://doi.org/10.1146/annurev-micro-092611-150104.

(5) Renslow, R.; Babauta, J.; Kuprat, A.; Schenk, J.; Ivory, C.; Fredrickson, J.; Beyenal, H. Modeling Biofilms with Dual Extracellular Electron Transfer Mechanisms. *Phys. Chem. Chem. Phys.* **2013**, *15* (44), 19262–19283. https://doi.org/10.1039/c3cp53759e.

(6) Babanova, S.; Bretschger, O.; Roy, J.; Cheung, A.; Artyushkova, K.; Atanassov, P. Innovative Statistical Interpretation of Shewanella Oneidensis Microbial Fuel Cells Data. *Phys. Chem. Chem. Phys.* **2014**, *16* (19), 8956–8969. https://doi.org/10.1039/c4cp00566j.

(7) Babanova, S.; Cornejo, J.; Roy, J. N.; Babanova, S.; Garcia, K. E.; Cornejo, J.; Ista, L. K.; Atanassov, P. Catalytic Biofilm Formation by Shewanella Oneidensis MR-1 and Anode Characterization by Expanded Uncertainty. *Electrochim. Acta* **2017**, *126* (July 2013), 3–10. https://doi.org/10.1016/j.electacta.2013.07.075.

(8) Kirchhofer, N. D.; Chen, X.; Marsili, E.; Sumner, J. J.; Dahlquist, F. W.; Bazan, G. C. The Conjugated Oligoelectrolyte DSSN+ Enables Exceptional Coulombic Efficiency via Direct Electron Transfer for Anode-Respiring Shewanella Oneidensis MR-1-a Mechanistic Study. *Phys. Chem. Chem. Phys.* **2014**, *16* (38), 20436–20443. https://doi.org/10.1039/c4cp03197k.

(9) Marsili, E.; Rollefson, J. B.; Baron, D. B.; Hozalski, R. M.; Bond, D. R. Microbial Biofilm Voltammetry: Direct Electrochemical Characterization of Catalytic Electrode-Attached Biofilms. *Appl. Environ. Microbiol.* **2008**, *74* (23), 7329–7337. https://doi.org/10.1128/AEM.00177-08.

(10) Jain, A.; Zhang, X.; Pastorella, G.; Connolly, J. O.; Barry, N.; Woolley, R.; Krishnamurthy, S.; Marsili, E. Electron Transfer Mechanism in Shewanella Loihica PV-4 Biofilms Formed at Graphite Electrode. *Bioelectrochemistry* **2012**, *87*, 28–32. https://doi.org/10.1016/j.bioelechem.2011.12.012.

(11) Rosenbaum, M.; Angenent, L. T. Genetically Modified Microorganisms for Bioelectrochemical Systems. In *Bioelectrochemical Systems: from extracellular electron transfer to biotechnological application*; Rabaey, K., Angenent, L., Schroder, U., Keller, J., Eds.; IWA Publishing, 2009; pp 101–113.

(12) Du, J.; Catania, C.; Bazan, G. C. Modification of Abiotic-Biotic Interfaces with Small Molecules and Nanomaterials for Improved Bioelectronics. *Chem. Mater.* **2014**, *26* (1), 686–697. https://doi.org/10.1021/cm401912j.

(13) Xie, X.; Criddle, C.; Cui, Y. Design and Fabrication of Bioelectrodes for Microbial Bioelectrochemical Systems. *Energy Environ. Sci.* **2015**, *8* (12), 3418–3441. https://doi.org/10.1039/C5EE01862E.

(14) TerAvest, M. A.; Ajo-Franklin, C. M. Transforming Exoelectrogens for Biotechnology Using Synthetic Biology. *Biotechnol. Bioeng.* **2016**, *113* (4), 687–697. https://doi.org/10.1002/bit.25723.

(15) Patil, S. a; Hasan, K.; Leech, D.; Hägerhäll, C.; Gorton, L. Improved Microbial Electrocatalysis with Osmium Polymer Modified Electrodes. *Chem. Commun.* **2012**, *48* (82), 10183. https://doi.org/10.1039/c2cc34903e.

(16) Förster, A. H.; Beblawy, S.; Golitsch, F.; Gescher, J. Electrode-Assisted Acetoin Production in a Metabolically Engineered Escherichia Coli Strain. *Biotechnol. Biofuels* **2017**, *10* (1), 65. https://doi.org/10.1186/s13068-017-0745-9.

(17) Elie, C.-R.; Hébert, A.; Charbonneau, M.; Haiun, A.; Schmitzer, A. R. Benzimidazolium-Based Synthetic Chloride and Calcium Transporters in Bacterial Membranes. *Org. Biomol. Chem.* **2013**, *11* (6), 923–928. https://doi.org/10.1039/C2OB26966J.

(18) Fyles, T. M. Synthetic Ion Channels in Bilayer Membranes. *Chem. Soc. Rev.* **2007**, *36* (2), 335–347. https://doi.org/10.1039/B603256G.

(19) Nango, M.; Hikita, T.; Nakano, T.; Yamada, T.; Nagata, M.; Kurono, Y.; Ohtsuka, T. Manganese Porphyrin-Mediated Electron Transfer across a Liposomal Membrane and on an Electrode Modified with a Lipid Bilayer Membrane. *Langmuir* **1998**, *14* (2), 407–416. https://doi.org/10.1021/la970463r.

(20) Patil, A. O.; Ikenoue, Y.; Wudl, F.; Heeger, A. J. Water Soluble Conducting Polymers. *J. Am. Chem. Soc.* **1987**, *109* (6), 1858–1859. https://doi.org/10.1021/ja00240a044.

(21) Sundaresan, N. S.; Basak, S.; Pomerantz, M.; Reynolds, J. R. Electroactive Copolymers of Pyrrole Containing Covalently Bound Dopant Ions: Poly{pyrrole-Co-[3-(Pyrrol-1-Yl)Propanesulphonate]}. *J. Chem. Soc. Chem. Commun.* **1987**, No. 8, 621–622. https://doi.org/10.1039/C39870000621.

(22) *Conjugated Polyelectrolytes: Fundamentals and Applications*; Liu, B., Bazan, G. C., Eds.; John Wiley & Sons, 2013.

(23) Wang, Y.; Schanze, K. S.; Chi, E. Y.; Whitten, D. G. When Worlds Collide: Interactions at the Interface between Biological Systems and Synthetic Cationic Conjugated Polyelectrolytes and Oligomers. *Langmuir* **2013**, *29* (34), 10635–10647. https://doi.org/10.1021/la4012263.

(24) Duarte, A.; Pu, K.-Y.; Liu, B.; Bazan, G. C. Recent Advances in Conjugated Polyelectrolytes for Emerging Optoelectronic Applications. *Chem. Mater.* **2011**, *23* (3), 501–515. https://doi.org/10.1021/cm102196t.

(25) Thomas, S. W.; Joly, G. D.; Swager, T. M. Chemical Sensors Based on Amplifying Fluorescent Conjugated Polymers. *Chem. Rev.* **2007**, *107* (4), 1339–1386. https://doi.org/10.1021/cr0501339.

(26) Li, C.; Numata, M.; Takeuchi, M.; Shinkai, S. A Sensitive Colorimetric and Fluorescent Probe Based on a Polythiophene Derivative for the Detection of ATP. *Angew. Chemie Int. Ed.* **2005**, *44* (39), 6371–6374. https://doi.org/10.1002/anie.200501823.

(27) DiCesare, N.; Pinto, M. R.; Schanze, K. S.; Lakowicz, J. R. Saccharide Detection Based on the Amplified Fluorescence Quenching of a Water-Soluble Poly(Phenylene Ethynylene) by a Boronic Acid Functionalized Benzyl Viologen Derivative. *Langmuir* **2002**, *18* (21), 7785–7787. https://doi.org/10.1021/la0264926.

(28) Rininsland, F.; Xia, W.; Wittenburg, S.; Shi, X.; Stankewicz, C.; Achyuthan, K.; McBranch, D.; Whitten, D. Metal Ion-Mediated Polymer Superquenching for Highly Sensitive Detection of Kinase and Phosphatase Activities. *Proc. Natl. Acad. Sci. U. S. A.* **2004**, *101* (43), 15295–15300. https://doi.org/10.1073/pnas.0406832101.

(29) Wang, Y.; Zhang, Y.; Liu, B. Conjugated Polyelectrolyte Based Fluorescence Turn-On Assay for Real-Time Monitoring of Protease Activity. *Anal. Chem.* **2010**, *82* (20), 8604–8610. https://doi.org/10.1021/ac101695x.

(30) Ortony, J. H.; Chatterjee, T.; Garner, L. E.; Chworos, A.; Mikhailovsky, A.; Kramer, E. J.; Bazan, G. C. Self-Assembly of an Optically Active Conjugated Oligoelectrolyte. *J. Am. Chem. Soc.* **2011**, *133* (21), 8380–8387. https://doi.org/10.1021/ja202776b.

(31) Catania, C.; Ajo-franklin, C. M.; Bazan, G. C. Membrane Permeabilization by Conjugated Oligoelectrolytes Accelerates Whole-Cell Catalysis. *RSC Adv.* **2016**, *6*, 100300–100306. https://doi.org/10.1039/C6RA23083K.

(32) Kirchhofer, N. D.; Rengert, Z. D.; Dahlquist, F. W.; Nguyen, T.-Q.; Bazan, G. C. A Ferrocene-Based Conjugated Oligoelectrolyte Catalyzes Bacterial Electrode Respiration. *Chem* **2017**, *2* (2), 240–257. https://doi.org/10.1016/j.chempr.2017.01.001.

(33) Weaver, J. C.; Schoenbach, K. H. Biodielectrics. *IEEE Trans. Dielectr. Electr. Insul.* **2011**, *18* (2), c1–c1. https://doi.org/10.1109/TDEI.2011.5739436.

(34) Woo, H. Y.; Liu, B.; Kohler, B.; Korystov, D.; Mikhailovsky, A.; Bazan, G. C. Solvent Effects on the Two-Photon Absorption of Distyrylbenzene Chromophores. *J. Am. Chem. Soc.* **2005**, *127* (42), 14721–14729. https://doi.org/10.1021/ja052906g.

(35) Salzner, U. Quantitatively Correct UV-Vis Spectrum of Ferrocene with TDB3LYP. *J. Chem. Theory Comput.* **2013**, *9* (9), 4064–4073. https://doi.org/10.1021/ct400322v.

(36) Barlow, S.; Bunting, H. E.; Ringham, C.; Green, J. C.; Bublitz, G. U.; Boxer, S. G.; Perry, J. W.; Marder, S. R. Studies of the Electronic Structure of Metallocene-Based Second-Order Nonlinear Optical Dyes. *J. Am. Chem. Soc.* **1999**, *121* (15), 3715–3723. https://doi.org/10.1021/ja9830896.

(37) Bard, A. J.; Faulkner, L. R. *Electrochemical Methods: Fundamentals and Applications*, 2nd ed.; John Wiley & Sons, Inc, 2001.

(38) Meites, L. *Handbook of Analytical Chemistry*, First Edit.; McGraw-Hill Inc.,US: New

York, 1963.

(39) N.P.R.A. Silva, M. E.; Pombeiro, A. J. L.; Fraústo da Silva, J. J. R.; Herrmann, R.; Deus, N.; E.Bozak, R. Redox Potential and Substituent Effects in Ferrocene Derivatives: II. *J. Organomet. Chem.* **1994**, *480* (1–2), 81–90. https://doi.org/10.1016/0022-328X(94)87105-1.

(40) White, B.; Banerjee, S.; O'Brien, S.; Turro, N. J.; Herman, I. P. Zeta-Potential Measurements of Surfactant-Wrapped Individual Single-Walled Carbon Nanotubes. *J. Phys. Chem. C* **2007**, *111* (37), 13684–13690. https://doi.org/10.1021/jp070853e.

(41) Qiu, L. Y.; Bae, Y. H. Self-Assembled Polyethylenimine-Graft-Poly(ε-Caprolactone) Micelles as Potential Dual Carriers of Genes and Anticancer Drugs. *Biomaterials* **2007**, *28* (28), 4132–4142. https://doi.org/10.1016/j.biomaterials.2007.05.035.

(42) Hartland, G. V.; Grieser, F.; White, L. R. Surface Potential Measurements in Pentanol–Sodium Dodecyl Sulphate Micelles. *J. Chem. Soc. Faraday Trans. 1 Phys. Chem. Condens. Phases* **1987**, *83* (3), 591. https://doi.org/10.1039/f19878300591.

(43) Tanford, C. *The Hydrophobic Effect: Formation of Micelles and Biological Membranes*, 2d ed.; Wiley: New York, 1980.

(44) Israelachvili, J. N.; Mitchell, D. J.; Ninham, B. W. Theory of Self-Assembly of Hydrocarbon Amphiphiles into Micelles and Bilayers. *J. Chem. Soc. Faraday Trans. 2* **1976**, *72* (0), 1525. https://doi.org/10.1039/f29767201525.

(45) French, R. A.; Jacobson, A. R.; Kim, B.; Isley, S. L.; Penn, R. L.; Baveye, P. C. Influence of Ionic Strength, PH, and Cation Valence on Aggregation Kinetics of Titanium Dioxide Nanoparticles. *Environ. Sci. Technol.* **2009**, *43* (5), 1354–1359. https://doi.org/10.1021/es802628n.

(46) Zhang, L.; Eisenberg, A. Morphogenic Effect of Added Ions on Crew-Cut Aggregates of Polystyrene-b-Poly(Acrylic Acid) Block Copolymers in Solutions. *Macromolecules* **1996**, *29* (27), 8805–8815. https://doi.org/10.1021/ma961376t.

(47) Andrews, J. M. Determination of Minimum Inhibitory Concentrations. *J. Antimicrob. Chemother.* **2001**, *48* (suppl_1), 5–16. https://doi.org/10.1093/jac/48.suppl_1.5.

(48) Kirchhofer, N. D.; Chen, X.; Marsili, E.; Sumner, J. J.; Dahlquist, F. W.; Bazan, G. C. The Conjugated Oligoelectrolyte DSSN+ Enables Exceptional Coulombic Efficiency via Direct Electron Transfer for Anode-Respiring Shewanella Oneidensis MR-1-a Mechanistic Study. *Phys. Chem. Chem. Phys.* **2014**, *16* (38), 20436–20443. https://doi.org/10.1039/c4cp03197k.

(49) Von Canstein, H.; Ogawa, J.; Shimizu, S.; Lloyd, J. R. Secretion of Flavins by Shewanella Species and Their Role in Extracellular Electron Transfer. *Appl. Environ. Microbiol.* **2008**, *74* (3), 615–623. https://doi.org/10.1128/AEM.01387-07.

(50) Okamoto, A.; Hashimoto, K.; Nealson, K. H.; Nakamura, R. Rate Enhancement of Bacterial Extracellular Electron Transport Involves Bound Flavin Semiquinones. *Proc. Natl. Acad. Sci. U. S. A.* **2013**, *110* (19), 7856–7861. https://doi.org/10.1073/pnas.1220823110.

(51) Ross, D. E.; Brantley, S. L.; Tien, M. Kinetic Characterization of OmcA and MtrC, Terminal Reductases Involved in Respiratory Electron Transfer for Dissimilatory Iron Reduction in Shewanella Oneidensis MR-1. *Appl. Environ. Microbiol.* **2009**, *75* (16), 5218–5226. https://doi.org/10.1128/AEM.00544-09.

(52) Okamoto, A.; Kalathil, S.; Deng, X.; Hashimoto, K.; Nakamura, R.; Nealson, K. H. Cell-Secreted Flavins Bound to Membrane Cytochromes Dictate Electron Transfer Reactions to Surfaces with Diverse Charge and PH. *Sci. Rep.* **2014**, *4*, 1–8. https://doi.org/10.1038/srep05628.

(53) Yang, Y.; Ding, Y.; Hu, Y.; Cao, B.; Rice, S. A.; Kjelleberg, S.; Song, H. Enhancing Bidirectional Electron Transfer of Shewanella Oneidensis by a Synthetic Flavin Pathway. *ACS Synth. Biol.* **2015**, *4* (7), 815–823. https://doi.org/10.1021/sb500331x.

(54) Léger, C.; Bertrand, P. Direct Electrochemistry of Redox Enzymes as a Tool for Mechanistic Studies. *Chem. Rev.* **2008**, *108* (7), 2379–2438. https://doi.org/10.1021/cr0680742.

(55) Okamoto, A.; Nakamura, R.; Nealson, K. H.; Hashimoto, K. Bound Flavin Model Suggests Similar Electron-Transfer Mechanisms in Shewanella and Geobacter. *ChemElectroChem* **2014**, *1* (11), 1808–1812. https://doi.org/10.1002/celc.201402151.

(56) Richardson, D. J.; Butt, J. N.; Fredrickson, J. K.; Zachara, J. M.; Shi, L.; Edwards, M. J.; White, G.; Baiden, N.; Gates, A. J.; Marritt, S. J.; Clarke, T. A. The "porin-Cytochrome" Model for Microbe-to-Mineral Electron Transfer. *Mol. Microbiol.* **2012**, *85* (2), 201–212. https://doi.org/10.1111/j.1365-2958.2012.08088.x.

(57) Clarke, T. A.; Edwards, M. J.; Gates, A. J.; Hall, A.; White, G. F.; Bradley, J.; Reardon, C. L.; Shi, L.; Beliaev, A. S.; Marshall, M. J.; Wang, Z.; Watmough, N. J.; Fredrickson, J. K.; Zachara, J. M.; Butt, J. N.; Richardson, D. J. Structure of a Bacterial Cell Surface Decaheme Electron Conduit. *Proc. Natl. Acad. Sci.* **2011**, *108* (23), 9384–9389. https://doi.org/10.1073/pnas.1017200108.

(58) Malcolmson, R. J.; Beswick, P. H.; Privat, P. O.; Saunier, L. DSC of DMPC Liposomes Containing Low Concentrations of Cholesteryl Esters or Cholesterol. *J. Memb. Sci.* **1997**, *123*, 243–253.

(59) Hinks, J.; Wang, Y.; Poh, W. H.; Donose, B. C.; Thomas, A. W.; Wuertz, S.; Loo, S. C. J.; Bazan, G. C.; Kjelleberg, S.; Mu, Y.; Seviour, T. Modeling Cell Membrane Perturbation by Molecules Designed for Transmembrane Electron Transfer. *Langmuir* **2014**, *30* (9), 2429–2440. https://doi.org/10.1021/la403409t.

(60) Chidsey, C. E. D.; Bertozzi, C. R.; Putvinski, T. M.; Mujsce, A. M. Coadsorption of Ferrocene-Terminated and Unsubstituted Alkanethiols on Gold: Electroactive Self-Assembled Monolayers. *J. Am. Chem. Soc.* **1990**, *112* (11), 4301–4306. https://doi.org/10.1021/ja00167a028.

(61) Creager, S. E.; Rowe, G. K. Solvent and Double-Layer Effects on Redox Reactions in Self-Assembled Monolayers of Ferrocenyl-Alkanethiolates on Gold. *J. Electroanal. Chem.* **1997**, *420* (1–2), 291–299. https://doi.org/10.1016/S0022-0728(96)04785-7.

(62) Fujii, S.; Kurokawa, S.; Murase, K.; Lee, K. H.; Sakai, A.; Sugimura, H. Self-Assembled Mixed Monolayer Containing Ferrocenylthiol Molecules: STM Observations and Electrochemical Investigations. *Electrochim. Acta* **2007**, *52* (13), 4436–4442. https://doi.org/10.1016/j.electacta.2006.12.026.

(63) Rudnev, A. V.; Zhumaev, U.; Utsunomiya, T.; Fan, C.; Yokota, Y.; Fukui, K. I.; Wandlowski, T. Ferrocene-Terminated Alkanethiol Self-Assembled Monolayers: An Electrochemical and in Situ Surface-Enhanced Infra-Red Absorption Spectroscopy Study. *Electrochim. Acta* **2013**, *107* (3), 33–44. https://doi.org/10.1016/j.electacta.2013.05.134.

(64) Oh, S.; Min, B.; Logan, B. E. Cathode Performance as a Factor in Electricity Generation in Microbial Fuel Cells. *Environ. Sci. Technol.* **2004**, *38* (18), 4900–4904. https://doi.org/10.1021/es049422p.

(65) Jacob, C.; Yang, H.-T.; H., A.; O., H. Electrochemical Investigations of a Novel Ferrocene Surfactant - ScienceDirect. *J. Electroanal. Chem.* **1996**, *416* (1–2), 83–88.

(66) Stone, D. L.; Smith, D. K.; McGrail, P. T. Ferrocene Encapsulated within Symmetric Dendrimers: A Deeper Understanding of Dendritic Effects on Redox Potential. *J. Am. Chem. Soc.* **2002**, *124* (5), 856–864. https://doi.org/10.1021/ja0117478.

(67) Balavoine, G. G. A.; Doisneau, G.; Fillebeen-Khan, T. An Improved Synthesis of Ferrocene-1,1′-Dicarbaldehyde. *J. Organomet. Chem.* **1991**, *412* (3), 381–382. https://doi.org/10.1016/0022-328X(91)86082-2.

(68) Plater, M. J.; Jackson, T. Polyaromatic Amines. Part 3: Synthesis of Poly(Diarylamino)Styrenes and Related Compounds. *Tetrahedron* **2003**, *59* (25), 4673–4685. https://doi.org/10.1016/S0040-4020(03)00520-9.

(69) Flaherty, D. P.; Walsh, S. M.; Kiyota, T.; Dong, Y.; Ikezu, T.; Vennerstrom, J. L. Polyfluorinated Bis-Styrylbenzene β-Amyloid Plaque Binding Ligands. *J. Med. Chem.* **2007**, *50* (20), 4986–4992. https://doi.org/10.1021/jm070085f.

(70) Gharib, B.; Hirsch, A. Synthesis and Characterization of New Ferrocene-Containing Ionic Liquids. *European J. Org. Chem.* **2014**, *2014* (19), 4123–4136. https://doi.org/10.1002/ejoc.201400061.

(71) Bond, D. R.; Lovley, D. R. Electricity Production by Geobacter Sulfurreducens Attached to Electrodes Electricity Production by Geobacter Sulfurreducens Attached to Electrodes. *Appl. Environ. Microbiol.* **2003**, *69* (3), 1548–1555. https://doi.org/10.1128/AEM.69.3.1548.

(72) Parry, E. P.; Osteryoung, R. A. Evaluation of Analytical Pulse Polarography. *Anal. Chem.* **1965**, *37* (13), 1634–1637. https://doi.org/10.1021/ac60232a001.

(73) Voß, T.; Gründler, P.; Kirbs, A.; Flechsig, G.-U. Temperature Pulse Voltammetry: Hot Layer Electrodes Made by LTCC Technology. *Electrochem. commun.* **1999**, *1* (9), 383–388. https://doi.org/10.1016/S1388-2481(99)00079-X.

Chapter **3**

Hydration Increases Both Electronic and Ionic Conductivity in Self-Doped Conjugated Polyelectrolytes

Materials that conduct both electrical carriers and ions have applications in energy storage, bioelectronics, and soft robotics. Polymer-based mixed conducting materials generally consist of molecular or polymeric acids doping a π-conjugated polymer. While these acids are important for mixed conduction, their absorption of water changes the morphology and conductive properties of the bulk material. How hydration impacts conduction remains unexplored for self-doped conjugated polyelectrolytes (CPEs), which have ionic groups appended to a π-conjugated backbone. Conduction of holes and ions in films of a cyclopentadithiophene-*alt*-benzothiadiazole polymer with pendant sulfonate groups (CPE-K) was measured starting from a largely dry state. While hole conduction dominates in dry CPE-K films, hydration at > 70% relative humidity generates commensurate ion conduction. As films are hydrated to 100% relative humidity, hole and ion conductivities increase to 50 ± 3 mS cm^{-1} and 70 ± 9 mS cm^{-1}, respectively In-situ UV/Vis/NIR absorbance spectroscopy and electron paramagnetic resonance (EPR) spectroscopy reveal that the charge-carrier

population of polarons (radical cations) in CPE-K increased, but negligibly in comparison to the increase in the conductivity, suggesting electronic mobility changes. The potential mobility changes is supported by Grazing Incidence Wide Angle X-ray Scattering, where the bimodal distribution of π-π stacking distances seen in dry films becomes unimodal at the closer stacking distance in hydrated films, indicating enhanced crystallinity. Humidity leads to greater solvation of ions and the increased crystal correlation lengths indicate more pathways for ionic transport. These findings give insight as to how hydration affects both conduction mechanisms in CPEs and paves the way for improved molecular design and processing protocols that increase mixed conduction simultaneously.

3.1 Introduction

Polymeric materials that transport ions in addition to electrons/holes are a class of materials that links polymer electrolytes with ion-only conductivity to organic semiconductors with electron/hole-only conductivity. Mixed conduction underpins applications that require an ionically conducting medium to be interfaced with an electronically conducting material, as is found in organic electrochemical devices such as batteries, supercapacitors, electrochromic and light emitting devices.[1–3] Due to their soft and biocompatible nature, mixed electron/ionic conducting polymers have also been employed in many bioelectronic applications, including neural probes, soft actuators for artificial muscles and drug delivery, and organic electrochemical transistors (OECTs) for biosensing and monitoring.[4–6]

Polymer-based mixed conducting materials generally incorporate molecular or polymeric acids with a π-conjugated polymer. The acids dope the polymer by oxidizing or protonating the polymer backbone, allowing it to attain its electronically conducting state

due to the higher concentration of free charge-carriers.[7–10] The conjugate base of the acid also serves as counterions to balance the charge in the conducting polymer, creating a possible route of ion conduction. However, most acid dopants/charge balancing agents are hygroscopic. Hydration impacts ionic conductivity and can also change the morphology of the conducting polymer through plasticization. For example, the well-known conductive polymer blend of poly(3,4-ethylenedioxythiophene) doped with poly(styrenesulfonate), PEDOT:PSS, shows anti-correlation between its electronic and ionic conductivity when hydrated.[11–13] The decrease in electron conductivity with humidity is attributed to swelling of the insulating PSS domains in the polymer morphology, which increases the separation of the PEDOT-rich hole-conducting domains.[14,15] To what extent these mechanisms extend to other mixed transport organic semiconductors remains under explored.

In this study, we consider the role hydration plays in the mixed conduction properties and morphology of anionic conjugated polyelectrolytes (CPEs). In CPEs, the anion is incorporated as a pendant group directly on the polymer backbone.[16] While CPEs have been used extensively as interlayers in organic solar cells and light emitting diodes, and their charge conduction is well documented, they are only just emerging as materials for mixed conducting applications. In previous reports CPEs have been oxidized by external chemical dopants such as F_4TCNQ to boost their electronic hole conductivity while maintaining their ionic conductivity.[13,17] Here we consider a narrow band gap CPE that self-dopes in water, called CPE-K, whose chemical structure is shown in **Figure 3.1**. Because the dopant is a proton and water is a ubiquitous solvent, CPE-K can be more readily doped even with limited scientific resources when compared to those that require the use of an external dopant molecule. In this investigation we quantify the role hydration plays in the conduction

properties and morphology of self-doped CPE-K to enable more targeted molecular design and effective processing protocols for mixed conductors. Impedance spectroscopy and DC polarization were used to measure conduction starting from dry films as a function of increasing hydration though change in humidity. Since conduction relies on the number of free charge carriers and their mobility through the material, charge carrier populations were characterized by UV/Vis/NIR absorbance spectroscopy and electron paramagnetic resonance (EPR) spectroscopy. Polymer morphology was studied with grazing-incidence wide angle X-ray scattering (GIWAXS).

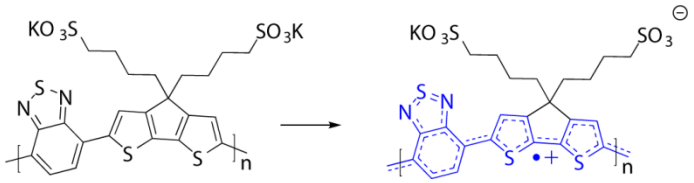

CPE-K

Figure 3.1: Chemical structure of CPE-K in its neutral and doped form.

3.2 Mixed Conduction

The effect of hydration on mixed conduction of electrons and ions in CPE-K films was probed using electrochemical impedance spectroscopy (EIS) and DC polarization. Representative Nyquist plots as a function of relative humidity are shown in **Figure 3.2a and b**. From a largely dry state up to 70% relative humidity, the spectra show only one single semicircle. A single semicircle is indicative of a single dominant pathway for charge transport and the lack of a capacitive tail at low frequencies is consistent with transport being dominated by electric charge.[18] For fitting of the spectra with an equivalent circuit and DC measurements, we refer to the Supporting Information **Figure 3.S1**. Importantly, the DC

measurements agree and confirms the low frequency, electronic resistance R_e obtained from the EIS modelling, which was used to calculate the electronic conductivity σ_e via

$$\sigma_e = \frac{l}{R_e \cdot h \cdot w} \tag{3.1}$$

where l, h, and w are the length, thickness, and width of the polymer film between gold electrodes. The average conductivity of dry CPE-K films was 12 ± 2 mS cm^{-1}, which is in the range of reported in-plane conductivities for spin-cast CPE-K films (1.5 to 24 mS cm^{-1}).[19–21] The sample resistance decreases as can be observed by the shrinking of the semicircle with increasing humidity, leading to an increase of hole conductivity in the CPE-K films, as summarized in Figure 3.2c.

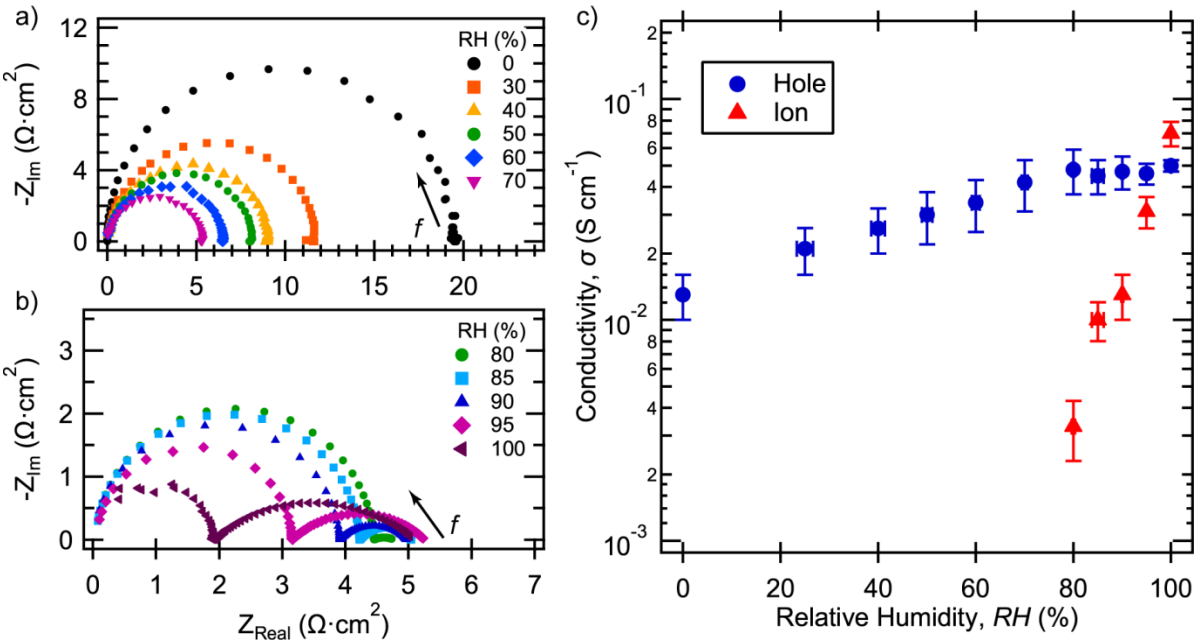

Figure 3.2:. Mixed conductivity with relative humidity (RH) in CPE-K films at 25 ˚C. Representative Nyquist plots from a) dry films up to 70% RH and b) from 80% to 100% RH. The arrows indicates the direction of increasing frequency, *f*. c) Averaged electronic and ionic conductivity values in hydrated CPE-K films

calculated from equivalent circuit fitting. Error bars represent ± 1 standard deviation (n = 4).

Ion motion in the CPE-K films is not ascertainable by EIS until the onset of a low frequency semicircle in the Nyquist plot. As seen in Figure 3.2b, at 80% relative humidity and above, the spectra consist of two semicircles, which suggest multiple charge transport pathways in hydrated CPE-K films. This behavior can be explained by a mixed conductivity of electronic and ionic charge carriers. The lack of a capacitive tail at low frequencies again supports that there are continuous pathways for the transport of electronic charge.[18] Between 80% and 100% relative humidity, the low frequency electronic resistance remains rather constant and is confirmed by DC measurements due to the ion-blocking gold electrodes. The average hole conductivity at 100% RH was 50 ± 3 mS cm^{-1}. By assuming the CPE-K films contain bi-continuous ion- and hole-conducting channels, an equivalent circuit that represents the parallel combination of these processes can be applied to extract the ionic resistance (see **Figure 3.S2**). This parallel circuit has been used previously in the literature for mixed conducting systems.[11,13,22] As hydration increases, the weight shifts from the high frequency semicircle to the low frequency semicircle, providing the ionic conductivity ranging from 3 ± 1 to 70 ± 9 mS cm^{-1} between 80% and 100% RH.

The trend in hole and ion conductivity with hydration can be partially explained by the water content in the film and the role it has in the self-doping process of CPE-K. Recently, it was found that the doping of CPE-K begins with protonation of the polymer backbone followed by single electron transfer from an adjacent polymer to form a polaron (radical cation or hole).[23] When doping occurs, the anionic sulfonate groups stabilize the polarons on the backbone, thus eliminating the need for the K^+ counterions. In our CPE-K

films, the effect of hydration is two-fold: allowing further doping of the CPE-K and solvating ions – both of which would lead to increased mixed conduction. However, because we also expect hydration to plasticize the CPE-K films, changes in mobility of charge carriers in the films due to shifts in film morphology must also be considered to account for the change in mixed conduction.

3.3 Charge Carrier Populations

Absorbance spectroscopy can be used to examine the level of doping, which can be related to the number of free charge carriers that can participate in charge transport. CPE-K exhibits a large absorption band from 300 nm to 1500 nm, with three peaks positioned at 412 nm, 700 nm (λ_{max}), and 1100 nm. The features at wavelengths < 1000 nm are characteristic of the neutral semiconducting polymer CPDT-*alt*-BT backbone.[24,25] The primary charge-carriers for CPE-K are positive polarons, with their optical transition assigned to the 1100 nm peak ($\lambda_{polaron}$).[19,26] From **Figure 3.3**, the polaron peak can be tracked as the film is hydrated. The level of doping, and therefor charge-carrier population, can be estimated by the ratio of the relative intensities of the neutral and polaron peaks ($\lambda_{polaron}/\lambda_{max}$). This ratio increases by 10% between the dry and humidified films, signifying an increase in the charge-carrier population. The increase in the number of charge-carriers in the film contributes to the increase in electronic conductivity. However, because the change in doping (10%) is not proportional to the order-of-magnitude change in conductivity (~300%), other factors must be considered.

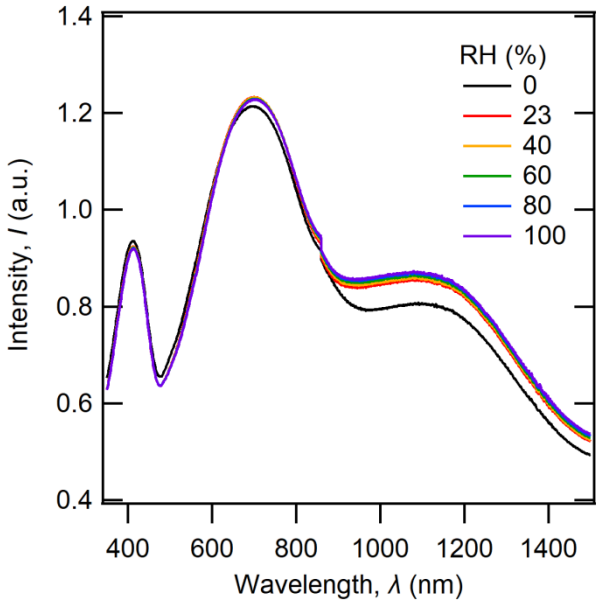

Figure 3.3: UV/Vis/NIR absorbance spectroscopy for a CPE-K film starting from dry and humidified to different RH levels.

In order to confirm the results from the absorbance spectroscopy, we turn to electron paramagnetic resonance (EPR) studies to investigate the free radical properties of CPE-K to gain additional insight into the behavior of the electronic charge carrier. Since CPE-K is a thiophene based polymer we anticipate, like for PEDOT:PSS, that the free radical signal to originate from the cationic polaron charge carrier.[19,27] As for our other measurements above, we performed an *in situ* hydration dependent continuous wave (CW) EPR at X-band on CPE-K, with example data depicted in **Figure 3.4a**. As can be seen, there is a clear change in the spectra with hydration. The change occurs to both the line width as well as the peak height, which is quantified in Figure 3.4b. It can be seen that initially there is no change at low hydration, but as the water content is increased, the spectra both narrows (Figure 3.4b) and the intensity increases (Figure 3.4c). Since both the height and line width is changing, the peak to peak height change can't be employed as a proxy for the change in the free radical concentration. Furthermore, there may be multiple species present as has been seen

for other thiophene systems.[28–30] Consequently, we proceeded to model the spectra, which can be seen in **Figure 3.S3** in the supplementary information.

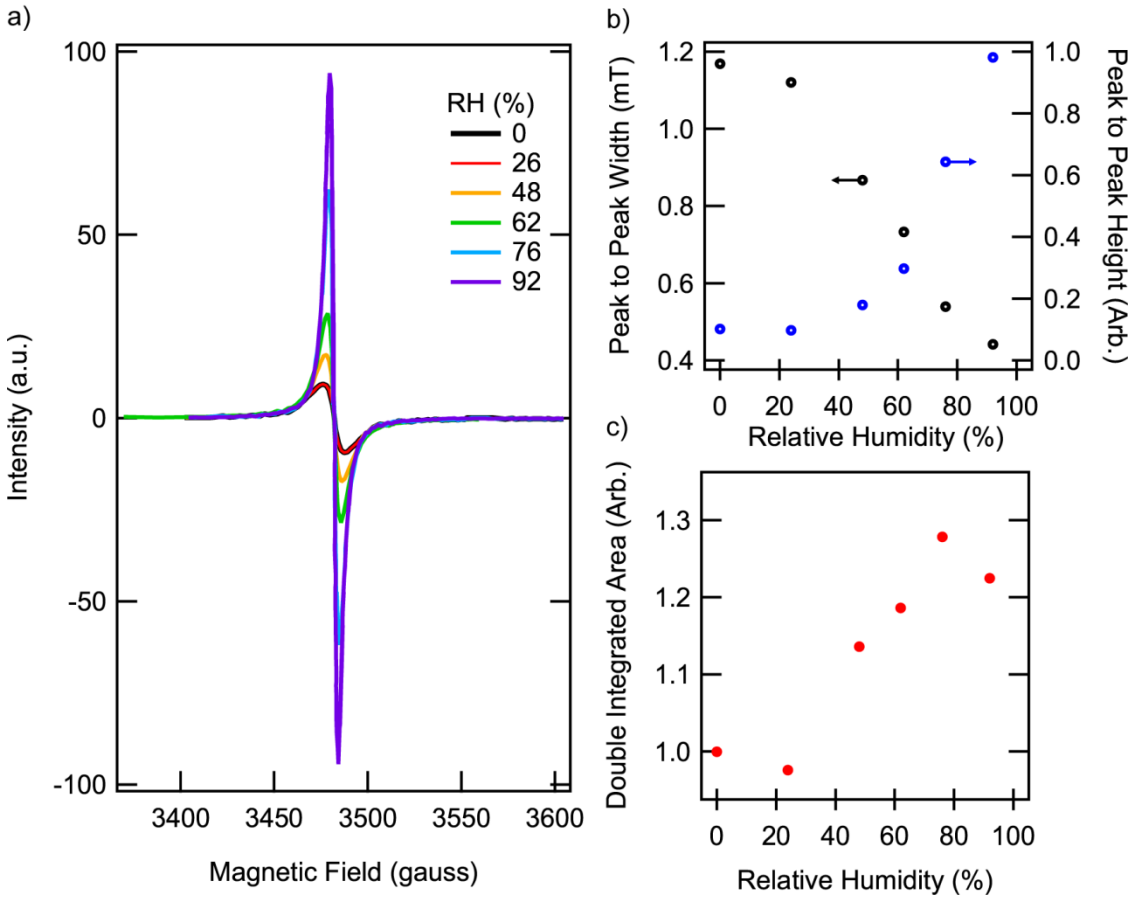

Figure 3.4: CW-EPR at X-band data for CPE-K under hydration control. a) Spectra at different relative humidity indicated in the legend. b) The peak to peak width and peak to peak heightof the EPR spectra as a function of hydration. c) Double integration of the spectra to obtain the relative spin concentration change.

All the curves were well modelled to a single, symmetric pseudo-Voigtian curve of predominantly Lorentzian character (~96%, Figure 3.S3) with an isotropic g value of 2.00235. The g value is commensurate with cationic free radicals as seen in other thiophene systems.[30–32] The fact that only a single curve is sufficient for fitting is different to other thiophene systems, where usually two curves, one Gaussian and one Lorentzian with

differing g values is required to fit the data.[30–32] If there were more than one species in the CPE-K, it would be reasonable to anticipate that the relative Lorentzian and Gaussian weights (a radical to each component) should change as a function of hydration, leading to the line narrowing observed. Given that this is not the case (Figure 3.S3b) we conclude that it is unlikely that there are two radical species. Therefore, the change in the line widths are due to the narrowing of the separate components as plotted in Figure 3.S3c. As a final test to check for multiple species, we obtained power saturation data at each hydration point and modeled the spectra at different microwave powers to see if a change in the relative Gaussian/Lorentzian weights would occur as has been seen for PEDOT:PSS (see **Table 3.S1**).[32] Again, it was observed that there was no change in the pseudo-Voigtian character. As such, the data above argues for a single species.

Having argued for one radical species only, we turn to the lineshape behavior, which has been quantified in Figure 3.4b. The first basic observation is that for a radical, the line width is fairly broad. This is most likely due to delocalization of the radical along the backbone leading to multiple hyperfine interactions with bonded hydrogen, in agreement with recent transient absorption studies of CPE-K.[31] As to the origin of the line narrowing we first note that the line is predominantly Lorentzian in character, hence inhomogeneous line narrowing is not favored.[32] Initially, the temptation is to assign the behavior due to the formation of bipolarons, a spin zero species as reported elsewhere other thiophene systems.[27,29] However, such species lead to a decrease in EPR intensity, which we manifestly do not see (Figure 3.4a). As such, we tentatively suggest that what is being observed is exchange line narrowing, which can occur in solid state systems of sufficiently high radical concentration

that any more radical production leads to narrowing, which implies that the total free radical concentration of the system should be increasing with hydration.

The above directly leads us to the final result, whether the free radical concentration in CPE-K actually increases with hydration. Given the above changes in the linewidth as well as intensity, we performed a double integration of the spectra to obtain the relative free radical concentration change, the results of which is depicted in Figure 3.4c. Clearly, there is an increase in the concentration with relative humidity. Initially, at the low hydration levels, there is no change, but then there is a linear increase followed by a saturation of the concentration at 30% more radicals. This 30% increase is of a similar order of magnitude as observed for the UV-Vis data above.

The EPR work as well as the UV-Vis work shows an electronic charge concentration increase that severely underestimates the conductivity changes observed. Hence, it naturally follows that to explain the difference the mobility of the electronic carriers must be increasing as well with hydration. One major contributor to potential mobility changes is changes in morphology, which we investigate below.

3.4 Morphology

Molecular ordering in conjugated polymer films is a relevant parameter that influences charge carrier mobility and therefore conductivity. To investigate the impact of hydration on CPE-K chain stacking and crystallinity, grazing incidence wide-angle X-ray scattering (GIWAXS) data was collected during in-situ humidification of films. **Figure 3.S4** shows two-dimensional GIWAXS images corresponding to a CPE-K film at low and high hydration (17% and 90% RH, respectively). We see a strong edge-on texture at low-q, while features at intermediate- and high-q have a more isotropic orientation. As the film is

hydrated, the features become less diffuse indicating better crystallinity. **Figure 3.5** and **Figure 3.S5** shows the out-of-plane and in-plane line cuts, respectively, for CPE-K films in the dry and hydrated states. **Table 3.S2** summarizes relevant GIWAXS parameters. At the out-of-plane higher q values, π-π stacking distances (d) suitable for inter-chain transport can be seen for both cases. For the dry film, there are two populations: q_z = 1.79 Å^{-1} and 1.59 Å^{-1} (d = 3.51 Å and 3.94 Å). With increase in humidity the population shifts to higher q-spacing, indicating a higher portion of the film has close π-π stacking (q_z = 1.74 Å^{-1}, d = 3.61 Å). Calculation of the crystal correlation length (*CCL*) from the peak full width at half maximum via the Scherrer equation shows similar crystallite sizes at the higher q, *CCL* ≈ 2.5 nm.[20,33] The closer π-π stacking of the humidified CPE-K would lead to increased charge-carrier mobility through the film and contribute to the increased hole conduction.

At the lower q range, both dry and humidified films show lamellar stacking peaks at q_z ≈ 0.31 Å^{-1} (d = 20 Å). Upon hydration, the *CCL* dramatically increases for the lamellar spacing feature, changing from 8.30 nm for dry films to 11.4 nm for humidified films. A larger *CCL* corresponds to larger or more perfect crystallites as humidity increases. Furthermore, the humidified sample also showed lamellar reflection peaks at q_z = 0.62 Å^{-1} and 0.93 Å^{-1}, which is a similar feature seen in the high mobility neutral polymer.[34]

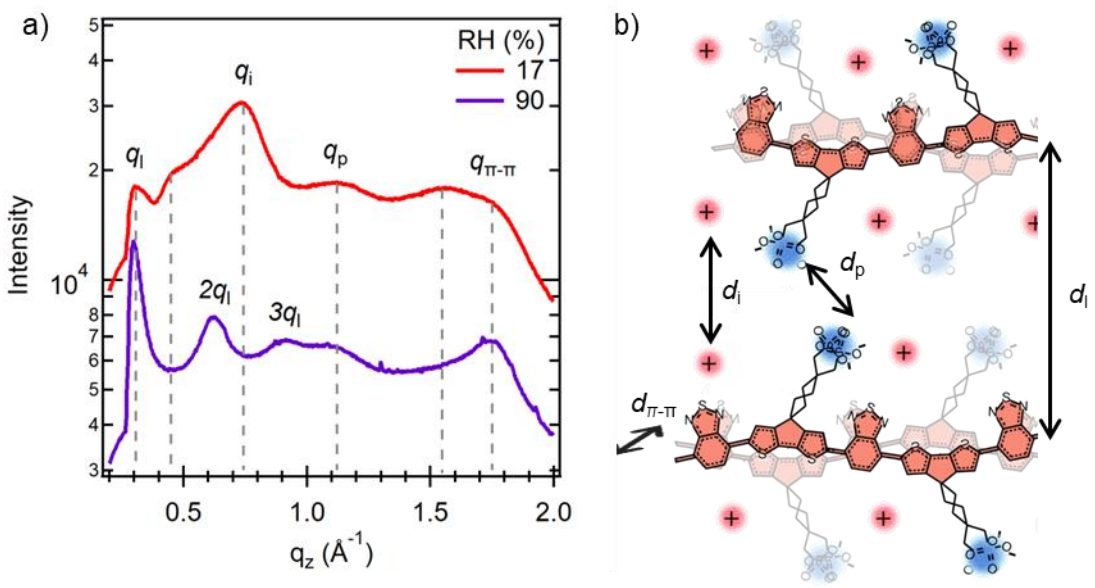

Figure 3.5: Polymer morphology from GIWAXs. a) Out-of-plane line cuts from two-dimensional GIWAXS patterns of CPE-K films drop-cast on silicon substrates. b) Cartoon schematic of molecular packing features identifying lamellar (d_l), pendant (d_p), ion aggregate (d_i), and π-π stacking ($d_{\pi-\pi}$) spacing.

Additional peaks in the intermediate-q range are reminiscent of stacking peaks seen for polyelectrolytes and polymerized ionic liquids. Studies of polymerized ionic liquids exhibiting intermediate stacking peaks from 0.7 to 1.3 Å^{-1} attribute them to ion aggregate spacing and correlation between pendant chains, respectively.[35–37] Dry CPE-K films show a peak at q_z = 1.14 Å^{-1} (d = 5.53 Å), which can be attributed to correlation between the sulfonate pendant groups. This spacing does not change substantially for humidified films (q_z = 1.09 Å^{-1}, d = 5.75 Å). The most prominent feature of the dry CPE-K line-cut is located at q_z = 0.74 Å^{-1} (d = 8.5 Å). This peak is assigned as the ion aggregate spacing. When CPE-K is humidified, this peak seemingly disappears. The absence of this peak could be due to the loss of sufficient contrast between the aggregates and the surrounding media to scatter x-rays.[35,38] This supports that the ions in the film are solvated and available for conduction.

Together with the refinement of the lamellar stacking, this provides evidence for increased percolation pathways for ion transport and supports the orders-of-magnitude increase ion conductivity.

3.5 Conclusions

The role of hydration in the mixed conduction of electrical carriers and ions in the self-doping conjugated polyelectrolyte CPE-K was investigated. Dry drop-cast films show only hole conduction, while ion conduction is seen starting above 70% relative humidity. Hole conduction increases with film humidification due to increased levels of doping, a higher prevalence of close π-π stacking, and better delocalization of the polaron charge-carrier throughout the polymer material. Ion conductivity increases with water content, as expected, and routes for conduction are improved with hydration as seen by GIWAXS. Overall, this study provides insight as to how hydration can improve the conduction properties of self-doping CPEs and lead to better molecular designs and processing methods to achieve desired mixed conduction.

3.7 Materials, Methods, & Supplementary Figures

3.7.1 Materials & Methods

Materials: CPE-K was synthesized as previously reported.[19] The molecular weight of CPE-K was determined by GPC of the tetrabutylammonium congener. GPC (DMF): M_n = 7714, M_w = 8166, *PDI* = 1.05.

Conductivity Measurements: Impedance spectroscopy measurements were performed using the in-plane configuration with gold electrodes (500 μm wide, 50 nm thick) with a chromium adhesion layer (2 nm thick) evaporated onto glass substrates (2.4 mm channel

lengths). Films were drop-cast from 10 mg/mL CPE-K in 1:2 H_2O:MeOH and allowed to dry under ambient conditions. Films were then annealed at 80 ˚C for 1 hour and then annealed under vacuum overnight in a glovebox. Prepared films were first measured in a glove box.

Impedance measurements were performed using the two-point-probe method with a Bio-logic SP-300 or VSP-300 Potentiostat. Measurements were taken with the following parameters: E = 0 V vs ref, E_A = 10 mV vs ref, f_i = 7 MHz – 3 MHz, f_f = 10 – 1 mHz . 10 points per decade, averaging over 10 points. Nyquist plots were fit using the Bio-logic Zfit program in the EC-Lab software. DC polarization was performed by biasing the films at -50 mV, -40 mV, -30 mV, 30 mV, 40 mV, and 50 mV with time to rest at OCV between measurements. Film equilibrium at each humidity step was confirmed by performing impedance before and after the DC measurements and showing no change in the spectra.

Film thicknesses and widths were measured using a Dektak Profilometer with 5 mg of force and 6.5 µm amplitude range. Thickness and width were measured after films rested 24 hours in ambient humidity. Dimensions were averaged from at least 5 measurements at different points in the films.

Humidity Control: Humidity was controlled by modulating the ratio of dry nitrogen gas to nitrogen gas passed through a water bubbler. Humidity and temperature were sensed using a probe with measurement errors of 0.3 %RH and 0.01 ˚C.

UV/VIS/NIR absorbance spectroscopy: Measurements were performed using a Perkin Elmer Lambda 750 spectrophotometer at room temperature. Change in doping population was calculated based on a logistic calibration curve created from CPE-K electrochromic devices.

Electron paramagnetic resonance (EPR): Continuous Wave (CW) X-band EPR was performed utilizing a bespoke hydration system that enables *in situ* hydration measurements, which prevents uncertainty in the measurement of the intensity due to changing sample position. Procedure used is as published elsewhere.[19,20] However, in brief, spectra was obtained using a Bruker Biospin Elexsys E500 CW-EPR spectrometer using an X-band, SuperX microwave bridge, a super high Q cavity, a Bruker Biopsin teslameter (ER036TM, calibrated) and an EIP 548B. Sample was measured at room temperature in a standard 3mm cylindrical quartz tube attached to a vacuum capable hydration system. The sample was dried first evacuating the line using a rotary pump ($<10^{-3}$ mbar) for several hours. The vacuum line was then isolated from the pump and a power saturated experiment was conducted (see below). After the experiment, water vaper was bled into the vacuum line (using a degassed water vial) up to a selected water vaper pressure (measured using an Edwards GK series 50 mbar gauge). Hydration was allowed for ~2 hours and a power saturation experiment was performed again. The above steps were repeated for higher hydration levels until a complete isotherm was obtained.

The power saturation experiment was performed centered at ~348 mT with a sweep width of 25 mT taking 4096 data points. Data was obtained from 50 dB to 20 dB at a modulation frequency of 100 kHz and modulation amplitude of 0.01 mT. The main data for analysis was taken from 35 dB data, which was within the linear response of the power saturation behaviour.

The data was modelled using EZSpin (ver. 5.2.28), the pepper functionality (i.e. solid state modelling) using the simplex algorithm while scaling and doing a linear baseline.

Grazing Incidence Wide-angle X-ray scattering (GIWAXS) : GIWAXS patterns were obtained using the humidity control stage at beamline 7.3.3 of the Advanced Light Source (ALS) at Lawrence Berkeley National Laboratory in Berkeley, CA. A sample-detector distance of 294.5 mm was used with an X-ray wavelength of 1.2398 Å corresponding to a beam energy of 10 keV. Scattering angles were calibrated to a silver behenate (AgB) standard. Data were reduced using the Nika package for Igor. The scattering intensity for line-cut data was averaged for each sector. Sectors were defined as follows: in-plane q_{xy} 7˚ to 17˚ and out-of-plane q_z 77˚ to 87˚. Peak centers and peak full width at half maximum (FWHM) were found by fitting the data to Gaussian curves using the Multipeak Fitting package for Igor.

3.7.2 Supplementary Figures & Discussion

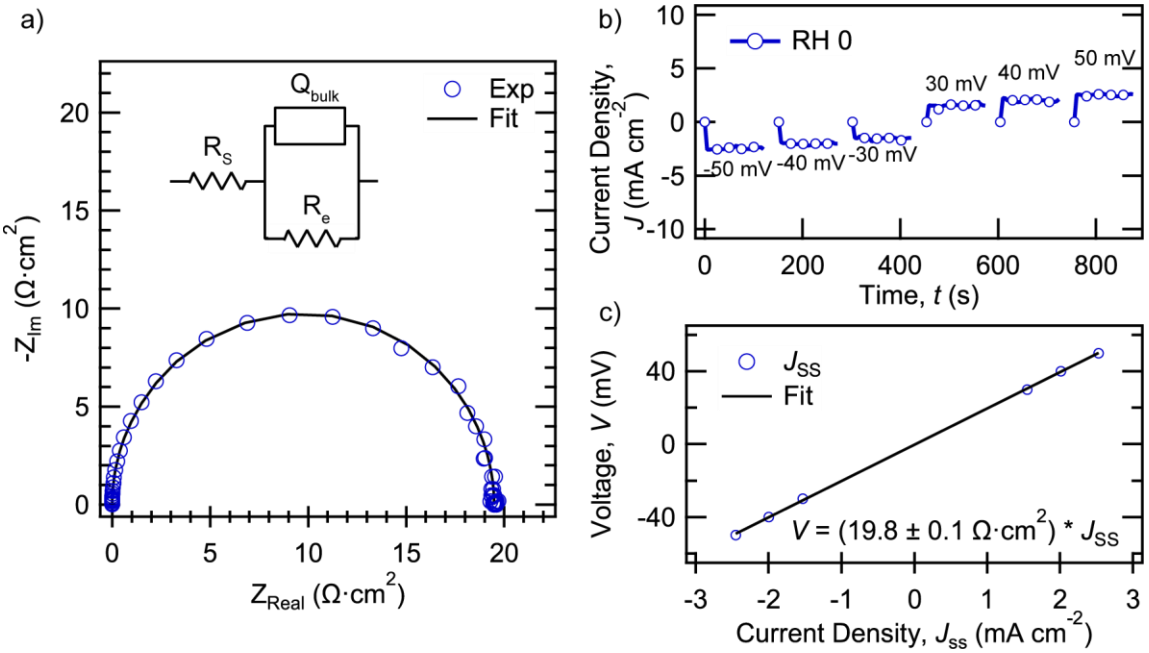

Figure 3.S1: Fitting example for conduction in CPE-K films at low relative humidity (RH). a) Nyquist plot for CPE-K film at 0% RH (open circles) and the corresponding fit (sold curve) using the inset equivalent circuit. b) DC polarization measurements. c) Corresponding Ohm's law plot of DC voltage vs the extracted steady-state current density.

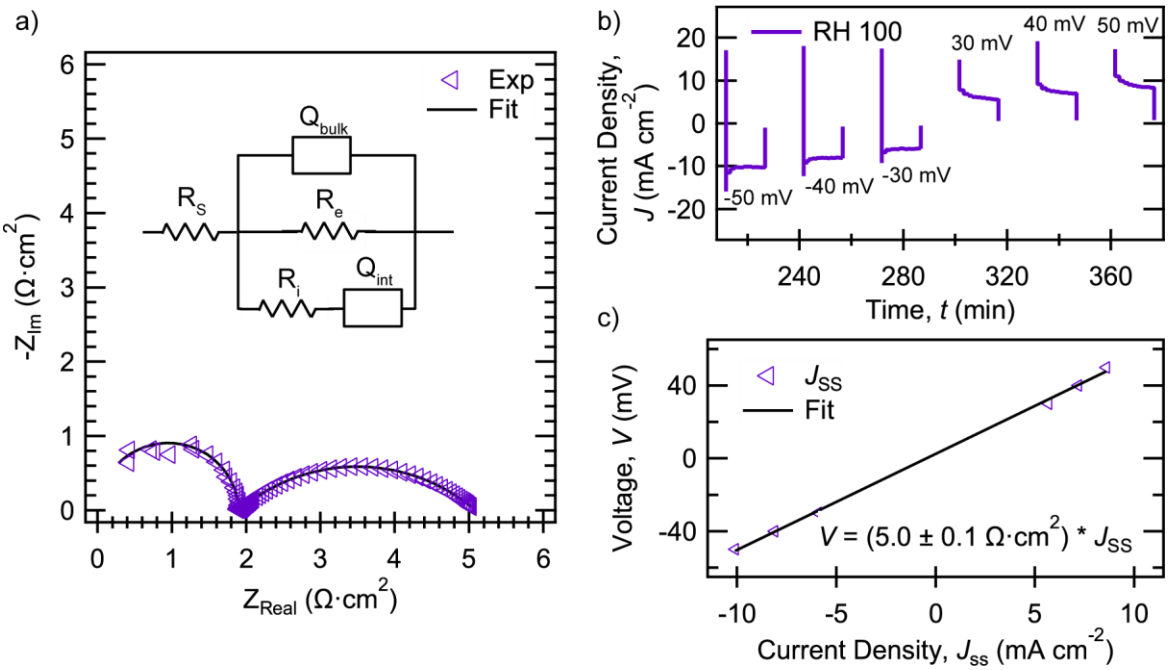

Figure 3.S2: Fitting example for conduction in CPE-K films at high relative humidity (RH). a) Nyquist plot for CPE-K film at 100% RH (open markers) and the corresponding fit (sold curve) using the inset equivalent circuit. b) DC polarization measurements. c) Corresponding Ohm's law plot of DC voltage vs the extracted steady-state current density.

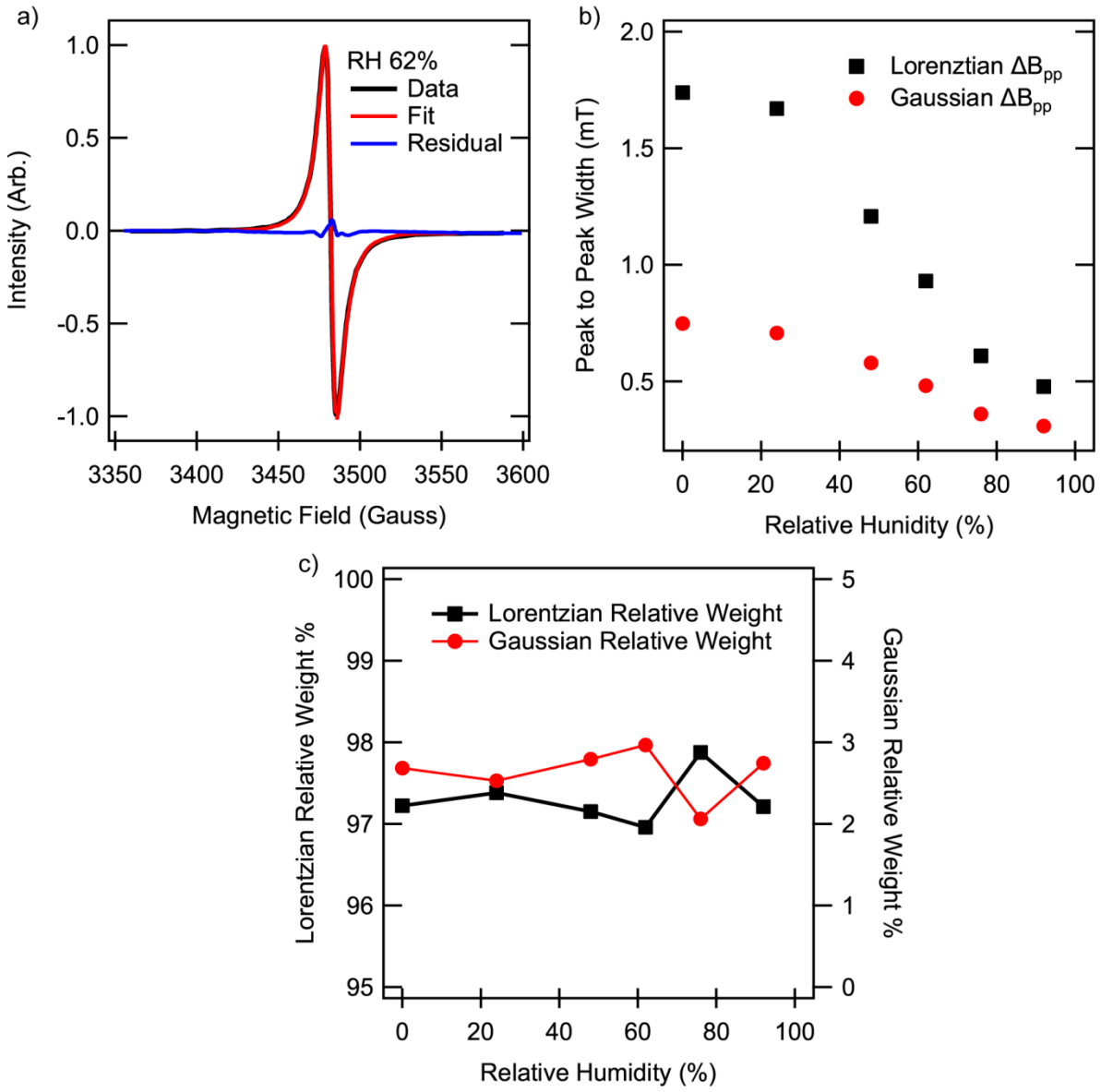

Figure 3.S3: The modelling of the EPR spectra. a) Modelling to a single, isotropic spin ½ system of predominantly Lorentzian character at 35dB. Indicated in blue are the residuals. b) The relative weightings of the pseudo-Voigtian curves used in the fits. c) The peak to peak widths of the separate components of the pseudo-Voigtian as a function of hydration.

Table 3.S1: Fitting parameters obtained for the power saturation data.

Sample Hydration (RH%)	Microwave Power (dB)	Lorentzian Weight (%)	Gaussian Weight (%)
0	47 (low power)	97.2	2.80
	35	97.2	2.77
	23 (high power)	97.2	2.81
92	47 (low power)	97.2	2.81
	35	97.3	2.74
	23 (high power)	97.2	2.80

Discrepancies in adding to 100% due to rounding errors.

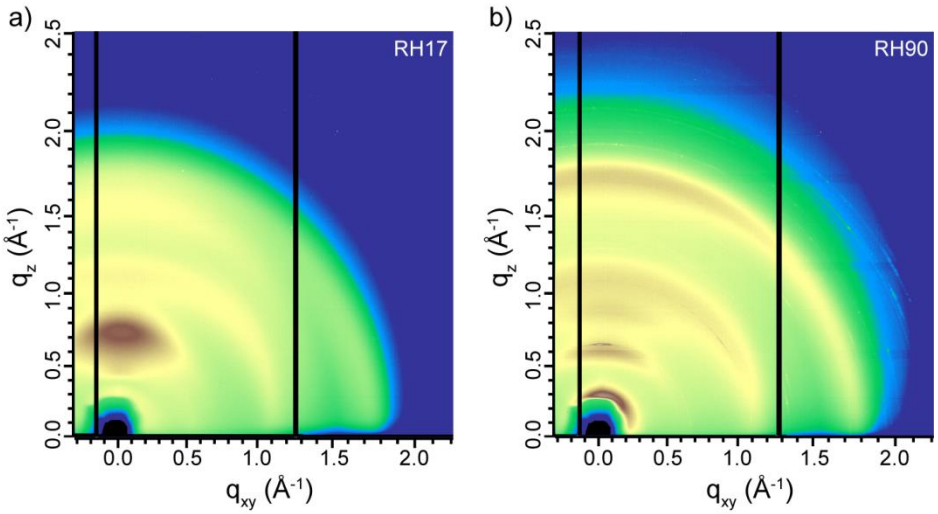

Figure 3.S4: 2D GIWAXs data plots.

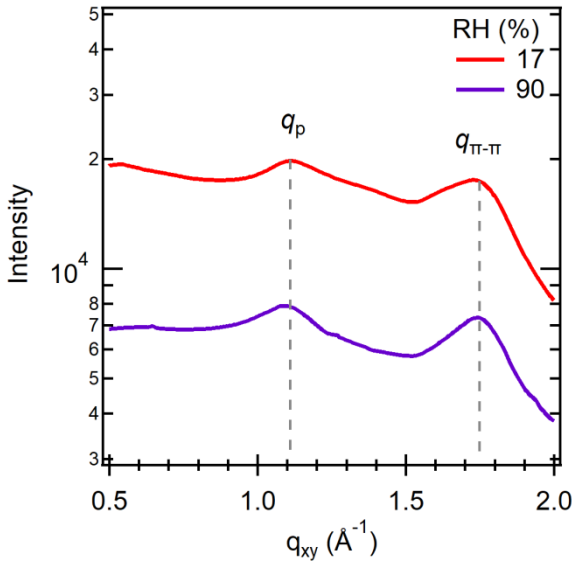

Figure 3.S5: In-plane line cuts from two-dimensional GIWAXS patterns of CPE-K films drop-cast on silicon substrates.

Table 3.S2: Parameters from GI-WAXs

	q_z (Å^{-1})		Distance, d (Å)		Crystal correlation length, *CCL* (nm)	
	dry	humidified	dry	humidified	dry	humidified
π-π	1.79	1.74	3.51	3.61	3.05	2.50
	1.59		3.94		1.95	
Pendant	1.14	1.09	5.52	5.75	3.34	2.90
Ionic aggregate	0.739		8.50		3.62	
	0.543		11.6		1.42	
Lamellar	0.308	0.31	20.4	20.3	8.3	11.37
		0.62		10.1		5.83
		0.93		6.76		4.39
	q_{xy} (Å^{-1})		Distance, d (Å)		Crystal correlation length, *CCL* (nm)	
	dry	humidified	dry	humidified	dry	humidified
π-π	1.75	1.74	3.59	3.61	3.19	2.88
	1.61		3.90		4.89	
Pendant	1.12	1.09	5.61	5.75	3.26	2.94

3.8 Acknowledgements

S. R. M. acknowledges funding from the National Science Foundation Graduate Research Fellowships Program (NSF GRFP) under grant 1650114. Funding was provided by the Institute for Collaborative Biotechnologies (ICB) under grant W911NF-09-D-0001-0044 from the U.S. Army Research Office. Dr. Martin Seifrid collected GIWAXS data with the help of Dr. Chenhui Zhu of the Lawrence Berkley National Lab. This research used resources of the Advanced Light Source, a U.S. DOE Office of Science User Facility under contract no. DE-AC02-05CH11231. In-situ EPR measurements and analysis were performed by Dr. A. Bernard Mostert. A.B.M. acknowledges the Australian Research Council through its Discovery Program (DP140103653) and is a Sêr Cymru II Fellow and the results incorporated in this work have received funding from the European Union's Horizon 2020 research and innovation program under the Marie Skłodowska-Curie grant agreement No 663830. S. R. M. also gratefully acknowledges Prof. Susannah Scott for help in drafting the original manuscriptthis chapter is based on in her CHE 594 Scientific Writing course.

3.9 References

(1) Hernández, G.; Casado, N.; Zamarayeva, A. M.; Duey, J. K.; Armand, M.; Arias, A. C.; Mecerreyes, D. Perylene Polyimide-Polyether Anodes for Aqueous All-Organic Polymer Batteries. *ACS Appl. Energy Mater.* **2018**, *1* (12), 7199–7205. https://doi.org/10.1021/acsaem.8b01663.

(2) Bryan, A. M.; Santino, L. M.; Lu, Y.; Acharya, S.; D'Arcy, J. M. Conducting Polymers for Pseudocapacitive Energy Storage. *Chem. Mater.* **2016**, *28* (17), 5989–5998. https://doi.org/10.1021/acs.chemmater.6b01762.

(3) Tekoglu, S.; Petzoldt, M.; Stolz, S.; Bunz, U. H. F.; Lemmer, U.; Hamburger, M.; Hernandez-Sosa, G. Emissive Polyelectrolytes As Interlayer for Color Tuning and Electron Injection in Solution-Processed Light-Emitting Devices. *ACS Appl. Mater.*

Interfaces **2016**, *8* (11), 7320–7325. https://doi.org/10.1021/acsami.6b00665.

(4) Uguz, I.; Proctor, C. M.; Curto, V. F.; Pappa, A. M.; Donahue, M. J.; Ferro, M.; Owens, R. M.; Khodagholy, D.; Inal, S.; Malliaras, G. G. A Microfluidic Ion Pump for In Vivo Drug Delivery. *Adv. Mater.* **2017**, *29* (27), 1–6. https://doi.org/10.1002/adma.201701217.

(5) Smela, E. Conjugated Polymer Actuators for Biomedical Applications. *Adv. Mater.* **2003**, *15* (6), 481–494. https://doi.org/10.1002/adma.200390113.

(6) Savva, A.; Hallani, R.; Cendra, C.; Surgailis, J.; Hidalgo, T. C.; Wustoni, S.; Sheelamanthula, R.; Chen, X.; Kirkus, M.; Giovannitti, A.; Salleo, A.; McCulloch, I.; Inal, S. Balancing Ionic and Electronic Conduction for High-Performance Organic Electrochemical Transistors. *Adv. Funct. Mater.* **2020**, *30* (11). https://doi.org/10.1002/adfm.201907657.

(7) Chiang, C. K.; Park, Y. W.; Heeger, A. J.; Shirakawa, H.; Louis, E. J.; MacDiarmid, A. G. Conducting Polymers: Halogen Doped Polyacetylene. *J. Chem. Phys.* **1978**, *69* (11), 5098–5104. https://doi.org/10.1063/1.436503.

(8) Audenaert, M.; Gusman, G.; Deltour, R. Electrical Conductivity of I2-Doped Polyacetylene. *Phys. Rev. B* **1981**, *24* (12), 7380–7382. https://doi.org/10.1103/PhysRevB.24.7380.

(9) MacDiarmid, A. G.; Mammone, R. J.; Kaner, R. B.; Porter, S. J. The Concept of 'Doping' of Conducting Polymers: The Role of Reduction Potentials. *Philos. Trans. R. Soc. London. Ser. A, Math. Phys. Sci.* **1985**, *314* (1528), 3–15. https://doi.org/10.1098/rsta.1985.0004.

(10) Moon, H. S.; Park, J. K. Structural Effect of Polymeric Acid Dopants on the Characteristics of Doped Polyaniline Composites. *Synth. Met.* **1998**, *92* (3), 223–228. https://doi.org/10.1016/s0379-6779(98)80090-8.

(11) Wang, H.; Ail, U.; Gabrielsson, R.; Berggren, M.; Crispin, X. Ionic Seebeck Effect in Conducting Polymers. *Adv. Energy Mater.* **2015**, *5* (11), 1–6. https://doi.org/10.1002/aenm.201500044.

(12) Rivnay, J.; Inal, S.; Collins, B. A.; Sessolo, M.; Stavrinidou, E.; Strakosas, X.; Tassone, C.; Delongchamp, D. M.; Malliaras, G. G. Structural Control of Mixed Ionic and Electronic Transport in Conducting Polymers. *Nat. Commun.* **2016**, *7*, 1–9. https://doi.org/10.1038/ncomms11287.

(13) Wieland, M.; Dingler, C.; Merkle, R.; Maier, J.; Ludwigs, S. Humidity-Controlled Water Uptake and Conductivities in Ion and Electron Mixed Conducting Polythiophene Films. *ACS Appl. Mater. Interfaces* **2020**, *12* (5), 6742–6751. https://doi.org/10.1021/acsami.9b21181.

(14) Huang, J.; Miller, P. F.; Wilson, J. S.; De Mello, A. J.; De Mello, J. C.; Bradley, D. D. C. Investigation of the Effects of Doping and Post-Deposition Treatments on the Conductivity, Morphology, and Work Function of Poly(3,4-Ethylenedioxythiophene)/Poly(Styrene Sulfonate) Films. *Adv. Funct. Mater.* **2005**, *15* (2), 290–296. https://doi.org/10.1002/adfm.200400073.

(15) Lang, U.; Naujoks, N.; Dual, J. Mechanical Characterization of PEDOT:PSS Thin Films. *Synth. Met.* **2009**, *159* (5–6), 473–479. https://doi.org/10.1016/j.synthmet.2008.11.005.

(16) *Conjugated Polyelectrolytes: Fundamentals and Applications*; Liu, B., Bazan, G. C., Eds.; John Wiley & Sons, 2013.

(17) Merkle, R.; Gutbrod, P.; Reinold, P.; Katzmaier, M.; Tkachov, R.; Maier, J.; Ludwigs, S. Mixed Conductivity of Polythiophene-Based Ionic Polymers under Controlled Conditions. *Polymer (Guildf).* **2017**, *132*, 216–226. https://doi.org/10.1016/j.polymer.2017.10.064.

(18) Huggins, R. A. Simple Method to Determine Electronic and Ionic Components of the Conductivity in Mixed Conductors a Review. *Ionics (Kiel).* **2002**, *8* (3–4), 300–313. https://doi.org/10.1007/BF02376083.

(19) Mai, C. K.; Zhou, H.; Zhang, Y.; Henson, Z. B.; Nguyen, T. Q.; Heeger, A. J.; Bazan, G. C. Facile Doping of Anionic Narrow-Band-Gap Conjugated Polyelectrolytes during Dialysis. *Angew. Chemie - Int. Ed.* **2013**, *52* (49), 12874–12878. https://doi.org/10.1002/anie.201307667.

(20) Mai, C. K.; Schlitz, R. A.; Su, G. M.; Spitzer, D.; Wang, X.; Fronk, S. L.; Cahill, D. G.; Chabinyc, M. L.; Bazan, G. C. Side-Chain Effects on the Conductivity, Morphology, and Thermoelectric Properties of Self-Doped Narrow-Band-Gap Conjugated Polyelectrolytes. *J. Am. Chem. Soc.* **2014**, *136* (39), 13478–13481. https://doi.org/10.1021/ja504284r.

(21) Mai, C.-K.; Arai, T.; Liu, X.; Fronk, S. L.; Su, G. M.; Segalman, R. A.; Chabinyc, M. L.; Bazan, G. C. Electrical Properties of Doped Conjugated Polyelectrolytes with Modulated Density of the Ionic Functionalities. *Chem. Commun.* **2015**, *51*, 1–4. https://doi.org/10.1039/C5CC06690E.

(22) Patel, S. N.; Javier, A. E.; Balsara, N. P. Electrochemically Oxidized Electronic and Ionic Conducting Nanostructured Block Copolymers for Lithium Battery Electrodes. *ACS Nano* **2013**, *7* (7), 6056–6068. https://doi.org/10.1021/nn4018685.

(23) Cao, D. X.; Leifert, D.; Brus, V. V.; Wong, M. S.; Phan, H.; Yurash, B.; Koch, N.; Bazan, G. C.; Nguyen, T. The Importance of Sulfonate to the Self-Doping Mechanism of the Water-Soluble Conjugated Polyelectrolyte PCPDTBT-SO 3 K. *Mater. Chem. Front.* **2020**. https://doi.org/10.1039/D0QM00073F.

(24) Mühlbacher, D.; Scharber, M.; Morana, M.; Zhu, Z.; Waller, D.; Gaudiana, R.; Brabec, C. High Photovoltaic Performance of a Low-Bandgap Polymer. *Adv. Mater.* **2006**, *18* (21), 2884–2889. https://doi.org/10.1002/adma.200600160.

(25) Soci, C.; Hwang, I. W.; Moses, D.; Zhu, Z.; Waller, D.; Gaudiana, R.; Brabec, C. J.; Heeger, A. J. Photoconductivity of a Low-Bandgap Conjugated Polymer. *Adv. Funct. Mater.* **2007**, *17* (4), 632–636. https://doi.org/10.1002/adfm.200600199.

(26) Beljonne, D.; Cornil, J.; Sirringhaus, H.; Brown, P. J.; Shkunov, M.; Friend, R. H.; Brédas, J. L. Optical Signature of Delocalized Polarons in Conjugated Polymers. *Adv. Funct. Mater.* **2001**, *11* (3), 229–234. https://doi.org/10.1002/1616-3028(200106)11:3<229::AID-ADFM229>3.0.CO;2-L.

(27) Ouyang, J.; Xu, Q.; Chu, C. W.; Yang, Y.; Li, G.; Shinar, J. On the Mechanism of Conductivity Enhancement in Poly(3,4- Ethylenedioxythiophene):Poly(Styrene Sulfonate) Film through Solvent Treatment. *Polymer (Guildf).* **2004**, *45* (25), 8443–8450. https://doi.org/10.1016/j.polymer.2004.10.001.

(28) Harima, Y.; Eguchi, T.; Yamashita, K.; Kojima, K.; Shiotani, M. In Situ ESR Study on Poly(3-Methylthiophene): Charge Transport Due to Polarons and Bipolarons before the Evolution of Metallic Conduction. *Synth. Met.* **1999**, *105* (2), 121–128. https://doi.org/10.1016/S0379-6779(99)00059-4.

(29) Lee, J. K.; You, S.; Jeon, S.; Ryu, N. H.; Park, K. H.; Myung-Hoon, K.; Kim, D. H.; Kim, S. H.; Schiff, E. A. Electron Spin Resonance and Electrical Transport in Films of Poly (3,4-Ethylenedioxythiophene) Doped with Poly(Styrenesulphonate). *J. Appl. Phys.* **2015**, *118* (1). https://doi.org/10.1063/1.4923416.

(30) Zykwinska, A.; Domagala, W.; Czardybon, A.; Pilawa, B.; Lapkowski, M. In Situ EPR Spectroelectrochemical Studies of Paramagnetic Centres in Poly(3,4-Ethylenedioxythiophene) (PEDOT) and Poly(3,4-Butylenedioxythiophene) (PBuDOT) Films. *Chem. Phys.* **2003**, *292* (1), 31–45. https://doi.org/10.1016/S0301-0104(03)00253-2.

(31) Tsokkou, D.; Peterhans, L.; Cao, D. X.; Mai, C.; Bazan, G. C.; Nguyen, T.; Banerji, N. Excited State Dynamics of a Self-Doped Conjugated Polyelectrolyte. **2020**, *1906148* (January). https://doi.org/10.1002/adfm.201906148.

(32) Wertz, J. E.; Bolton, J. R. *Electron Spin Resonance*; Springer Netherlands: Dordrecht, 1986. https://doi.org/10.1007/978-94-009-4075-8.

(33) Rivnay, J.; Mannsfeld, S. C. B.; Miller, C. E.; Salleo, A.; Toney, M. F. Quantitative Determination of Organic Semiconductor Microstructure from the Molecular to Device Scale. *Chem. Rev.* **2012**, *112*, 5488–5519. https://doi.org/10.1021/cr3001109 |.

(34) Niedzialek, D.; Lemaur, V.; Dudenko, D.; Shu, J.; Hansen, M. R.; Andreasen, J. W.; Pisula, W.; Müllen, K.; Cornil, J.; Beljonne, D. Probing the Relation between Charge

Transport and Supramolecular Organization down to Ångström Resolution in a Benzothiadiazole- Cyclopentadithiophene Copolymer. *Adv. Mater.* **2013**, *25* (13), 1939–1947. https://doi.org/10.1002/adma.201201058.

(35) la Cruz, D. S.; Green, M. D.; Ye, Y.; Elabd, Y. A.; Long, T. E.; Winey, K. I. Correlating Backbone-to-Backbone Distance to Ionic Conductivity in Amorphous Polymerized Ionic Liquids. *J. Polym. Sci. Part B Polym. Phys.* **2012**, *50* (5), 338–346. https://doi.org/10.1002/polb.23019.

(36) Nakamura, K.; Fukao, K.; Inoue, T. Dielectric Relaxation and Viscoelastic Behavior of Polymerized Ionic Liquids with Various Counteranions. *Macromolecules* **2012**, *45*, 3850–3858. https://doi.org/10.1021/ma300040b.

(37) Nakamura, K.; Fukao, K. Dielectric Relaxation Behavior of Polymerized Ionic Liquids with Various Charge Densities. *Polymer (Guildf).* **2013**, *54* (13), 3306–3313. https://doi.org/10.1016/j.polymer.2013.04.039.

(38) Sanoja, G. E.; Popere, B. C.; Beckingham, B. S.; Evans, C. M.; Lynd, N. A.; Segalman, R. A. Structure-Conductivity Relationships of Block Copolymer Membranes Based on Hydrated Protic Polymerized Ionic Liquids: Effect of Domain Spacing. *Macromolecules* **2016**, *49* (6), 2216–2223. https://doi.org/10.1021/acs.macromol.5b02614.

(39) Mostert, A. B.; Hanson, G. R.; Sarna, T.; Gentle, I. R.; Powell, B. J.; Meredith, P. Hydration-Controlled X - Band EPR Spectroscopy: A Tool for Unravelling the Complexities of the Solid-State Free Radical in Eumelanin. **2013**. https://doi.org/10.1021/jp401615e.

(40) Mostert, A. B.; Rienecker, S. B.; Noble, C.; Hanson, G. R.; Meredith, P. The Photoreactive Free Radical in Eumelanin. *Sci. Adv.* **2018**, *4* (3), 1–7. https://doi.org/10.1126/sciadv.aaq1293.

Chapter 4

Living Bioelectrochemical Composites

Composites, in which two or more material elements are combined to provide properties unattainable by single components, have a historical record dating to ancient times. Few have included a living microbial community as a key design element. A logical basis for enabling bioelectronic composites stems from the phenomenon that certain microorganisms transfer electrons to external surfaces, such as an electrode. A bioelectronic composite which allows one to address cells beyond the confines of an electrode surface can impact bioelectrochemical technologies, including microbial fuel cells for power production and bioelectrosynthesis platforms where microbes produce desired chemicals. We show that the conjugated polyelectrolyte CPE-K functions as a conductive matrix to electronically connect a three-dimensional network of *Shewanella oneidensis* MR-1 to a gold electrode, thereby increasing biocurrent ~150-fold over control biofilms. These biocomposites spontaneously assemble from solution into an intricate arrangement of cells within a conductive polymer matrix. While increased biocurrent is due to more cells in communication with the electrode, current extracted per cell is also enhanced indicating efficient long-range electron transport. Further, biocomposites show almost an order-of-magnitude lower charge transfer resistance

than CPE-K alone, supporting that the electroactive bacteria and the conjugated polyelectrolyte work synergistically towards an effective bioelectronic composite.

4.1 Introduction

Certain anaerobic bacteria can interface with electrodes to catalyze the interconversion of chemical and electrical energy. Indeed, a series of bioelectrochemical systems (BESs) based on microbial electroactivity has been developed. Such technologies include microbial fuel cells (MFCs) that produce electricity from the oxidation of organic and inorganic compounds, applicable for wastewater remediation, desalination, and the removal of toxic chemicals from the environment.[1–4] Conversely, electrical current can also drive microbial metabolism in bioelectrosynthesis platforms to produce desired chemicals, while other configurations allow for electrochemical production of hydrogen or methane gas.[5,6] In all of these systems, energy transduction is achieved by microbial colonization of an electrode and electron transfer to/from electrode surfaces.

However, inefficient interfacial contacts pose a primary bottleneck for electron transfer throughout the range of BES technologies.[7–9] Substantial efforts thus are centered on seeking enhancements through engineering of device configurations and electrode surfaces, for example the introduction of interfacial agents.[7,10,11] Electrodes with greater dimensionality have the advantage of larger specific surface areas for increased microbial loading.[12–14] Monolithic three-dimensional (3D) electrodes with porous structures have been used, including reticulated vitreous carbon, metal oxide foams, and sponges with conductive coatings; however, biofilms must conform to their structure and clogging can occur.[15–17]

An alternative strategy to 3D integration is via formation of bacteria/soft conductive material composites in which the conductive matrix and biofilm formation are

spontaneously organized.[18,19] Desirable properties of the soft host matrix include conductivity in aqueous media, tunable optoelectronic properties, biocompatibility, diffusion of nutrients/waste, ease of assembly, and shape-adaptability to conform within different device configurations. Literature examples fall into two groups: immobilizing bacteria with conductive materials before BES operation or developing a bacteria/conductive material hybridized biofilm through self-assembly. For instance, polypyrrole and PEDOT:PSS were electropolymerized with *S. oneidensis* MR-1 to create thicker biofilms with greater electronic connectivity with the electrode.[20,21] *S. oneidensis* MR-1 has also been encapsulated in a phospholipid hydrogel functionalized with ferrocene, which allowed extracellular electrons to hop via redox-reactions to the electrode.[22] In other approaches, *S. oneidensis* MR-1 and environmental samples were combined with graphene oxide on electrodes to create hybridized biofilms that increased current generation through increased biomass and electroactive surface area.[23,24]

The self-p-doped conjugated polyelectrolyte CPE-K (**Figure 4.1a**), initially used in optoelectronic devices, can meet all of the requirements to function as the conductive synthetic element in a 3D abiotic/biotic composite.[25,26] CPE-K was previously reported to accept electrons and increase biocurrent output from a single layer of *S. oneidensis* MR-1 atop carbon felt electrodes by a factor of ~3-fold.[27] This enhancement was due to increasing electron transfer at the electrode interface through redox-cycling of the CPE-K and an increase in surface cell density.[27] Moreover, CPE-K was independently found to assemble into a hierarchical hydrogel structure held together primarily via ionic-cross-links (**Figure 4.1b**).[28] Based on the combination of these properties, we disclose here a 3D living material produced by combining CPE-K and *S. oneidensis* MR-1. **Figure 4.1c** illustrates a vison of

this composite in which living cells play a bifunctional role of tailoring the composite structure and charge generation capacity. Indeed, as disclosed herein, the 3D living composite enables efficient interfacial coupling, resulting in current density amplification by ~150-fold.

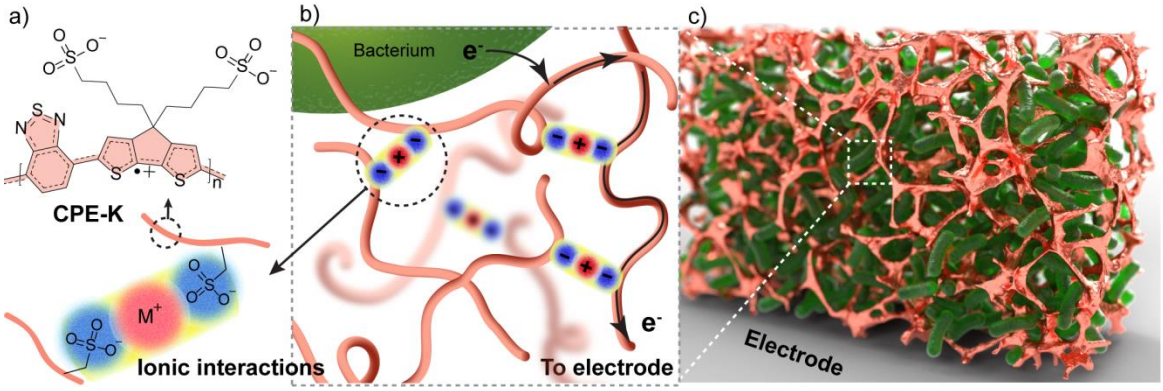

Figure 4.1: Bioelectronic composite concept. a) The molecular structure of CPE-K is shown with a polaron (radical cation) in its backbone. CPE-K is expected to form a hydrogel via ionic interactions. b) Metabolic electrons are transferred extracellularly to the matrix made of conductive CPE-K polymer chains. c) A cartoon representation of a conductive matrix (metallic color) encapsulating electroactive bacteria (green).

4.2 Biocompatibility

Before testing the electrochemical properties of the composites, the toxicity of CPE-K towards *S. oneidensis* MR-1 was investigated. Previous studies of CPE-K show low antimicrobial activity towards *Escherichia coli* due to low binding affinity, with the highest concentration tested being 0.2 mg mL^{-1} CPE-K.[29] To test whether the polymer was toxic toward *S. oneidensis* MR-1 at higher concentrations, biocomposites first were obtained by simply adding appropriate volumes of liquid culture to pre-weighed solid CPE-K followed by vortexing at low speeds to mix. After 18 hours incubation, bacterial survival rates were

determined through traditional agar plate colony-forming-unit counting. Testing revealed no toxic effect by CPE-K on *S. oneidensis* MR-1 up to the highest concentration tested (20 mg mL^{-1} CPE-K), see **Figure 4.S1**. Furthermore, there was no inhibition of growth compared to control cultures. Indeed, we found that the highest CPE-K concentration tested (20 mg mL^{-1}) increased cell growth 50 ± 27% over the controls. Biocompatibility was also confirmed through live/dead staining of a biocomposite after 24 hours incubation as shown in **Figure 4.2**, where all cells are stained with 4,6-diamidino-2-phenylindole (DAPI, blue), while dead cells are also stained with propidium iodide (PI, red). Assessment via confocal laser scanning microscopy (CLSM) gives a positive evaluation of bacteria health, with approximately 9% dead cells.

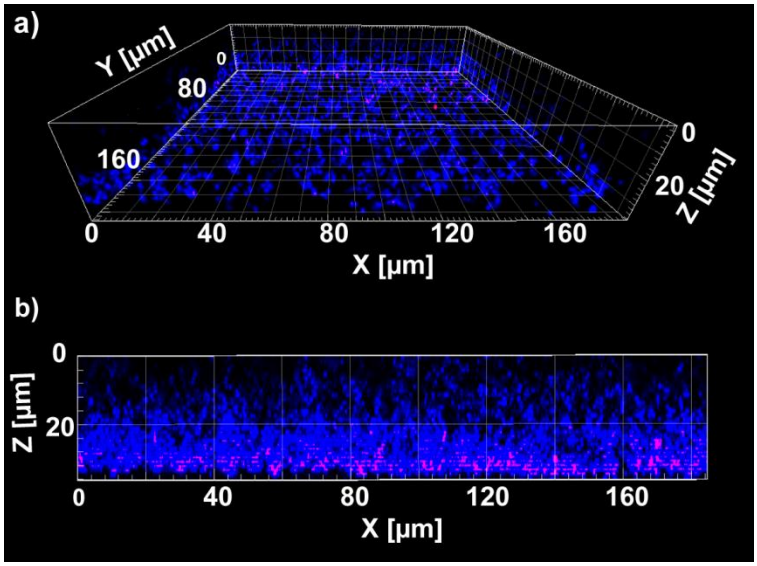

Figure 4.2: Bioelectronic initial biocompatibility testing. CLSM images of a 10 mg mL^{-1} CPE-K and *S. oneidensis* MR-1 composite stained with DAPI (blue, all cells) and PI (red, dead cells) after 24 hours anaerobic incubation. a) 3D view and b) profile view.

4.3 Current Generation of Composites

Microbial three-electrode electrochemical cells (M3Cs) were used to test the current generating properties of biocomposites by measuring chronoamperometry (CA) at a specified applied electrode potential (E_{CA}) against a reference electrode.[30–33] In *S. oneidensis* MR-1, the characteristic redox-potentials of flavin-based mediated electron transfer (MET, -0.4 V to -0.3 V vs Ag/AgCl) and membrane-protein direct electron transfer (DET, 0 V vs Ag/AgCl) to electrodes are well established.[30,34–37] Because CPE-K (M_n = 6638 g mol^{-1}) is expected to form a network by labile non-covalent interactions, a dialysis membrane (3.5 kD MWCO) was used to confine the polymer and the cells inside a well above the gold working electrode (area = 2 cm^2, depth = 247 μm ± 5). The main M3C chamber was kept sterile and contained a reservoir of 40 mM lactate in M1 growth media. Please see **Figure 4.S2** for a device schematic and the Supporting Information for full experimental details on device assembly.

Current generation by *S. oneidensis* MR-1 was tested independently before investigating the performance of the biocomposites. Stationary cultures of 0.15 OD_{600} *S. oneidensis* MR-1 (1.0 OD_{600} = 1.0 × 10^9 cells mL^{-1}) were added to working electrode wells. Similar control tests were carried out for different concentrations of CPE-K. **Figure 4.3** shows the average biocurrent density (J) over time at E_{CA} = 0.3 V vs Ag/AgCl for controls and biocomposites. The E_{CA} value was chosen to stimulate extracellular electron transport mechanisms of the bacteria, while encompassing the oxidation potential of CPE-K (0.27 V vs Ag/AgCl).[27] Control biofilms reached a maximum of J = 7 ± 3 mA m^{-2} after 6 hours and declined to J = 1.3 ± 0.4 mA m^{-2} after 7 days of operation. This current density is similar in magnitude to other *Shewanella* biofilms atop gold electrodes.[38,39] For the negative control 20 mg mL^{-1}

CPE-K, J = 1.2 ± 1.0 mA m^{-2} after 7 days. Negative controls of 5 and 10 mg mL^{-1} CPE-K concentrations showed similarly low currents (0.7 ± 0.7 mA m^{-2} and 0.7 ± 2.0 mA m^{-2}, respectively). These controls provide the basis to evaluate the performance of biocomposites, as described below.

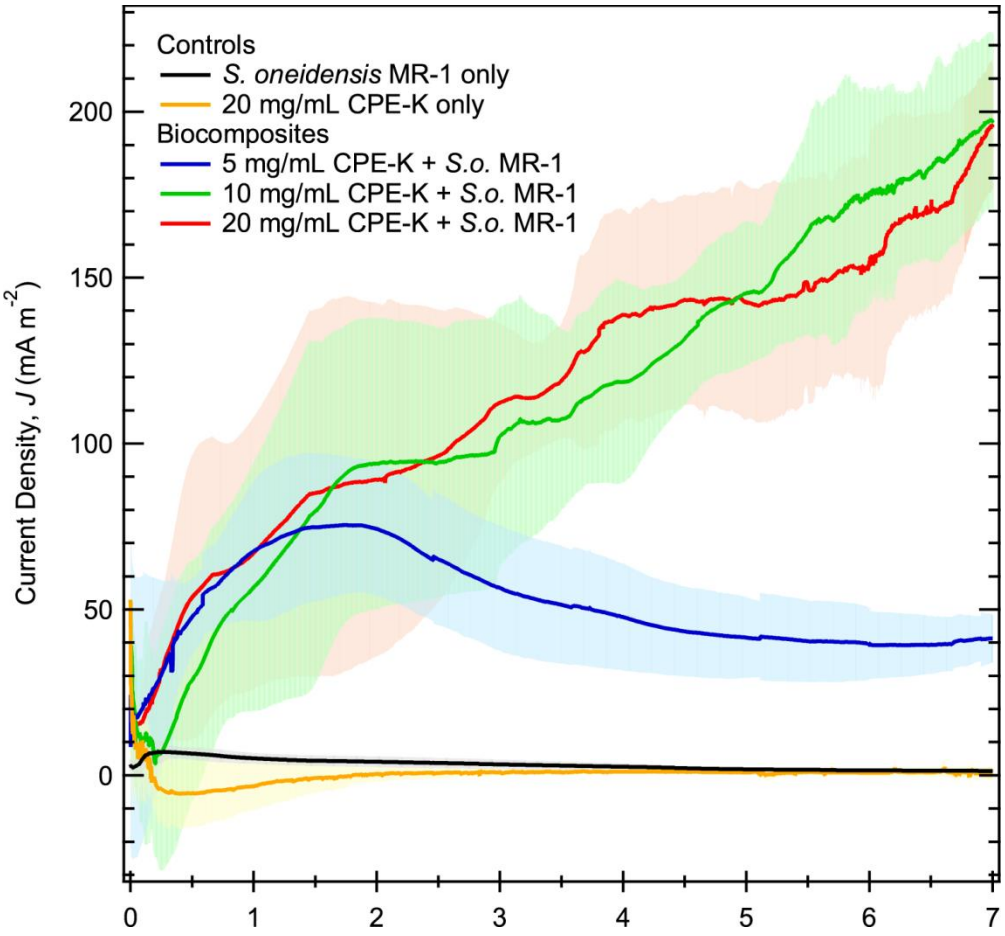

Figure 4.3: Average current density as a function of time (chronoamperometry, CA) for controls and biocomposites. Controls are S. oneidensis MR-1 only and 20 mg mL-1 CPE-K only. Biocomposite concentrations tested with S. oneidensis MR-1 include 5, 10, and 20 mg mL-1 CPE-K. Electrochemical cells were poised at 0.3 V vs Ag/AgCl and used 40 mM lactate as the carbon source. Light colored bands indicate the standard deviation in current ($n \geq 3$).

Biocomposites were prepared with 5, 10, and 20 mg mL^{-1} CPE-K with the same initial *S. oneidensis* MR-1 loading of 0.15 OD_{600}. In the case of the 5 mg mL^{-1} CPE-K biocomposites, *J* began at ~20 mA m^{-2} and peaked after ~1.8 days at 75 ± 20 mA m^{-2}. Current generation decreased gradually for ~3 more days and subsequently maintained a steady-state, with *J* = 41 ± 7 mA m^{-2} at the end of 7 days. This is a ~30-fold increase over the controls. Biocomposites with 10 and 20 mg mL^{-1} CPE-K showed a similar rise in current over time compared to the 5 mg mL^{-1} counterparts; however the current did not peak and instead continued to increase over the 7 days of operation. Both the 10 and 20 mg mL^{-1} CPE-K biocomposites reached similar *J* values of 198 ± 17 mA m^{-2} and 196 ± 20 mA m^{-2} after 7 days, respectively. These values represent a ~150-fold increase in average current density over the controls.

4.4 Composite Morphology and Current per Cell

Working electrode surfaces were imaged after biocurrent testing to examine the organizational relationships between the cells and CPE-K in the composites, see **Figure 4.4**. From the scanning electron microscopy (SEM) image obtained of the control containing only *S. oneidensis* MR-1 (Figure 4.4a) one observes a sparse monolayer biofilm on the electrode surface. The 5 mg mL^{-1} CPE-K biocomposite (Figure 4.4c) exhibits a higher density of cells on the electrode surface, together with polymeric material. The appearances of the 10 and 20 mg mL^{-1} CPE-K biocomposites are similar to each other; from Figure 4.4d and 4.S3, one observes the presence of both cells and CPE-K, which appears as sheet-like structures. It is worth noting that the appearance of the polymer is more condensed in the 20 mg mL^{-1} CPE-K sterile control relative to biocomposites, see Figure 4.4b. Cross-sectional views of the 20 mg mL^{-1} biocomposite (Figure 4.4e) show that cells reside not only on the

top surface, but are also well interspersed throughout the volume of the composite. Live/dead staining performed at the end of current collection shows few dead cells (red) during confocal microscopy, see **Figure 4.5**. It is worth noting that the DAPI dye not only accumulated in the cells, but also associated with what looks like CPE-K polymer sheets with similar structures to what is seen by SEM characterization.

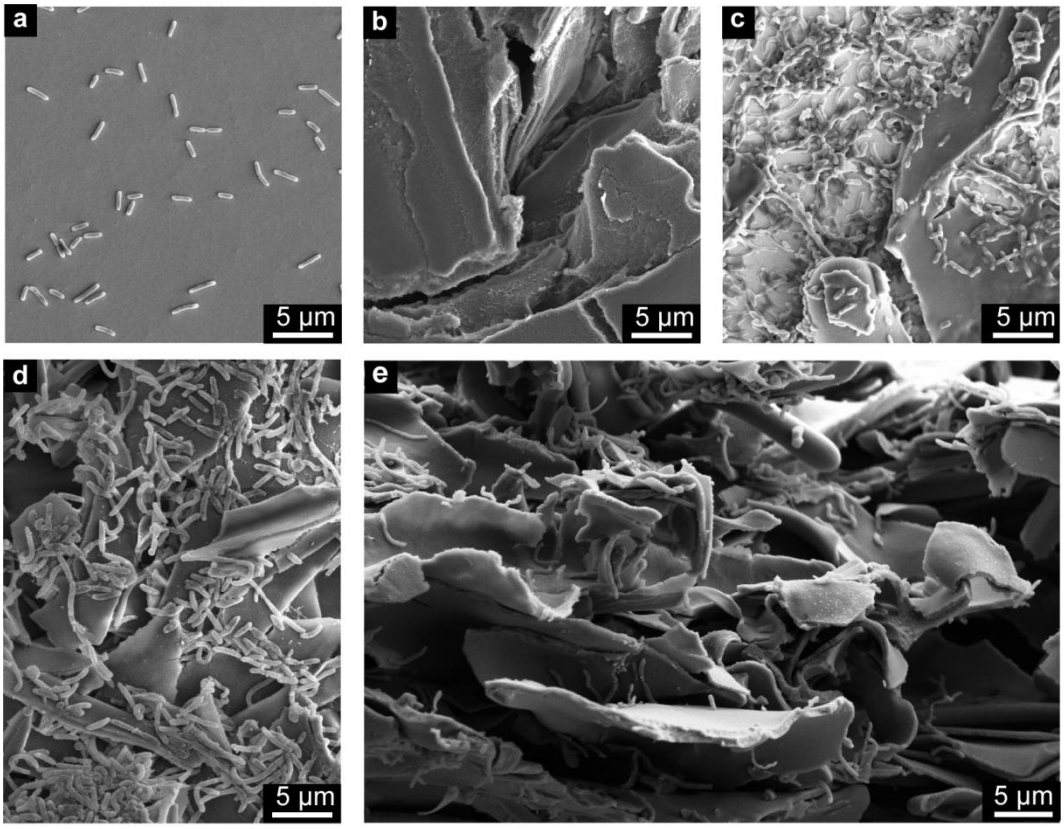

Figure 4.4: Representative SEM images after 7 days of CA current collection for a) S. oneidensis MR-1 only, b) 20 mg mL-1 CPE-K only, c) 5 mg mL-1 CPE-K biocomposite, and d) 20 mg mL-1 CPE-K biocomposite with e) a cross-sectional view of the 20 mg mL-1 biocomposite.

The number of living cells was quantified immediately after electrochemical characterization was complete at the end of 7 days. The current per cell was then determined by dividing the current at the end of CA over the number of cells (see **Table 4.1**). From this

analysis one finds that current output per cell is similar for the 5 mg mL^{-1} CPE-K biocomposites (78 ± 8 fA) and the control *S. oneidensis* MR-1 biofilms (66 ± 12 fA). The current generation per cell for the 10 and 20 mg mL^{-1} CPE-K biocomposites are almost double with 152 ± 26 fA and 188 ± 11 fA, respectively. Higher loadings of CPE-K thus leads to a higher cell density and a more efficient charge extraction per cell, the latter being consistent with the CPE-K matrix being intimately involved in long-range electron transfer to the electrode surface.

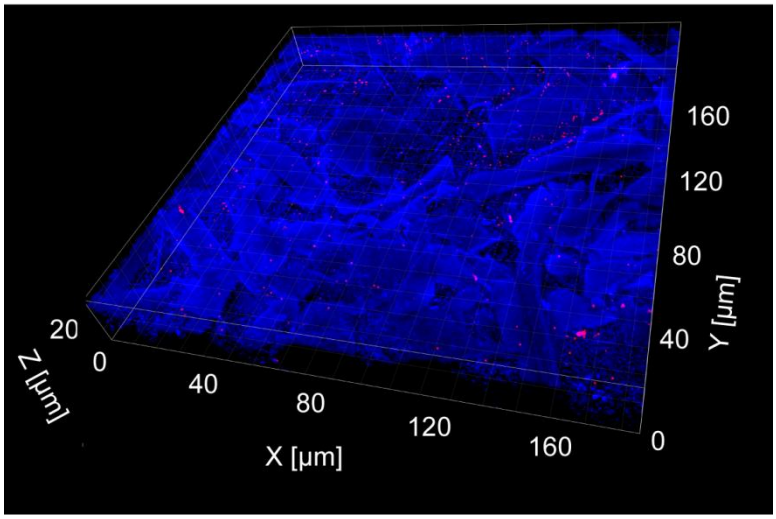

Figure 4.5: Representative CSLM image after 7 days of CA current collection for 20 mg mL^{-1} CPE-K biocomposite stained with DAPI (blue, all cells and polymer) and PI (red, dead cells).

Table 4.1: Bioelectrochemical parameters from M3Cs after 7 days of CA current collection from controls and biocomposites.[a)]

Biocomposites with *S. oneidensis* MR-1	Average Current Density, J [mA m^{-2}]	Number of Cells, X [*10^8]	Current per cell,[b)] I_{cell} [fA $cell^{-1}$]
5 mg mL^{-1} CPE-K	41 ± 7	1.1 ± 0.2	78 ± 8
10 mg mL^{-1} CPE-K	198 ± 17	2.6 ± 0.5	152 ± 26
20 mg mL^{-1} CPE-K	196 ± 20	2.1 ± 0.2	188 ± 11
Control			
S. oneidensis MR-1 only	1.3 ± 0.4	0.04 ± 0.01	66 ± 12

[a)]Errors represent standard deviations from the mean (n ≥ 3); [b)]Current per cell calculated as $I_{cell} = J*A/X$, where A is the area of the gold electrode (2 cm^2).

4.5 Evaluation of the Conductive Network

Cyclic voltammetry (CV) and electrochemical impedance spectroscopy (EIS) were performed after 7 days of CA collection to further investigate the mechanisms of current generation enhancement. For CV, see **Figure 4.6**, a potential sweep window of -0.6 V to 0.45 V was chosen to encompass expected redox processes of the system with respect to the Ag/AgCl (saturated KCl) reference electrode: MET and DET in *S. oneidensis* MR-1, and oxidation of CPE-K (0.27 V). No detectable signal is seen for MET for all conditions, which we attribute to diffusion of mediators out of the electrode well (~50 µL volume) through the dialysis membrane and into the M3C reservoir (15 mL volume). Catalytic DET through membrane proteins is observed for the control biofilms with the oxidation at ~0 V. Sterile controls of CPE-K at 5, 10, and 20 mg mL^{-1}, provided for reference, only show oxidation of the polymer at E > 200 mV, see Figure 4.6 dashed lines. A combination of these two features is seen in the CV scan of the 5 mg mL^{-1} CPE-K biocomposite.

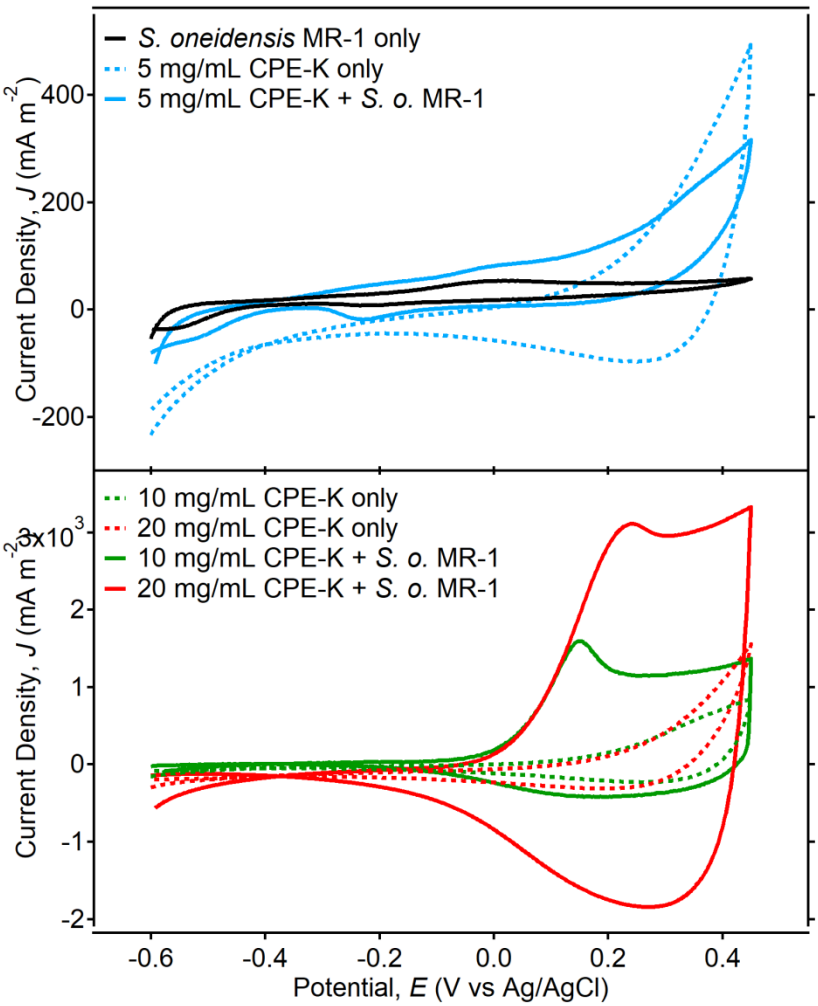

Figure 4.6: Representative cyclic voltammetry (CV) data after 7 days of CA current collection. a) CV of *S. oneidensis* MR-1 only, 5 mg mL^{-1} CPE-K only, and 5 mg mL^{-1} CPE-K biocomposite. b) CV of *S. oneidensis* MR-1 only, 10 and 20 mg mL^{-1} CPE-K controls and biocomposites. (scan rate 5 mV s^{-1}).

Most significantly, CV measurements of the 10 and 20 mg mL^{-1} CPE-K biocomposites exhibit substantially higher current densities, in line with the CA data, and unexpectedly shaped curves. While the CV of the 5 mg mL^{-1} CPE-K biocomposites show quasi reversible redox peaks, indicating a diffusion-limited process, the 10 and 20 mg mL^{-1} CPE-K biocomposites show rectangular-shaped waves reminiscent of the characteristics of pseudocapacitors.[40–42] We attribute the presence of pseudocapacitive behavior upon higher

CPE-K loading to a matrix with more continuous interchain contacts that improves electron transport.

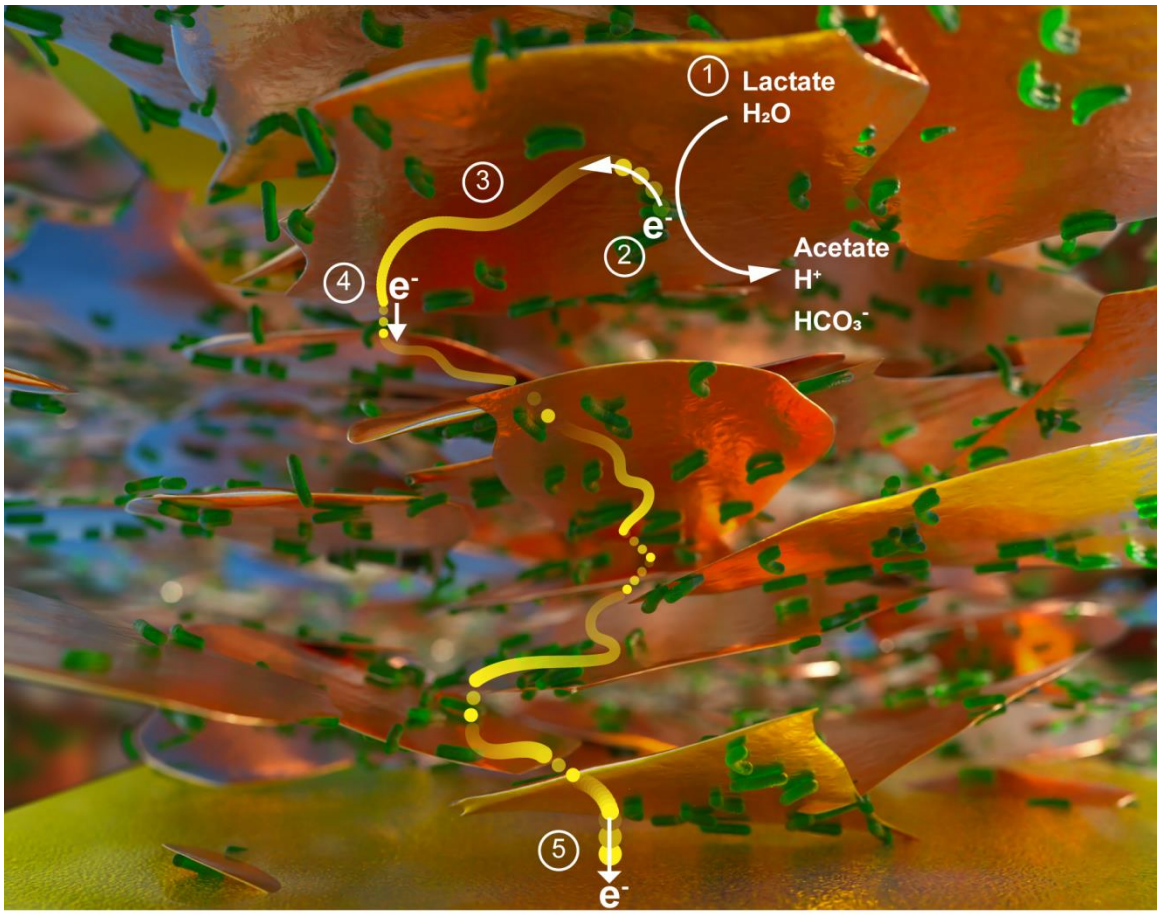

Figure 4.7: Proposed biocomposite charge generation scheme. 1) *S. oneidensis* MR-1 bacteria (green) generate metabolic electrons from the catalytic conversion of lactate to acetate and other products. 2) Electron equivalents are transferred to CPE-K sheets (orange) from bacteria via membrane proteins. 3) Charges conduct along the CPE-K sheet. 4) Charges transfer between sheets. Steps 3 and 4 repeat until 5) charges are collected at the gold electrode.

Of particular interest is the redox peak seen between 100 mV and 300 mV in the CV traces of the more concentrated biocomposites (Figure 4.6b). We surmise that the peak is from the oxidation of the membrane proteins of *S. oneidensis* MR-1. This DET peak is

shifted from its potential in the control biofilms and 5 mg mL^{-1} CPE-K biocomposites, presumably due to the variable resistance of the CPE-K network. Specifically, at ~0 V, oxidation of the membrane proteins occurs in the control biofilm, but in the networked-biocomposite the encapsulated cells can not be accessed because the CPE-K matrix is not as conductive at this potential. CPE-K is oxidized as the potential is swept to more positive values thereby providing a pathway to membrane-protein oxidation. **Figure 4.7** presents a schematic of this charge transfer process through the bioelectronic composite.

An ideal bioelectronic composite would have low charge transfer resistance (R_{CT}) at the abiotic/biotic interface to efficiently collect current. We thus performed EIS at 300 mV, see **Figure 4.8**. Apart from the positive control (Figure 4.8a), the Nyquist plots consist of a classical semicircle representing the resistance to charge transfer, followed by a linear response at low frequencies. The Supporting Information provides further details on the recording and analysis of the EIS data. Based on the semicircle diameter, the average R_{CT} for the 10 and 20 mg mL^{-1} CPE-K biocomposite conditions is 50 ± 20 Ω and 40 ± 20 Ω, respectively (Figure 4.8d), which is considerably smaller than what is calculated for the sterile 5, 10, and 20 mg mL^{-1} CPE-K (480 ± 20 Ω, 410 ± 60 Ω, and 150 ± 20 Ω, respectively) and 5 mg mL^{-1} CPE-K biocomposite (700 ± 50 Ω), as seen in Figure 4.8b and 4.8c. The linear response at low frequencies also transitions from a ~45˚ angle to a more vertical orientation, signifying a shift from slow mass transport of ions to the electrode surface to better capacitive behavior by way of the conducting matrix in the 10 and 20 mg mL^{-1} CPE-K biocomposites.[41,43] That the biocomposites have a lower charge transfer resistance and more capacitive behavior than the sterile polymer controls suggests that the presence of the *S. oneidensis* MR-1 improves the electronic properties of the polymer

matrix. The further improved electronic properties of the CPE-K may in turn be responsible for the increased current per cell seen in chronoamperometry (see Table 4.1). Taken as a whole, these results reveal a synergistic action of the two components in the biocomposite towards optimizing the biotic/abiotic interface at the charge collecting electrode.

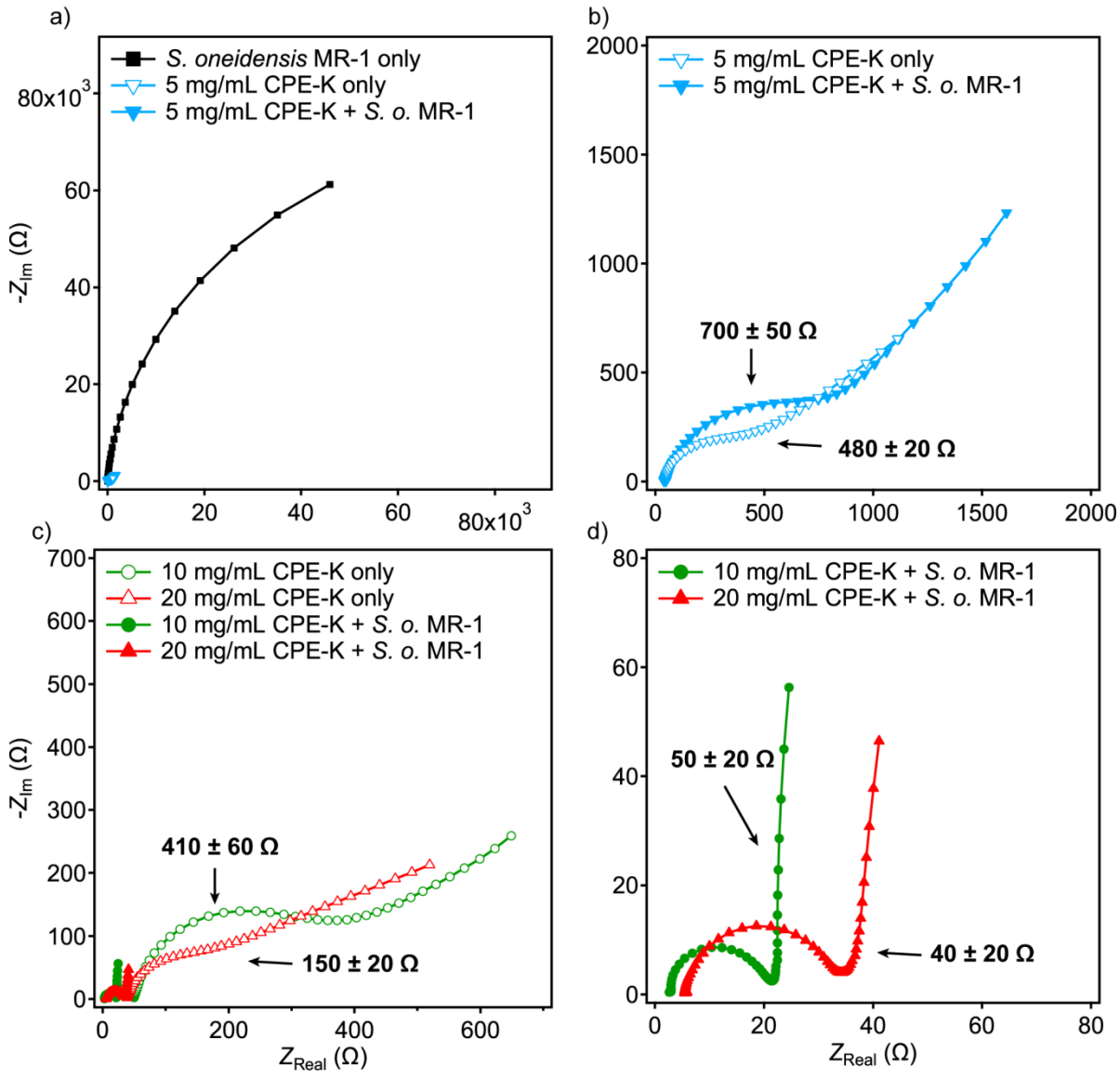

Figure 4.8: Representative electrochemical impedance spectroscopy (EIS) data after 7 days of CA current collection. Nyquist curves of a) *S. oneidensis* MR-1 only, 5 mg mL^{-1} CPE-K only, and 5 mg mL^{-1} CPE-K biocomposite and b) the enlarged Nyquist curves of the 5 mg mL^{-1} CPE-K control and biocomposite. Nyquist

curves of c) 10 and 20 mg mL^{-1} CPE-K controls and biocomposites with d) the enlarged Nyquist curves of the 10 and 20 mg mL^{-1} CPE-K biocomposites. Annotated values represent the average charge transfer resistance and standard deviation ($n \geq 3$).

4.6 Conclusion

To summarize, a new 3D living composite material can be obtained by the simple combination of CPE-K, a self-p-doped conjugated polyelectrolyte, and the electroactive bacteria *S. oneidensis* MR-1. The bioelectronic composite is an effective way to significantly increase biocurrent density, which originates from increasing the number of microbes in electronic communication with the charge-collecting electrode through the conductive CPE-K matrix. The one-step assembly of these composites therefore offers a simple and effective route to improve the performance of BESs such as microbial fuel cells and bioelectrosynthesis platforms. Opportunities also exist to apply this living material to environmental sensing applications and fundamental investigations of electronic communication within microbial communities. The bacteria and CPE-K have a synergistic relationship in which the 3D framework promotes microbial respiration (both increased number of microbes and increased current per cell) and in turn the bacteria influence the formation of the conducting matrix. Specifically, the biocomposites have a more continuous and conductive network than controls of polymer only, as evidenced by their pseudo-capacitive behavior and lower charge transfer resistance. This work suggests that living organisms can be synergistically integrated with synthetic systems to create fundamentally new advanced materials, bridging the gap between microbiology and the vast repertoire of materials previously developed for plastic electronics.

4.7 Materials, Methods, & Supplementary Figures

4.7.1 Materials & Methods

Materials: All chemicals were purchased from Fisher Scientific or Sigma Aldrich and used as received unless otherwise indicated. CPE-K was synthesized according to literature procedures.[44] The molecular weight of CPE-K was determined by GPC of the tetrabutylammonium congener. GPC (DMF): M_n = 6638, M_w = 21434, *PDI* = 3.22.

Cell culture and growth medium: *Shewanella oneidensis* MR-1 (ATCC 700550) was struck out on LB agar plates from frozen bacterial stock and incubated at 30 °C to isolate single colonies. Liquid cultures were grown by selecting morphologically similar colonies with a sterile loop to inoculate anaerobic modified M1 medium containing 20 mM Na-(L)-lactate as electron donor and 20 mM Na-fumarate as electron acceptor. After 24 hours incubation at 30 °C with shaking at 120 rpm, cultures consistently reach a maximum OD_{600} of ~0.22 (or 2.2×10^8 cfu mL^{-1}). These stationary phase cultures are then centrifuged, washed, and then re-suspended in fresh M1 media to a final concentration of 0.15 OD_{600}. M1 media is a defined media with the following composition per liter: 3 g HEPES buffer, 0.225 g potassium phosphate monobasic, 0.225 g potassium phosphate dibasic, 0.225 g ammonium sulphate, 0.46 g ammonium chloride, 0.117 g magnesium sulphate heptahydrate, 0.5 g cassamino acids, 10 mL DL vitamin mix, 10 mL Wolfe's mineral mix.

Biocompatibility through minimum bactericidal concentration testing (MBC)[45]: Various concentrations of CPE-K in M1 growth media with 20 mM Na-(L)-lactate and 40 mM Na-fumarate were inoculated with *S. oneidensis* MR-1 and incubated anaerobically for 18 hours. Because CPE-K absorbs at 600 nm – the standard wavelength at which cell growth is

measured in solution – samples were instead diluted and plated on LB agar plates. The number of colonies were counted and the results are summarized in Figure 4.S1.

Working electrode fabrication: Heavily doped (ρ = 0.001-0.005 Ω cm) p^+ (boron) silicon wafers were obtained from Addison Engineering Inc. The metal electrode in the silicon well was defined by soft lithography (PDMS mask), anisotropic plasma etching (Plasma-Therm DSEIII), and subsequent electron-beam evaporation of Ti (5 nm) and Au (70 nm). The depth of the Si well (247 ± 5 μm) was characterized by profilometery and SEM cross-sections. For electrode fabrication, ohmic contact to the device chip was made by rubbing Ga-In eutectic on its posterior. Then the chip was fixed to Ti foil with carbon tape, providing a point of contact for electrical leads. Immediately before use in M3Cs, electrodes were treated with UV/ozone to make the surface hydrophilic.

Working electrode well loading: For each test condition (sterile controls, bacteria-only controls, and biocomposites), solutions were made using 10 mM lactate with 20% glycerol in M1 media. To test different concentrations of CPE-K, the appropriate amount liquid culture or sterile solution was mixed with pre-weighed CPE-K and vortexed. Solutions were transferred into the working electrode well via pipette. In order to precisely control the assembly process, working electrodes were adhered to the M3C bottom lid, placed in an -80 ˚C freezer for 5 minutes, and then quickly sandwiched with the dialysis membrane, sealing O-ring, and M3C chamber. It is important to note that the dialysis membrane confines the bacteria and CPE-K in the working electrode well.

Microbial three-electrode electrochemical cells (M3Cs): Single-chambered M3Cs were fabricated out of acrylic to have a 15 mL working volume and were sealed with silicone O-rings. Reference electrode: Ag/AgCl (saturated KCl) with 3.2 mm Vycor frit (Gamry).

Counter electrode: coiled 0.25 mm Ti wire (Aldrich), 10 turns. Membrane: regenerated cellulose dialysis membrane, 3.5 kD molecular weight cut-off (Repligen/Spectrum Laboratories). The M3C chamber was kept as a sterile reservoir of 40 mM lactate in M1 media. Anaerobic conditions were maintained through constant headspace degassing with humidified, deoxygenated N_2. Temperature was kept at 30 °C by housing the M3Cs in a temperature regulated incubator.

Chronoamperometry (CA): Using a Gamry potentiostat (Reference 600, Series G 300, or Interface 1000 E models) and multiplexer (model ECM8), gold working electrode wells were poised at E_{CA} = 0.3 V vs Ag/AgCl to serve as the sole terminal electron acceptor for bacteria. M3Cs wells were inoculated (see above) and incubated in the dark 7 days total to measure current responses. The current response was measured, recorded, and averaged for 20-second blocks (at 160 second intervals) with Gamry software (Framework Version 6.11, Build 2227, 2013).

Cyclic voltammetry (CV): Electrochemical characterization with CV was undertaken at the end of 7 days CA operation to characterize the CPE-K-bacteria-electrode interactions. For these experiments, the working electrode potential was swept from $E_{initial}$ = –0.6 V to E_{vertex} = 0.45 V and back to E_{final} = –0.6 V at a scan rate of 0.005 V/s.

Electrochemical impedance spectroscopy (EIS): Electrochemical characterization with EIS was undertaken at the end of operation to characterize the CPE-K-bacteria-electrode interactions. For these experiments, the working electrode potential was poised at E_{DC} = 0.3 V vs Ag/AgCl and a sinusoidal potential with amplitude E_{AC} = 5 mV vs Ag/AgCl was applied starting from a frequency of 100 kHz to 100 mHz.

EIS spectra were fit to the simplest appropriate equivalent circuit models using Bio-logic EC-Lab software to estimate charge transfer resistance, R_{CT}. The intersection of the Nyquist curve at the Z_{Real} axis in the high-frequency range represents the solution resistance, R_S. The semicircle at high frequency can be modeled with a parallel combination of geometrical capacitance (Q_{geom}) and charge transfer resistance (R_{CT}). To fit spectra with a ~45˚ linear response at low frequencies, an additional circuit element called Warburg impedance, *W*, is added in series. This gives the simplest equivalent circuit $R_S + (Q_{geom}/R_{CT}) + W$. For EIS data with a more vertical linear response at low frequencies, an interfacial capacitance (Q_{int}) is used in place of the Warburg element, giving the equivalent circuit $R_S + (Q_{geo}/R_{CT}) + Q_{int}$. In all cases a constant phase element "*Q*" is used in place of a pure capacitor element to represent the deviation from an ideal capacitor.

Biomass quantification: Electrodes were removed from the M3Cs and placed in 50 mL centrifuge tubes with M1 media. Electrodes were gently agitated with vortexing and pipetting to facilitate dissolution of the biocomposites/biofilms into the media. Suspended cells were then diluted 25 to 1000 more times and 50 µL was plated on LB agar plates. Colonies were counted after incubating the plates at 30 ˚C for 24 hours.

Confocal microscopy (CLSM): Live/dead staining of cells was performed with 5 µM propidium iodide (10 minutes) and 10 µM DAPI (20 minutes), with 10 minutes rinsing in between each stain. Using a Leica SP8 Resonant Scanning Confocal microscope and 63x oil or glycerol objective, the dyes were exited sequentially and detected using HyD detectors. Images were processed using Imaris Measurement Pro software.

Scanning electron microscopy (SEM): After bioelectrochemical experiments, media in the M3C chambers was exchanged with 4% glutaraldehyde in fresh M1 media to chemically

fix electrode-associated cells for 24 hours. After fixation, electrodes were sequentially rinsed by exchanging the chamber media with the following solutions twice each: M1 media (1.5 hours), deionized water (1.5 hours), 35% ethanol in deionized water (1.5 hours), 70% ethanol in deionized water (1.5 hours), 100% ethanol (overnight). M3Cs were then dis-assembled and working electrodes dried via CO_2 critical point drying. Working electrodes were then sputtered with gold (Anatech Hummer Sputtering System) before imaging with an FEI Nova Nano 650 FEG SEM or ThermoFisher Apreo C LoVac FEG SEM. Accelerating voltage: 5 keV, working distance: ~10 mm, stage current: 50 pA, secondary electron detector.

4.7.2 Supplementary Figures

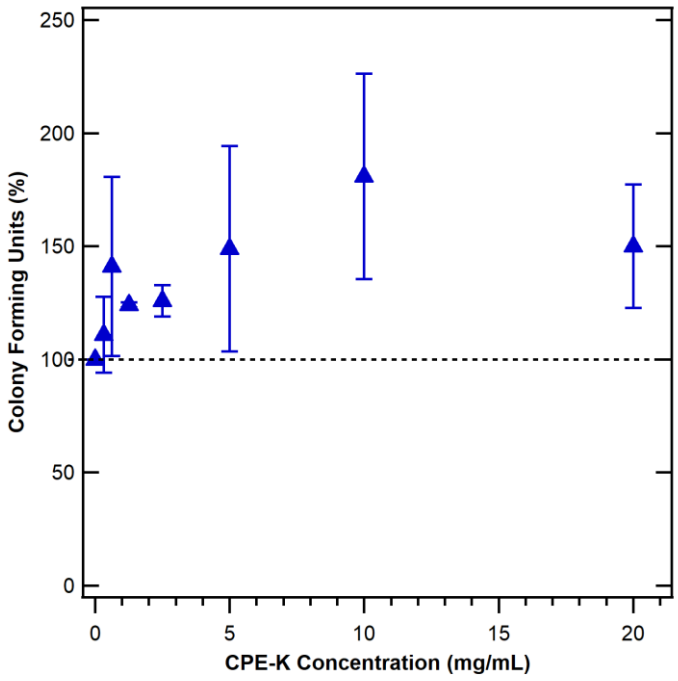

Figure 4.S1: Minimum bactericidal concentration (MBC) testing of CPE-K towards *S. oneidensis* MR-1.

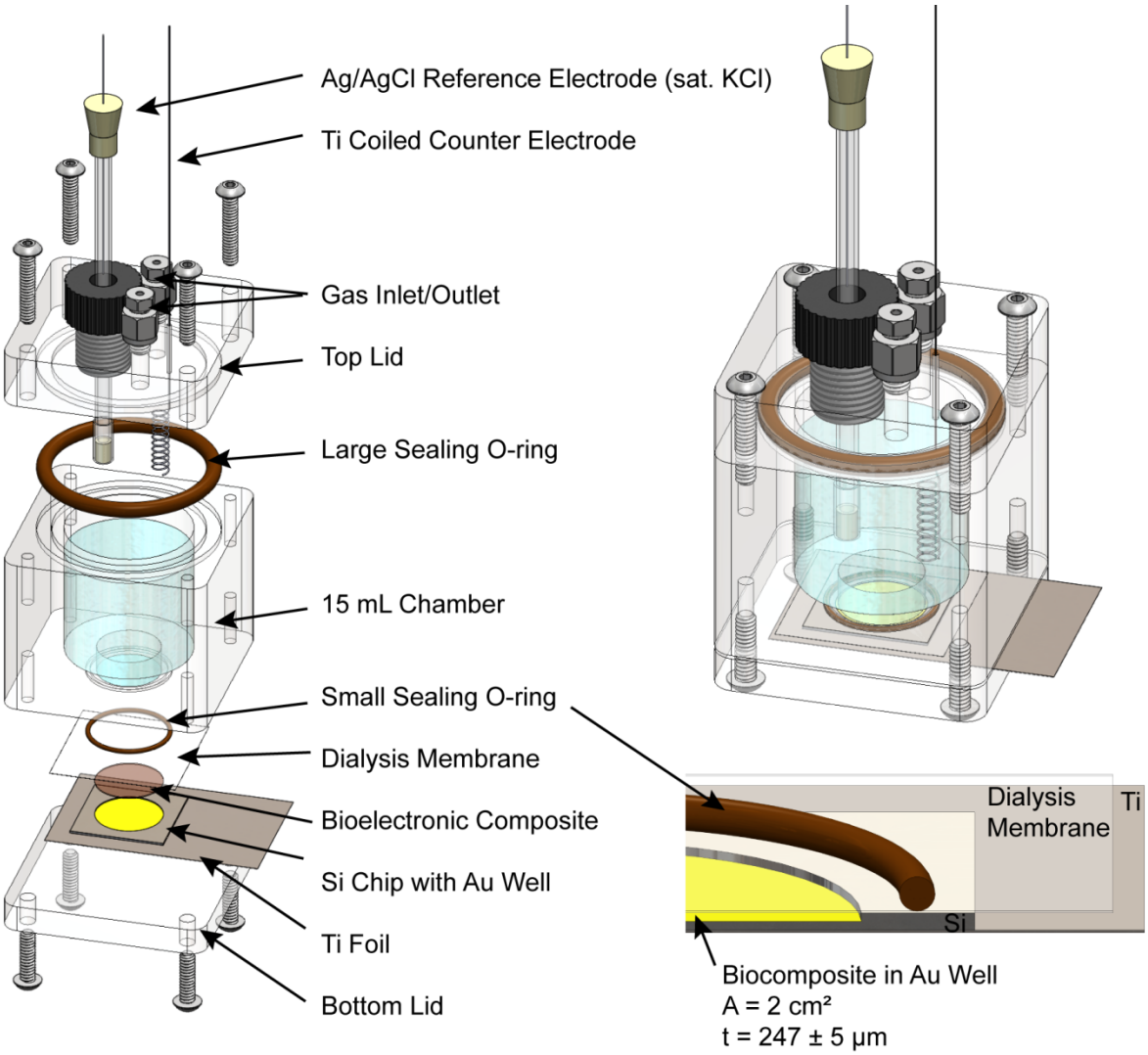

Figure 4.S2: Planar-electrode electrochemical cell with dialysis membrane device schematic.

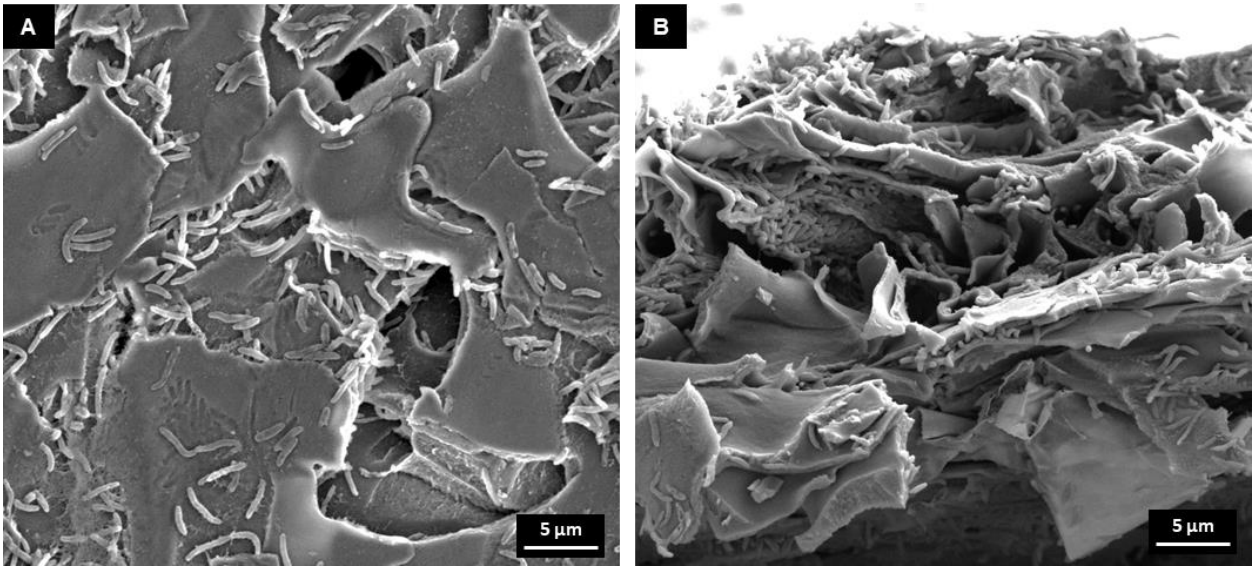

Figure 4.S3: SEM of working electrodes after 7 days of CA current collection. a) 10 mg mL^{-1} CPE-K biocomposite. b) 10 mg mL^{-1} CPE-K biocomposite cross-section.

4.8 Acknowledgements

S. R. M. acknowledges funding from the National Science Foundation Graduate Research Fellowships Program (NSF GRFP) under grant 1650114. Funding was provided by the Institute for Collaborative Biotechnologies (ICB) under grant W911NF-09-D-0001-0044 from the U.S. Army Research Office. Electron microscopy research reported here made use of shared facilities of the UCSB MRSEC (NSF DMR 1720256), a member of the Materials Research Facilities. We acknowledge the use of the NRI-MCDB Microscopy Facility under NSF MRI grant DBI-1625770 (confocal) and NIH: 1S10 ODO010610-01A1 (computer workstations). S. R. M. acknowledges the help of Dr. Yude Su who fabricated the gold electrodes used in the work. S. R. M also acknowledges Dr. Dirk Leifert for the large batch synthesis of CPE-K

4.9 References

(1) Logan, B. E. Exoelectrogenic Bacteria That Power Microbial Fuel Cells. *Nat. Rev. Microbiol.* **2009**, *7* (5), 375–381. https://doi.org/10.1038/nrmicro2113.

(2) Logan, B. E.; Hamelers, B.; Rozendal, R.; Schröder, U.; Keller, J.; Freguia, S.; Aelterman, P.; Verstraete, W.; Rabaey, K. Microbial Fuel Cells: Methodology and Technology. *Environ. Sci. Technol.* **2006**, *40* (17), 5181–5192. https://doi.org/10.1021/es0605016.

(3) Logan, B. E.; Rabaey, K. Conversion of Wastes into Bioelectricity and Chemicals by Using Microbial Electrochemical Technologies. *Science (80-.).* **2012**, *337* (6095), 686–690. https://doi.org/10.1126/science.1217412.

(4) Lovley, D. R. Live Wires: Direct Extracellular Electron Exchange for Bioenergy and the Bioremediation of Energy-Related Contamination. *Energy Environ. Sci.* **2011**, *4* (12), 4896. https://doi.org/10.1039/c1ee02229f.

(5) Nevin, K. P.; Woodard, T. L.; Franks, A. E.; Summers, Z. M.; Lovley, D. R. Microbial Electrosynthesis: Feeding Microbes Electricity To Convert Carbon Dioxide and Water to Multicarbon Extracellular Organic Compounds. *Am. Soc. Microbiol.* **2010**, *1* (2), 1–4. https://doi.org/10.1128/mBio.00103-10.Editor.

(6) Rabaey, K.; Rozendal, R. A. Microbial Electrosynthesis — Revisiting the Electrical Route for Microbial Production. *Nat. Rev. Microbiol.* **2010**, *8* (10), 706–716. https://doi.org/10.1038/nrmicro2422.

(7) Guo, K.; Freguia, S.; Dennis, P. G.; Chen, X.; Donose, B. C.; Keller, J.; Gooding, J. J.; Rabaey, K. Effects of Surface Charge and Hydrophobicity on Anodic Biofilm Formation, Community Composition, and Current Generation in Bioelectrochemical Systems. *Environ. Sci. Technol.* **2013**, *47* (13), 7563–7570. https://doi.org/10.1021/es400901u.

(8) Bonanni, P. S.; Bradley, D. F.; Schrott, G. D.; Busalmen, J. P. Limitations for Current Production in Geobacter Sulfurreducens Biofilms. *ChemSusChem* **2013**, *6* (4), 711–720. https://doi.org/10.1002/cssc.201200671.

(9) Popat, S. C.; Torres, C. I. Critical Transport Rates That Limit the Performance of Microbial Electrochemistry Technologies. *Bioresour. Technol.* **2016**, *215*, 265–273. https://doi.org/10.1016/j.biortech.2016.04.136.

(10) Du, J.; Catania, C.; Bazan, G. C. Modification of Abiotic-Biotic Interfaces with Small Molecules and Nanomaterials for Improved Bioelectronics. *Chem. Mater.* **2014**, *26* (1), 686–697. https://doi.org/10.1021/cm401912j.

(11) Zhang, P.; Liu, J.; Qu, Y.; Li, D.; He, W.; Feng, Y. Nanomaterials for Facilitating Microbial Extracellular Electron Transfer: Recent Progress and Challenges.

Bioelectrochemistry **2018**, *123*, 190–200. https://doi.org/10.1016/j.bioelechem.2018.05.005.

(12) Chaudhuri, S. K.; Lovley, D. R. Electricity Generation by Direct Oxidation of Glucose in Mediatorless Microbial Fuel Cells. *Nat. Biotechnol.* **2003**, *21* (10), 1229–1232. https://doi.org/10.1038/nbt867.

(13) Logan, B.; Cheng, S.; Watson, V.; Estadt, G. Graphite Fiber Brush Anodes for Increased Power Production in Air-Cathode Microbial Fuel Cells. *Environ. Sci. Technol.* **2007**, *41* (9), 3341–3346. https://doi.org/10.1021/es062644y.

(14) Aelterman, P.; Versichele, M.; Marzorati, M.; Boon, N.; Verstraete, W. Loading Rate and External Resistance Control the Electricity Generation of Microbial Fuel Cells with Different Three-Dimensional Anodes. *Bioresour. Technol.* **2008**, *99* (18), 8895–8902. https://doi.org/10.1016/j.biortech.2008.04.061.

(15) Lepage, G.; Albernaz, F. O.; Perrier, G.; Merlin, G. Characterization of a Microbial Fuel Cell with Reticulated Carbon Foam Electrodes. *Bioresour. Technol.* **2012**, *124*, 199–207. https://doi.org/10.1016/j.biortech.2012.07.067.

(16) Xie, X.; Ye, M.; Hu, L.; Liu, N.; Mcdonough, J. R.; Chen, W.; Alshareef, H. N.; Criddle, C. S.; Cui, Y.; Environ, E.; Xie, X.; Ye, M.; Hu, L.; Liu, N.; Mcdonough, J. R.; Chen, W.; Alshareef, H. N. Carbon Nanotube-Coated Macroporous Sponge for Microbial Fuel Cell Electrodes. *Energy Environ. Sci.* **2012**, *5* (1), 5265–5270. https://doi.org/10.1039/c1ee02122b.

(17) Chong, P.; Erable, B.; Bergel, A. Microbial Anodes: What Actually Occurs inside Pores? *Int. J. Hydrogen Energy* **2019**, *44* (9), 4484–4495. https://doi.org/10.1016/j.ijhydene.2018.09.075.

(18) Xie, X.; Criddle, C.; Cui, Y. Design and Fabrication of Bioelectrodes for Microbial Bioelectrochemical Systems. *Energy Environ. Sci.* **2015**, *8* (12), 3418–3441. https://doi.org/10.1039/C5EE01862E.

(19) Yu, Y.-Y.; Zhai, D.-D.; Si, R.-W.; Sun, J.-Z.; Liu, X.; Yong, Y.-C. Three-Dimensional Electrodes for High-Performance Bioelectrochemical Systems. *Int. J. Mol. Sci.* **2017**, *18* (1), 90. https://doi.org/10.3390/ijms18010090.

(20) Song, R.-B.; Wu, Y.; Lin, Z.-Q.; Xie, J.; Tan, C. H.; Loo, J. S. C.; Cao, B.; Zhang, J.-R.; Zhu, J.-J.; Zhang, Q. Living and Conducting: Coating Individual Bacterial Cells with in Situ Formed Polypyrrole. *Angew. Chemie Int. Ed.* **2017**, *56* (35), 10516–10520. https://doi.org/10.1002/anie.201704729.

(21) Zajdel, T. J.; Baruch, M.; Méhes, G.; Stavrinidou, E.; Berggren, M.; Maharbiz, M. M.; Simon, D. T.; Ajo-Franklin, C. M. PEDOT:PSS-Based Multilayer Bacterial-Composite Films for Bioelectronics. *Sci. Rep.* **2018**, *8* (1), 15293. https://doi.org/10.1038/s41598-018-33521-9.

(22) Lin, X.; Nishio, K.; Konno, T.; Ishihara, K. The Effect of the Encapsulation of Bacteria in Redox Phospholipid Polymer Hydrogels on Electron Transfer Efficiency in Living Cell-Based Devices. *Biomaterials* **2012**, *33* (33), 8221–8227. https://doi.org/10.1016/j.biomaterials.2012.08.035.

(23) Yong, Y.-C.; Yu, Y.-Y.; Zhang, X.; Song, H. Highly Active Bidirectional Electron Transfer by a Self-Assembled Electroactive Reduced-Graphene-Oxide-Hybridized Biofilm. *Angew. Chemie Int. Ed.* **2014**, *53* (17), 4480–4483. https://doi.org/10.1002/anie.201400463.

(24) Yoshida, N.; Miyata, Y.; Doi, K.; Goto, Y.; Nagao, Y.; Tero, R.; Hiraishi, A. Graphene Oxide-Dependent Growth and Self-Aggregation into a Hydrogel Complex of Exoelectrogenic Bacteria. *Sci. Rep.* **2016**, *6* (1), 21867. https://doi.org/10.1038/srep21867.

(25) Zhou, H.; Zhang, Y.; Mai, C.-K.; Collins, S. D.; Nguyen, T.-Q.; Bazan, G. C.; Heeger, A. J. Conductive Conjugated Polyelectrolyte as Hole-Transporting Layer for Organic Bulk Heterojunction Solar Cells. *Adv. Mater.* **2014**, *26* (5), 780–785. https://doi.org/10.1002/adma.201302845.

(26) Choi, H.; Mai, C.-K.; Kim, H.-B.; Jeong, J.; Song, S.; Bazan, G. C.; Kim, J. Y.; Heeger, A. J. Conjugated Polyelectrolyte Hole Transport Layer for Inverted-Type Perovskite Solar Cells. *Nat. Commun.* **2015**, *6*, 7348. https://doi.org/10.1038/ncomms8348.

(27) Kirchhofer, N. D.; McCuskey, S. R.; Mai, C.; Bazan, G. C. Anaerobic Respiration on Self-Doped Conjugated Polyelectrolytes: Impact of Chemical Structure. *Angew. Chemie Int. Ed.* **2017**, *56* (23), 6519–6522. https://doi.org/10.1002/anie.201701964.

(28) Danielsen, S. P. O.; Sanoja, G. E.; McCuskey, S. R.; Hammouda, B.; Bazan, G. C.; Fredrickson, G. H.; Segalman, R. A. Mixed Conductive Soft Solids by Electrostatically Driven Network Formation of a Conjugated Polyelectrolyte. *Chem. Mater.* **2018**, *30* (4), 1417–1426. https://doi.org/10.1021/acs.chemmater.7b05303.

(29) Feng, G.; Mai, C. K.; Zhan, R.; Bazan, G. C.; Liu, B. Narrow Band Gap Conjugated Polyelectrolytes for Photothermal Killing of Bacteria. *J. Mater. Chem. B* **2015**, *3* (37), 7340–7346. https://doi.org/10.1039/c5tb01118c.

(30) Marsili, E.; Rollefson, J. B.; Baron, D. B.; Hozalski, R. M.; Bond, D. R. Microbial Biofilm Voltammetry: Direct Electrochemical Characterization of Catalytic Electrode-Attached Biofilms. *Appl. Environ. Microbiol.* **2008**, *74* (23), 7329–7337. https://doi.org/10.1128/AEM.00177-08.

(31) Pocaznoi, D.; Erable, B.; Etcheverry, L.; Delia, M. L.; Bergel, A. Towards an Engineering-Oriented Strategy for Building Microbial Anodes for Microbial Fuel Cells. *Phys. Chem. Chem. Phys.* **2012**, *14* (38), 13332–13343. https://doi.org/10.1039/c2cp42571h.

(32) Schröder, U.; Harnisch, F.; Angenent, L. T. Microbial Electrochemistry and Technology: Terminology and Classification. *Energy Environ. Sci.* **2015**, *8* (2), 513–519. https://doi.org/10.1039/c4ee03359k.

(33) Babauta, J. T.; Beyenal, H. Biofilm Electrochemistry. In *Biofilms in Bioelectrochemical Systems*; Wiley, 2015; pp 121–176. https://doi.org/10.1002/9781119097426.ch5.

(34) Von Canstein, H.; Ogawa, J.; Shimizu, S.; Lloyd, J. R. Secretion of Flavins by Shewanella Species and Their Role in Extracellular Electron Transfer. *Appl. Environ. Microbiol.* **2008**, *74* (3), 615–623. https://doi.org/10.1128/AEM.01387-07.

(35) Okamoto, A.; Kalathil, S.; Deng, X.; Hashimoto, K.; Nakamura, R.; Nealson, K. H. Cell-Secreted Flavins Bound to Membrane Cytochromes Dictate Electron Transfer Reactions to Surfaces with Diverse Charge and PH. *Sci. Rep.* **2014**, *4*, 1–8. https://doi.org/10.1038/srep05628.

(36) Babanova, S.; Cornejo, J.; Roy, J. N.; Babanova, S.; Garcia, K. E.; Cornejo, J.; Ista, L. K.; Atanassov, P. Catalytic Biofilm Formation by Shewanella Oneidensis MR-1 and Anode Characterization by Expanded Uncertainty. *Electrochim. Acta* **2017**, *126* (July 2013), 3–10. https://doi.org/10.1016/j.electacta.2013.07.075.

(37) Kirchhofer, N. D.; Chen, X.; Marsili, E.; Sumner, J. J.; Dahlquist, F. W.; Bazan, G. C. The Conjugated Oligoelectrolyte DSSN+ Enables Exceptional Coulombic Efficiency via Direct Electron Transfer for Anode-Respiring Shewanella Oneidensis MR-1-a Mechanistic Study. *Phys. Chem. Chem. Phys.* **2014**, *16* (38), 20436–20443. https://doi.org/10.1039/c4cp03197k.

(38) Crittenden, S. R.; Sund, C. J.; Sumner, J. J. Mediating Electron Transfer from Bacteria to a Gold Electrode via a Self-Assembled Monolayer. *Langmuir* **2006**, *22* (23), 9473–9476. https://doi.org/10.1021/la061869j.

(39) Kane, A. L.; Bond, D. R.; Gralnick, A.; Gralnick, J. A. Electrochemical Analysis of Shewanella Oneidensis Engineered to Bind Gold Electrodes. *ACS Synth. Biol.* **2013**, *2* (2), 93–101. https://doi.org/10.1021/sb300042w.

(40) Fong, K. D.; Wang, T.; Smoukov, S. K. Multidimensional Performance Optimization of Conducting Polymer-Based Supercapacitor Electrodes. *Sustain. Energy Fuels* **2017**, *1* (9), 1857–1874. https://doi.org/10.1039/C7SE00339K.

(41) Mathis, T. S.; Kurra, N.; Wang, X.; Pinto, D.; Simon, P.; Gogotsi, Y. Energy Storage Data Reporting in Perspective—Guidelines for Interpreting the Performance of Electrochemical Energy Storage Systems. *Adv. Energy Mater.* **2019**, *9* (39), 1902007. https://doi.org/10.1002/aenm.201902007.

(42) Proctor, C. M.; Rivnay, J.; Malliaras, G. G. Understanding Volumetric Capacitance in Conducting Polymers. *J. Polym. Sci. Part B Polym. Phys.* **2016**, *54* (15), 1433–1436.

https://doi.org/10.1002/polb.24038.

(43) Bard, A. J.; Faulkner, L. R. *Electrochemical Methods: Fundamentals and Applications*, 2nd ed.; John Wiley & Sons, Inc, 2001.

(44) Mai, C. K.; Zhou, H.; Zhang, Y.; Henson, Z. B.; Nguyen, T. Q.; Heeger, A. J.; Bazan, G. C. Facile Doping of Anionic Narrow-Band-Gap Conjugated Polyelectrolytes during Dialysis. *Angew. Chemie - Int. Ed.* **2013**, *52* (49), 12874–12878. https://doi.org/10.1002/anie.201307667.

(45) Leekha, S.; Terrell, C. L.; Edson, R. S. General Principles of Antimicrobial Therapy. *Mayo Clin. Proc.* **2011**, *86* (2), 156–167. https://doi.org/10.4065/mcp.2010.0639.

Chapter **5**

Testing Conjugated Polyelectrolyte Bioelectronic Composites in Microbial Fuel Cells

A key element in microbial bioelectrochemical systems is the electronic coupling at the biotic/abiotic interface between the electroactive bacteria and the charge collecting electrode. The self-doped conjugated polyelectrolyte CPE-K has been previously used with *Shewanella oneidensis* MR-1 to create three-dimensional conductive composites that showed enhanced current density when tested at the poised potential of 0.3 V vs Ag/AgCl. Increased current was not only due to the increased organism loading per electrode area, but also effective long-range electron transport through the polymer network. It is shown that in microbial fuel cells (MFCs) where the anode potential is established through the lactate oxidation by the microbes, the CPE-K polymer network is not activated. Even so, the bioelectronic composites show ~22-fold increased steady-state current density and ~65% higher maximum power production when compared to control biofilms in MFCs. These results support the need for further development of conducting polymers with frontier orbital energies more commensurate with physiologically relevant electron transfer processes.

5.1 Introduction

Microbial fuel cells (MFCs) utilize bacteria to harvest chemical energy as electricity.[1–4] In MFCs, microbes at the anode oxidize a carbon source generating electrons and protons in the process. These electrons are then collected by the anode, which acts as an artificial electron acceptor, and then transported to the cathode through an external circuit. Together with the electrons and protons, an ultimate electron acceptor such as oxygen is reduced at the cathode. In addition to employment in simultaneous wastewater treatment and electricity generation, MFC based biosensors are of great interest due to their high sensitivity, stability, and remote site applicability.[5,6] However, inefficient interfacial contacts pose a primary bottleneck for electron transfer throughout the range of MFC technologies.[7–9] Substantial efforts thus are centered on seeking enhancements through engineering of device configurations and electrode surfaces.

Recently, a bioelectronic composite material comprised of the self-doped conjugated polyelectrolyte CPE-K and the electrogenic *Shewanella oneidensis* MR-1 was shown to increase biocurrent output compared to control biofilms on gold electrodes.[10] The CPE-K functioned to connect the microbes to the electrode through a three-dimensional conductive network, increasing the number of bacteria accessible by the electrode. The conductive avenues and increased microbial loading in the composite were achieved over time by the synergistic action of the microbes and polymer. However, this composite was formed by poising the electrode at 0.3 V vs Ag/AgCl in order to oxidize the CPE-K polymer so that it could act as an electron transfer pathway. In this study, these bioelectronic composites are tested in MFCs, to see if they can operate autonomously. Composites are first conditioned with the application of a poised potential and then assessed in single-chamber MFCs using

lactate as the carbon source and air-cathodes to provide the complimentary reduction reaction. See the supplementary **Figure 5.S1** for a diagram of the hybrid three-electrode electrochemical cell/microbial fuel cell.

5.2 Activity of Bioelectronic Composites in Microbial Fuel Cells

CPE-K/*S. oneidensis* MR-1 bioelectronic composites were prepared as previously reported by simply mixing 10 mg mL^{-1} CPE-K with stationary liquid cultures.[10] Bioelectronic composites and *S. oneidensis* MR-1 control biofilms were conditioned in anaerobic microbial three-electrode electrochemical cells with the anode poised at 0.3 V vs Ag/AgCl. This poised potential was chosen to encompass the electron transfer pathways of *S. oneidensis* MR-1 (flavins, -0.4 V to -0.3 V vs Ag/AgCl; membrane proteins, ~0 V vs Ag/AgCl) and the oxidation potential of CPE-K (0.27 V vs Ag/AgCl).[11–16] After 5 days, the average steady-state biocurrent density (*J*) of control biofilms was 1.2 ± 0.2 mA m^{-2} while the CPE-K biocomposites showed ~120-fold higher *J* at 144 ± 12 mA m^{-2}, see **Figure 5.1**. Cyclic voltammetry (CV) characterization of the control biofilms in **Figure 5.2a** showed a catalytic wave centered around ~0 V from the direct electron transfer though the membrane proteins of *S. oneidensis* MR-1. Conductive network formation in the CPE-K bioelectronic composite was confirmed by the square-wave pseudo-capacitive feature in the CV (**Figure 5.2b**).[17–19] As reported previously, the peak between 0 V – 0.2 V vs Ag/AgCl can be attributed to oxidation of membrane proteins of microbes that are in the conductive polymer network.[10] This peak is shifted from 0 V due to the variable resistance of the CPE-K.

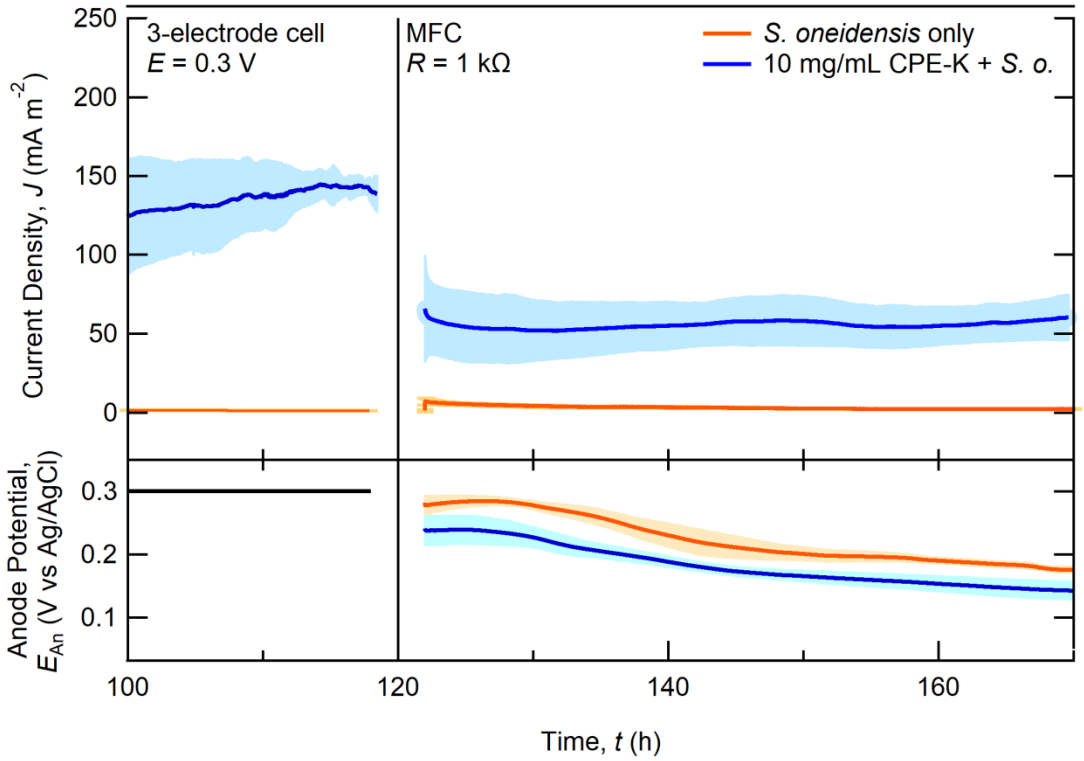

Figure 5.1: Average steady-state biocurrent production and anode potential in MFCs with 1 kΩ external resistance after conditioning at 0.3 V vs Ag/AgCl. Shaded areas represent ± 1 standard deviation from the mean (n ≥ 3).

With the biofilms and conductive network established, reactors were switched to an MFC-configuration. The anode was connected to the air-cathode by an external resistor (1 kΩ). Control reactors had a steady-state J = 2.2 ± 0.3 mA m^{-2} while CPE-K biocomposites showed 60 ± 15 mA m^{-2}, see Figure 5.1. There is only a ~26-fold increase in current density between the controls and biocomposites, which is almost an 80% decrease from what was seen in the poised cells. Tracking of the anode potential shows that it was gradually reduced from ca. 0.3 V to ca. 0.15 V vs Ag/AgCl over a two day period as the system equilibrated to the driving force of the complementary oxidation and reduction reactions of the cell (catalytic lactate oxidation and oxygen reduction).

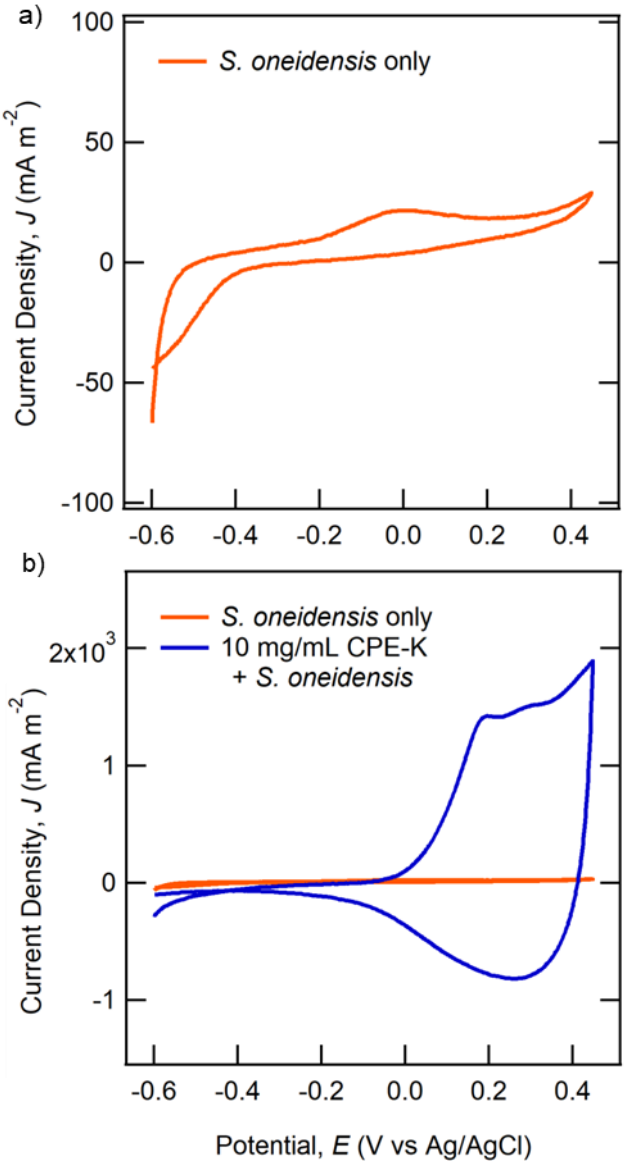

Figure 5.2: Representative CV curves for a) control biofilms and b) CPE-K biocomposites.

The decrease in biocurrent from the CPE-K biocomposite can be explained by the lower anode potential that developed during MFC operation. Using the Nernst equation, the relative amount of oxidized and reduced CPE-K species can be calculated. The Nernst equation (**Equation 5.1**) relates the oxidation potential (E°_{ox}) of the polymer to the anode potential E_{An}, temperature T, and species activities (here approximated as concentrations):

$$E_{\mathrm{An}} = E^{\circ}_{\mathrm{ox}} - \frac{RT}{F} \ln \frac{[\mathrm{Red}]}{[\mathrm{Ox}]} \qquad (5.1)$$

where R is the gas constant and F is Faraday's constant. At E_{An} = 150 mV, a negligible fraction of CPE-K is oxidized and is able to accept metabolic electrons from *S. oneidensis* MR-1. In other words, the CPE-K network formed during the composite conditioning would not be active during MFC operation.

The charge transfer resistance in the bioelectronic composites between conditioning and MFC-operation can be quantified by electrochemical impedance spectroscopy. **Figure 5.3** shows Nyquist plots of bioelectronic composites taken at different anode potentials. Both spectra show a semi-circle feature at high frequencies followed by a linear tail at low frequencies. The diameter of the semi-circle represents the resistance to change transfer (R_{CT}).[20] At E_{An} = 300 mV, R_{CT} is ~40 Ω. When the anode potential is reduced to 150 mV, R_{CT} doubles to ~100 Ω. Also, the low frequency tail shifts from a more vertical angle to 45˚ indicating mass transport limitations.[18,21] Therefore, the change in resistance could be due to both the reduced number of free change carriers in the system as well as disruption of the CPE-K network.

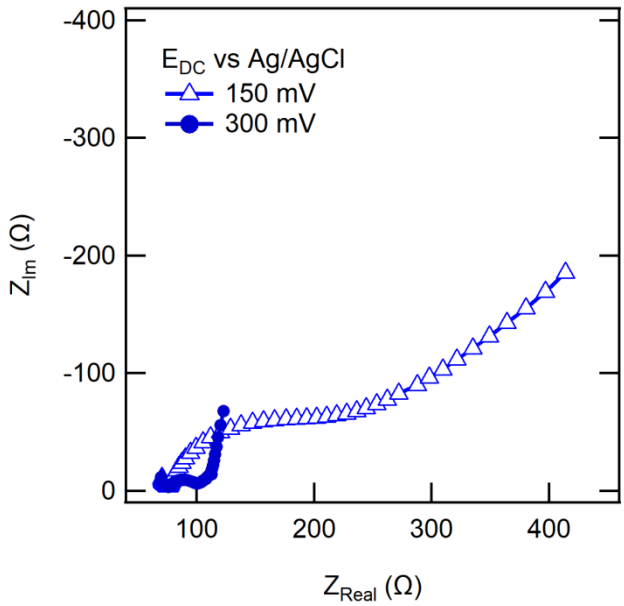

Figure 5.3: Nyquist plot of CPE-K biocomposite at 150 mV vs Ag/AgCl (representative of the anode potential in steady-state MFC operation) and 300 mV vs Ag/AgCl (potential poised during biofilm conditioning).

5.3 Power Production

By varying the external resistance, the polarization curves and power density curves were recorded for the MFCs (**Figure 5.4**).[22] Near the open circuit voltage, produced by highest external resistance, the control biofilms and bioelectronic composites performed similarly, having 550 ± 30 mV and 540 ± 60 mV cell voltages respectively in Figure 5.4a. The trend in current density began to diverge after the anode potential reached ~0 V, with the bioelectronic composites reaching a maximum current density of 110 ± 30 mA m^{-2}, about ~2.5-fold higher than the controls. As a result, the biocomposites also showed higher maximum power densities of 6.8 ± 0.3 mW m^{-2}, only ~65% higher than that of the controls.

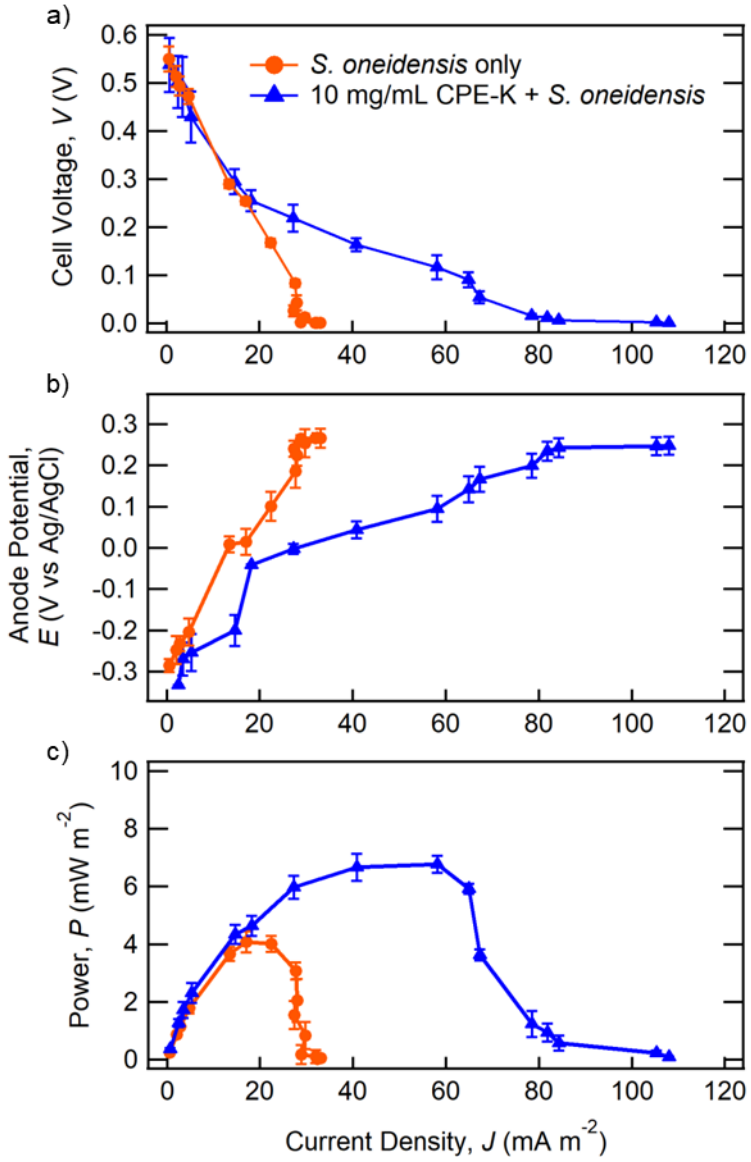

Figure 5.4: Polarization tests of control biofilms and CPE-K biocomposites in MFCs. a) Cell voltages. b) Anode potentials (vs Ag/AgCl). c) Power curves.

5.4 Conclusion

To summarize, bioelectronic composites comprised of the self-doped conjugated polyelectrolyte CPE-K and *S. oneidensis* MR-1 were tested in single chamber MFCs equipped with air-cathodes. While the anode potential developed during operation with a 1 kΩ external resistance was much lower than the oxidation potential of CPE-K (~150 mV

compared to 270 mV vs Ag/AgCl), the bioelectronic composites still exhibited enhanced performance over control biofilms. By having a larger cell voltage at higher current densities, the biocomposites increased the maximum power density by ~65%. These results highlight that although conjugated polyelectrolytes can be used with electroactive bacteria to create 3D bioelectronic composites (an alternative to 3D inorganic electrodes) the need exists for further materials design efforts to tailor electronic properties towards more physiological relevant levels. As it so happens, a hallmark of organic semiconductors is the ability to tune properties through molecular design. Even so, these bioelectronic composites might have application in biosensors that employ a constant anode potential during detection.

5.5 Materials, Methods, & Supplementary Figures

5.5.1 Materials & Methods

Materials: All chemicals were purchased from Fisher Scientific or Sigma Aldrich and used as received unless otherwise indicated. CPE-K was synthesized according to literature procedures.[23] The molecular weight of CPE-K was determined by GPC of the tetrabutylammonium congener. GPC (DMF): M_n = 6638, M_w = 21434, *PDI* = 3.22.

Cell culture and growth medium: *Shewanella oneidensis* MR-1 (ATCC 700550) was struck out on LB agar plates from frozen bacterial stock and incubated at 30 °C to isolate single colonies. Liquid cultures were grown by selecting morphologically similar colonies with a sterile loop to inoculate anaerobic modified M1 medium containing 20 mM Na-(L)-lactate as electron donor and 20 mM Na-fumarate as electron acceptor. After 24 hours incubation at 30 °C with shaking at 120 rpm, cultures consistently reach a maximum OD_{600} of ~0.22 (or 2.2×10^8 cfu mL^{-1}). These stationary phase cultures are then centrifuged,

washed, and then re-suspended in fresh M1 media to a final concentration of 0.15 OD_{600}. M1 media is a defined media with the following composition per liter: 3 g HEPES buffer, 0.225 g potassium phosphate monobasic, 0.225 g potassium phosphate dibasic, 0.225 g ammonium sulphate, 0.46 g ammonium chloride, 0.117 g magnesium sulphate heptahydrate, 0.5 g cassamino acids, 10 mL DL vitamin mix, 10 mL Wolfe's mineral mix.

Working electrode fabrication: Heavily doped (ρ = 0.001-0.005 Ω cm) p^+ (boron) silicon wafers were obtained from Addison Engineering Inc. The metal electrode in the silicon well was defined by soft lithography (PDMS mask), anisotropic plasma etching (Plasma-Therm DSEIII), and subsequent electron-beam evaporation of Ti (5 nm) and Au (70 nm). The depth of the Si well (247 ± 5 μm) was characterized by profilometery and SEM cross-sections. For electrode fabrication, ohmic contact to the device chip was made by rubbing Ga-In eutectic on its posterior. Then the chip was fixed to Ti foil with carbon tape, providing a point of contact for electrical leads. Immediately before use in M3Cs, electrodes were treated with UV/ozone to make the surface hydrophilic.

Working electrode well loading: For each test condition (bacteria-only controls and biocomposites), solutions were made using 10 mM lactate with 20% glycerol in M1 media. To prepare the biocomposite, the appropriate amount liquid culture or sterile solution was mixed with pre-weighed CPE-K and vortexed. Solutions were transferred into the working electrode well via pipette. In order to precisely control the assembly process, working electrodes were adhered to the M3C bottom lid, placed in an -80 ˚C freezer for 5 minutes, and then quickly sandwiched with the dialysis membrane, sealing O-ring, and M3C chamber. It is important to note that the dialysis membrane confines the bacteria and CPE-K in the working electrode well.

Microbial three-electrode electrochemical cells/fuel cell hybrid (M3C/FCs): Single-chambered cells were fabricated out of acrylic to have a 15 mL working volume and were sealed with silicone O-rings. Reference electrode: Ag/AgCl (saturated KCl) with 3.2 mm Vycor frit (Gamry). Counter electrode: coiled 0.25 mm Ti wire (Aldrich), 10 turns. Membrane: regenerated cellulose dialysis membrane, 3.5 kD molecular weight cut-off (Repligen/Spectrum Laboratories). Air-cathode: 12 cm^2, prepared with carbon cloth (30% wet proofing) coated on one side with a carbon base later and four PTFE diffusion layers, and coated on the other side with 10% Pt on carbon in 5% by weight Nafion solution following procedures by Cheng et al.[24] The chamber was kept as a sterile reservoir of 40 mM lactate in M1 media. Anaerobic conditions were maintained through constant headspace degassing with humidified, deoxygenated N_2. Temperature was kept at 30 °C by housing the M3Cs in a temperature regulated incubator.

Chronoamperometry (CA): Using a Gamry potentiostat (Reference 600, Series G 300, or Interface 1000 E models) and multiplexer (model ECM8), gold working electrode wells were poised at E_{CA} = 0.3 V vs Ag/AgCl to serve as the sole terminal electron acceptor for bacteria. M3Cs wells were inoculated (see above) and incubated in the dark 5 days total to measure current responses. The current response was measured, recorded, and averaged for 20-second blocks (at 160 second intervals) with Gamry software (Framework Version 6.11, Build 2227, 2013).

Cyclic voltammetry (CV): Electrochemical characterization with CV was undertaken at the end of 7 days CA operation to characterize the CPE-K-bacteria-electrode interactions. For these experiments, the working electrode potential was swept from $E_{initial}$ = –0.6 V to E_{vertex} = 0.45 V and back to E_{final} = –0.6 V at a scan rate of 0.005 V/s.

Electrochemical impedance spectroscopy (EIS): Electrochemical characterization with EIS was undertaken at the end of operation to characterize the CPE-K-bacteria-electrode interactions. For these experiments, the working electrode potential was poised at E_{DC} = 0.3 V vs Ag/AgCl and a sinusoidal potential with amplitude E_{AC} = 5 mV vs Ag/AgCl was applied starting from a frequency of 100 kHz to 100 mHz.

EIS spectra were fit to the simplest appropriate equivalent circuit models using Bio-logic EC-Lab software to estimate charge transfer resistance, R_{CT}. The intersection of the Nyquist curve at the Z_{Real} axis in the high-frequency range represents the solution resistance, R_S. The semicircle at high frequency can be modeled with a parallel combination of geometrical capacitance (Q_{geom}) and charge transfer resistance (R_{CT}). To fit spectra with a ~45˚ linear response at low frequencies, an additional circuit element called Warburg impedance, *W*, is added in series. This gives the simplest equivalent circuit $R_S + (Q_{geom}/R_{CT}) + W$. For EIS data with a more vertical linear response at low frequencies, an interfacial capacitance (Q_{int}) is used in place of the Warburg element, giving the equivalent circuit $R_S + (Q_{geo}/R_{CT}) + Q_{int}$. In all cases a constant phase element "*Q*" is used in place of a pure capacitor element to represent the deviation from an ideal capacitor.

Polarization and Power Curves (MFC): Before polarization tests, the M3C chamber volume was completed with 40 mM lactate in Shewanella Basal Media and N_2 degassing was stopped. Reactors were disconnected from the potentiostat and left at open circuit for 1 hour. The external resistor was then switched from 4 MΩ to 100 Ω in a decreasing order, three points per decade (20 minutes per resistance, single cycle method). The voltages across the resistor were recorded using a eDAQ-e-corder and Chart software. To measure the anode

potential leads from the eDAQ were connected directly between the anode and reference electrode. Current density, *J*, was calculated by

$$J = \frac{V}{R * A} \tag{5.2}$$

Where V is the voltage measured across the external resistor with a value *R*, normalized by the working electrode area *A*. Following this, power, *P*, can be calculated by

$$P = \frac{V^2}{R * A} \tag{5.3}$$

5.5.2 Supplementary Figures

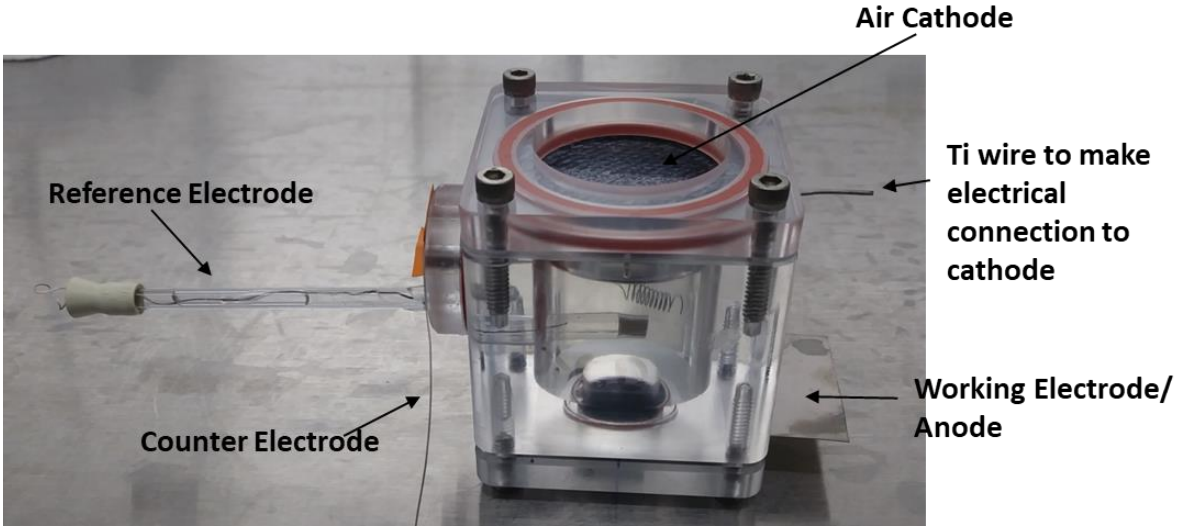

Figure 5.S1: Minimum bactericidal concentration (MBC) testing of CPE-K towards *S. oneidensis* MR-1.

5.6 Acknowledgements

S. R. M. acknowledges funding from the National Science Foundation Graduate Research Fellowships Program (NSF GRFP) under grant 1650114. Funding was provided

by the Institute for Collaborative Biotechnologies (ICB) under grant W911NF-09-D-0001-0044 from the U.S. Army Research Office. S. R. M. gratefully acknowledges the help of Dr. Lijiao Ren in giving advice on MFC set up and air-cathode fabrication as well as Dr. Dirk Leifert who synthesized the CPE-K material used in the work.

5.7 References

(1) Logan, B. E. Exoelectrogenic Bacteria That Power Microbial Fuel Cells. *Nat. Rev. Microbiol.* **2009**, *7* (5), 375–381. https://doi.org/10.1038/nrmicro2113.

(2) Logan, B. E.; Hamelers, B.; Rozendal, R.; Schröder, U.; Keller, J.; Freguia, S.; Aelterman, P.; Verstraete, W.; Rabaey, K. Microbial Fuel Cells: Methodology and Technology. *Environ. Sci. Technol.* **2006**, *40* (17), 5181–5192. https://doi.org/10.1021/es0605016.

(3) Logan, B. E.; Rabaey, K. Conversion of Wastes into Bioelectricity and Chemicals by Using Microbial Electrochemical Technologies. *Science (80-.).* **2012**, *337* (6095), 686–690. https://doi.org/10.1126/science.1217412.

(4) Lovley, D. R. Live Wires: Direct Extracellular Electron Exchange for Bioenergy and the Bioremediation of Energy-Related Contamination. *Energy Environ. Sci.* **2011**, *4* (12), 4896. https://doi.org/10.1039/c1ee02229f.

(5) Dávila, D.; Esquivel, J. P.; Sabaté, N.; Mas, J. Silicon-Based Microfabricated Microbial Fuel Cell Toxicity Sensor. *Biosens. Bioelectron.* **2011**, *26* (5), 2426–2430. https://doi.org/10.1016/j.bios.2010.10.025.

(6) Su, L.; Jia, W.; Hou, C.; Lei, Y. Microbial Biosensors: A Review. *Biosens. Bioelectron.* **2011**, *26* (5), 1788–1799. https://doi.org/10.1016/j.bios.2010.09.005.

(7) Guo, K.; Freguia, S.; Dennis, P. G.; Chen, X.; Donose, B. C.; Keller, J.; Gooding, J. J.; Rabaey, K. Effects of Surface Charge and Hydrophobicity on Anodic Biofilm Formation, Community Composition, and Current Generation in Bioelectrochemical Systems. *Environ. Sci. Technol.* **2013**, *47* (13), 7563–7570. https://doi.org/10.1021/es400901u.

(8) Bonanni, P. S.; Bradley, D. F.; Schrott, G. D.; Busalmen, J. P. Limitations for Current Production in Geobacter Sulfurreducens Biofilms. *ChemSusChem* **2013**, *6* (4), 711–720. https://doi.org/10.1002/cssc.201200671.

(9) Popat, S. C.; Torres, C. I. Critical Transport Rates That Limit the Performance of Microbial Electrochemistry Technologies. *Bioresour. Technol.* **2016**, *215*, 265–273. https://doi.org/10.1016/j.biortech.2016.04.136.

(10) McCuskey, S. R.; Su, Y.; Leifert, D.; Moreland, A. S.; Bazan, G. C. Living Bioelectrochemical Composites. *Adv. Mater.* **2020**, *1908178*, 1908178. https://doi.org/10.1002/adma.201908178.

(11) Marsili, E.; Rollefson, J. B.; Baron, D. B.; Hozalski, R. M.; Bond, D. R. Microbial Biofilm Voltammetry: Direct Electrochemical Characterization of Catalytic Electrode-Attached Biofilms. *Appl. Environ. Microbiol.* **2008**, *74* (23), 7329–7337. https://doi.org/10.1128/AEM.00177-08.

(12) Von Canstein, H.; Ogawa, J.; Shimizu, S.; Lloyd, J. R. Secretion of Flavins by Shewanella Species and Their Role in Extracellular Electron Transfer. *Appl. Environ. Microbiol.* **2008**, *74* (3), 615–623. https://doi.org/10.1128/AEM.01387-07.

(13) Okamoto, A.; Kalathil, S.; Deng, X.; Hashimoto, K.; Nakamura, R.; Nealson, K. H. Cell-Secreted Flavins Bound to Membrane Cytochromes Dictate Electron Transfer Reactions to Surfaces with Diverse Charge and PH. *Sci. Rep.* **2014**, *4*, 1–8. https://doi.org/10.1038/srep05628.

(14) Babanova, S.; Cornejo, J.; Roy, J. N.; Babanova, S.; Garcia, K. E.; Cornejo, J.; Ista, L. K.; Atanassov, P. Catalytic Biofilm Formation by Shewanella Oneidensis MR-1 and Anode Characterization by Expanded Uncertainty. *Electrochim. Acta* **2017**, *126* (July 2013), 3–10. https://doi.org/10.1016/j.electacta.2013.07.075.

(15) Kirchhofer, N. D.; Chen, X.; Marsili, E.; Sumner, J. J.; Dahlquist, F. W.; Bazan, G. C. The Conjugated Oligoelectrolyte DSSN+ Enables Exceptional Coulombic Efficiency via Direct Electron Transfer for Anode-Respiring Shewanella Oneidensis MR-1-a Mechanistic Study. *Phys. Chem. Chem. Phys.* **2014**, *16* (38), 20436–20443. https://doi.org/10.1039/c4cp03197k.

(16) Kirchhofer, N. D.; McCuskey, S. R.; Mai, C.; Bazan, G. C. Anaerobic Respiration on Self-Doped Conjugated Polyelectrolytes: Impact of Chemical Structure. *Angew. Chemie Int. Ed.* **2017**, *56* (23), 6519–6522. https://doi.org/10.1002/anie.201701964.

(17) Fong, K. D.; Wang, T.; Smoukov, S. K. Multidimensional Performance Optimization of Conducting Polymer-Based Supercapacitor Electrodes. *Sustain. Energy Fuels* **2017**, *1* (9), 1857–1874. https://doi.org/10.1039/C7SE00339K.

(18) Mathis, T. S.; Kurra, N.; Wang, X.; Pinto, D.; Simon, P.; Gogotsi, Y. Energy Storage Data Reporting in Perspective—Guidelines for Interpreting the Performance of Electrochemical Energy Storage Systems. *Adv. Energy Mater.* **2019**, *9* (39), 1902007. https://doi.org/10.1002/aenm.201902007.

(19) Proctor, C. M.; Rivnay, J.; Malliaras, G. G. Understanding Volumetric Capacitance in Conducting Polymers. *J. Polym. Sci. Part B Polym. Phys.* **2016**, *54* (15), 1433–1436. https://doi.org/10.1002/polb.24038.

(20) Huggins, R. A. Simple Method to Determine Electronic and Ionic Components of the

Conductivity in Mixed Conductors a Review. *Ionics (Kiel).* **2002**, *8* (3), 300–313. https://doi.org/10.1007/BF02376083.

(21) Bard, A. J.; Faulkner, L. R. *Electrochemical Methods: Fundamentals and Applications*, 2nd ed.; John Wiley & Sons, Inc, 2001.

(22) Logan, B. E.; Hamelers, B.; Rozendal, R.; Schröder, U.; Keller, J.; Freguia, S.; Aelterman, P.; Verstraete, W.; Rabaey, K. Microbial Fuel Cells: Methodology and Technology †. *Environ. Sci. Technol.* **2006**, *40* (17), 5181–5192. https://doi.org/10.1021/es0605016.

(23) Mai, C. K.; Zhou, H.; Zhang, Y.; Henson, Z. B.; Nguyen, T. Q.; Heeger, A. J.; Bazan, G. C. Facile Doping of Anionic Narrow-Band-Gap Conjugated Polyelectrolytes during Dialysis. *Angew. Chemie - Int. Ed.* **2013**, *52* (49), 12874–12878. https://doi.org/10.1002/anie.201307667.

(24) Cheng, S.; Liu, H.; Logan, B. E. Increased Performance of Single-Chamber Microbial Fuel Cells Using an Improved Cathode Structure. *Electrochem. commun.* **2006**, *8* (3), 489–494. https://doi.org/10.1016/j.elecom.2006.01.010.